Host-viral interactions and innate immune evasion by SARS-CoV-2 Nsp14 and HIV-1 Vif

by
Victor L Lam

DISSERTATION
Submitted in partial satisfaction of the requirements for degree of
DOCTOR OF PHILOSOPHY

in

Biochemistry and Molecular Biology

in the

GRADUATE DIVISION
of the
UNIVERSITY OF CALIFORNIA, SAN FRANCISCO

Approved:

DocuSigned by:
Alan Frankel
A0A99322C05A480...

Alan Frankel
Chair

DocuSigned by:
John D Gross
[illegible]F4...

John D Gross

DocuSigned by:
David P. Toczyski
B39DA64A208E4CB...

David P. Toczyski

Committee Members

Acknowledgements

I'd like to start off with scientific acknowledgements of people who contributed to my growth as a scientist. Dr. John Gross has been a supportive mentor and guide throughout the past 5 years I've been in the lab and has been great at helping me navigate the complicated and information-rich field of HIV biology. I'd also like to thank my thesis committee members, Drs. Alan Frankel and Dave Toczyski, for their continued support and advice during committee meetings. I'd also like to thank members of the Gross Lab that were present during my time in the lab for providing a supportive and great environment for doing research.

Work in chapter 1 was done with help from Dr. Jessica Peters in our lab and Taia Wu in Jason Gestwicki's lab. Jessica helped tremendously with guidance on protein purification and on the DSF assay. Taia is the main expert on DSF, and communicated with Jessica on protocols for DSF, dyes, and how to build an assay for our proteins. Jessie was also my rotation mentor when I first rotated in the lab, and she has been a great mentor and resource when it came to learning about protein biochemistry.

Work in chapter 3 would not have been possible without Lily Burton, Leandrew Dailey, Drs. Yang Li, Xi Liu, Jen Binning, Nick Chesarino, and Michael Emerman. Lily and Jen were authors on papers that led to my main thesis project and continued to be supportive and communicative when I first started working on the project and had to troubleshoot protein purification and expression. Xi was extremely helpful in answering technical questions and troubleshooting machinery and issues when it came to Vif and A3G. Yang was extremely helpful in providing guidance with tissue culture, help in splitting cells when I was not around, and in providing guidance and protocols for coIPs. Nick and Michael are great collaborators, and I greatly appreciate the times we were able to discuss results and troubleshoot tissue culture

experiments. They have also been great with sharing reagents required for tissue culture work. Leandrew Dailey has also been hard at work restocking and remaking our A3G stocks for in vitro assays which will allow us to explore more of the in vitro biochemistry behind this mutation.

I would not be the scientist I am today without mentors and great teachers. Dr. Chris Sullivan and Dr. Rodney Kincaid were both great mentors to me as an undergrad during my first serious research experience, and a lot of what I know about how to do science comes from them. They welcomed me into the lab as an undergrad and were not afraid to give me difficult projects that contributed to their papers. Dr. Arturo De Lozanne was my faculty advisor in Dean's Scholars at UT Austin and provided great advice for me as I chose classes and prepared my grad school applications. Dr. Moriah Sandy was the Research Educator for my FRI stream at UT Austin which was one of my first independent research experiences. Without her guidance, I would not have enjoyed research nor would I have had the confidence to pursue other research opportunities on campus.

As for personal thank yous, I want to thank my family and my parents first and foremost. The immigrant experience is not easy, but everyone who came before me worked incredibly hard to provide my generation with education and opportunities. I would not be here today without their support. My Tetrad classmates have also been a source of comfort and comradery during a challenging time for all of us, and I enjoyed the time we spent together. Lastly, I'd like to thank my friends from Texas, some of whom made the long journey to California for my exit talk, for their friendship and providing respite from my PhD whenever I visit home.

Contributions

Work in this dissertation has previously appeared in:

Walter, M. *et al.* SIRT5 is a proviral factor that interacts with SARS-CoV-2 Nsp14 protein. *PLoS Pathogens* **5**, 1–30 (2022).

Host-viral interactions and innate immune evasion of SARS-CoV-2 Nsp14 and HIV-1 Vif

Victor L. Lam

Abstract

Viruses are obligate intracellular parasites and must rely on interactions with host proteins and machinery to produce progeny. Over time, hosts have developed innate immune responses as a first line of defense to control and limit viral infection. This has led to an arms race where viruses find new ways and adaptations to evade host defenses. SARS-CoV-2 encodes a protein called nsp14 which can modify viral mRNA caps to appear more host-like to evade innate immune sensors. Proteomics studies have also found that it binds to several host proteins, including SIRT5, as part of its life cycle but the purpose of this interaction is unknown. HIV and Simian Immunodeficiency Viruses (SIV) encode a protein called Vif to hijack the host E3 ubiquitin ligase complex to target APOBEC3G (A3G), a host antiviral protein, for proteasomal degradation and allow for successful viral replication. This dissertation ties together several different viruses, interactions, and innate immune evasion methods to contribute to our understanding of host-viral interactions. I developed a differential scanning fluorimetry (DSF) assay as a potential screening tool for inhibitors of nsp14 that could be used to combat SARS-CoV-2. I also explored nsp14's interaction with SIRT5 by contributing purified protein to the research effort. This nsp14/SIRT5 interaction was confirmed to have proviral effects, but the exact mechanism is still unknown. On interactions with HIV and SIV Vif and host A3G, I explored the mechanism behind how a single amino acid mutation in Vif allowed it to antagonize A3G in different species and cross a species barrier. By exploring these different variations of

host-viral interactions, we gain a better understanding of viral life cycles and gain knowledge on how to counteract future pandemic viruses.

Table of Contents

List of Figures

List of Tables

Chapter 1

Investigating the properties and interactors of SARS-CoV-2 Nsp10/14

Victor L. Lam[1], Jessica K. Peters[1], Taia Wu[1], and John D. Gross[1,2,3]

Affiliations:

[1] University of California San Francisco, San Francisco, CA, United States.

[2] Department of Pharmaceutical Chemistry, University of California San Francisco, San Francisco, CA, United States.

[3] Quantitative Biosciences Institute (QBI), University of California San Francisco, San Francisco, CA, United States.

Abstract

SARS-CoV-2 nsp14 is a multifunction viral enzyme required for viral replication and innate immune evasion. It contains an exonuclease proofreading domain to limit the number of mutations introduced during replication and a N7 cap methyltransferase domain responsible for modifying the caps of viral mRNAs to avoid immune detection and allow for efficient translation. Inhibiting the cap methylating activity of nsp14 could render SARS-CoV-2 susceptible to the host innate immune response, so we develop in vitro assays and protocols for testing small molecule binding to nsp14 using differential scanning fluorimetry (DSF). We find that small molecules known to bind methyltransferases also bind to nsp14 and nsp10/14 complexes and alter the melting temperature of the protein. These melting temperature changes were clear enough such that DSF could become a useful in vitro screen for small compound inhibitors that bind nsp14 and nsp10/14 complex.

Introduction

SARS-CoV-2 is a respiratory virus that caused major worldwide disruptions and a global pandemic in 2020. Like the original SARS virus, SARS-CoV-2 has a ~30kb positive-sense single-strand RNA genome from which subgenomic RNAs are transcribed and subsequently translated to produce viral proteins, including, but not limited to, spike, nucleocapsid, envelope, and 16 non-structural proteins (1-3). Non-structural proteins, ranging from nsp1 to nsp16, translated from these subgenomic RNAs are primarily enzymes that further the SARS-CoV-2 replication cycle.

As a positive strand RNA virus that replicates in the cytoplasm, coronaviruses like SARS-CoV-2 encode their own mechanisms for capping and modifying its mRNAs to evade the host immune response and allow for eIF4E-dependent translation of viral mRNAs (4-6). The niRAN domain of the SARS-CoV-2 RNA-dependent RNA polymerase (RdRP, also known as nsp12) and nsp9 add a guanosine cap to its mRNAs (7). The methyltransferases nsp14 and nsp16 are then able to add an N7 methyl and a 2′-O methyl to the 5′ cap of viral mRNAs, respectively, by transferring a methyl group from S-adenosylmethionine (SAM) (8,9). Both nsp14 and nsp16 separately bind and form a complex with nsp10. Mutations that disrupt the nsp10-nsp16 interaction led to a reduction in 2′-O methylation activity and virus viability (10). Disrupting the nsp10-nsp14 interaction abrogated the exonuclease proofreading activity of nsp14 but did not appear to have any effect on N7 methylation activity (11). Mutations attenuating nsp14 and nsp16 methyltransferase activity led to a decrease in viral titers due to sensitivity to type I interferon and IFN-induced proteins with tetratricopeptide repeats (IFIT) in the absence of a cap-1 structure.

Cap methylation plays an important role in coronavirus replication, immune evasion, and viral protein translation. Therefore, these cap modifying proteins are inhibition targets for potential drugs against SARS-CoV-2. By developing an in vitro fluorescent assay to test for compound binding to nsp14 and nsp10/14 complex we can quickly screen potential compounds and select those that might merit further investigation.

We explored the possibility of using differential scanning fluorimetry (DSF) as a potential assay for detecting compound binding. DSF takes advantage of the fact that proteins become less stable and unfold as temperature increases (12,13). The melting temperature (T_m), the point at which the concentrations of folded and unfolded proteins are equal, can increase if the protein binds to compounds which in turn increase its stability. As the protein begins to unfold when the temperature increases, fluorescent dyes like SYPRO orange bind to hydrophobic residues that become exposed during unfolding. These dyes are quenched and have little fluorescence in aqueous solution but are highly fluorescent when bound to hydrophobic patches on proteins. This results in an increase in fluorescence as temperature increases. Fluorescence eventually decreases again at higher temperatures due to protein precipitation and aggregation that occludes dye binding. More stable proteins and those bound to ligand unfold at higher temperatures which results in a fluorescence peak shifted rightwards when plotted as a function of temperature. This shift and increase in T_m can be useful in determining whether a ligand or compound binds to a protein.

DSF becomes a powerful tool for screening large numbers of compounds simultaneously because fluorescence from dyes like SYPRO orange can be read out on real-time polymerase chain reaction (RT-PCR) machines using 96-well plates. Additionally, DSF has been used before in drug discovery applications for a variety of receptors and enzymes including SARS-CoV

nsp15, an RNA endonuclease (14). Due to the favorable properties of DSF, we decided to develop it as a potential tool for screening compounds that can bind and inhibit nsp14.

Results

Nsp14 can be purified as either a monomer or in complex with nsp10

Due to the rapid emergence of SARS-CoV-2, there was no published protocol for purifying nsp14 or nsp10/14 complex of the new virus. Previous work described a purification process for these proteins from the original SARS virus, so we used that as the basis for optimizing and building a protocol for purifying the proteins from SARS-CoV-2 (8). We found that placing a 6xhis tag on nsp14 allowed for a good amount of protein to bind to a nickel column and elute at about 20% buffer B (~230mM imidazole) (**Fig. 1.1a,b)**. The eluted peak from the HisTrap column was pooled, loaded onto a Superdex200 column for size exclusion chromatography (SEC), and a peak containing monomeric and usable protein appeared at 15mL (**Fig. 1.1a,c**).

The 6xhis tag nsp14 construct could also be co-purified in complex with nsp10 by combining and co-lysing six liters worth of *E. coli* pellets expressing 6xhis-nsp14 with one liter of 6xhis-nsp10 pellet. Most of the excess nsp10 protein came off in the nickel column wash fractions at around 18-24mL which led to only a minor excess of nsp10 protein in the nickel column eluate at 45mL (**Fig. 1.2a,b)**. The smaller molecular weight of the excess nsp10 caused it to elute later on SEC at 17mL which allowed us to pool earlier peaks containing properly folded nsp10/14 proteins that bound at a 1:1 ratio that eluted at 14-15mL (**Fig. 1.2c,d)**.

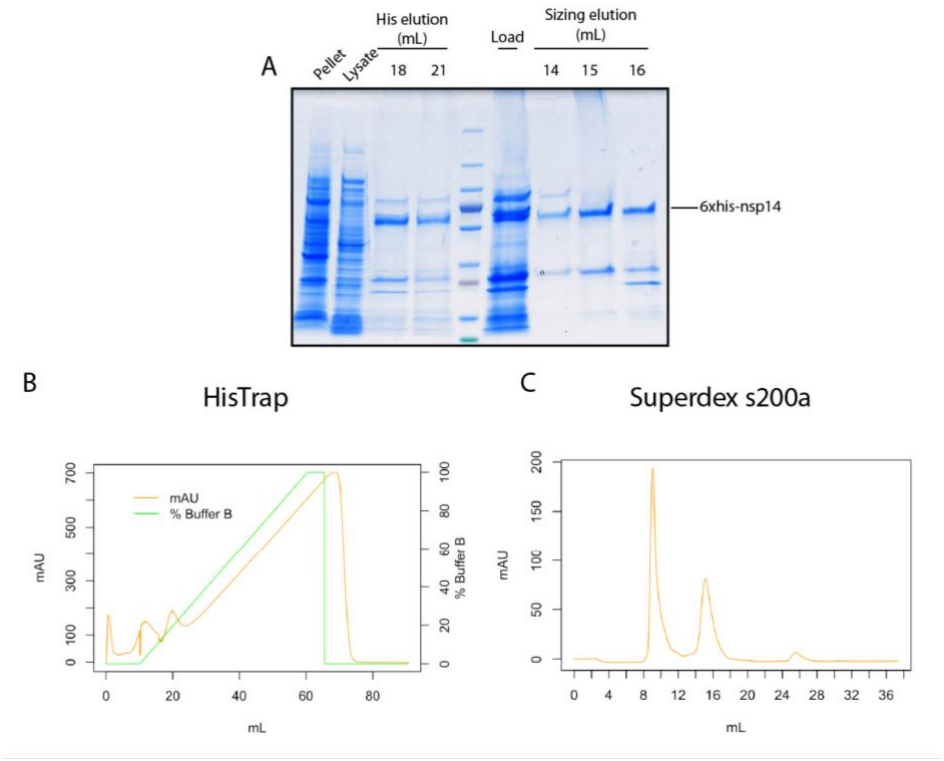

Figure 1.1: Purification of 6xhis-nsp14.
a, PAGE protein gel showing different samples and fractions of the 6xhis-nsp14 purification process. Pellet contains insoluble protein left over after *E. coli* lysis and spin down. Lysate contains all proteins present in the supernatant that is loaded onto the HisTrap column. Load fraction is a sample of what was injected onto the SEC column. b, Chromatograph of protein eluted off the HisTrap column under a gradient of buffer B containing 1M imidazole. c, SEC on a Superdex s200 analytical column of protein collected from the peak at 20mL from the HisTrap column. The first peak around 9mL is the void peak containing mostly aggregated protein while the 15mL peak contains primarily nsp14 protein.

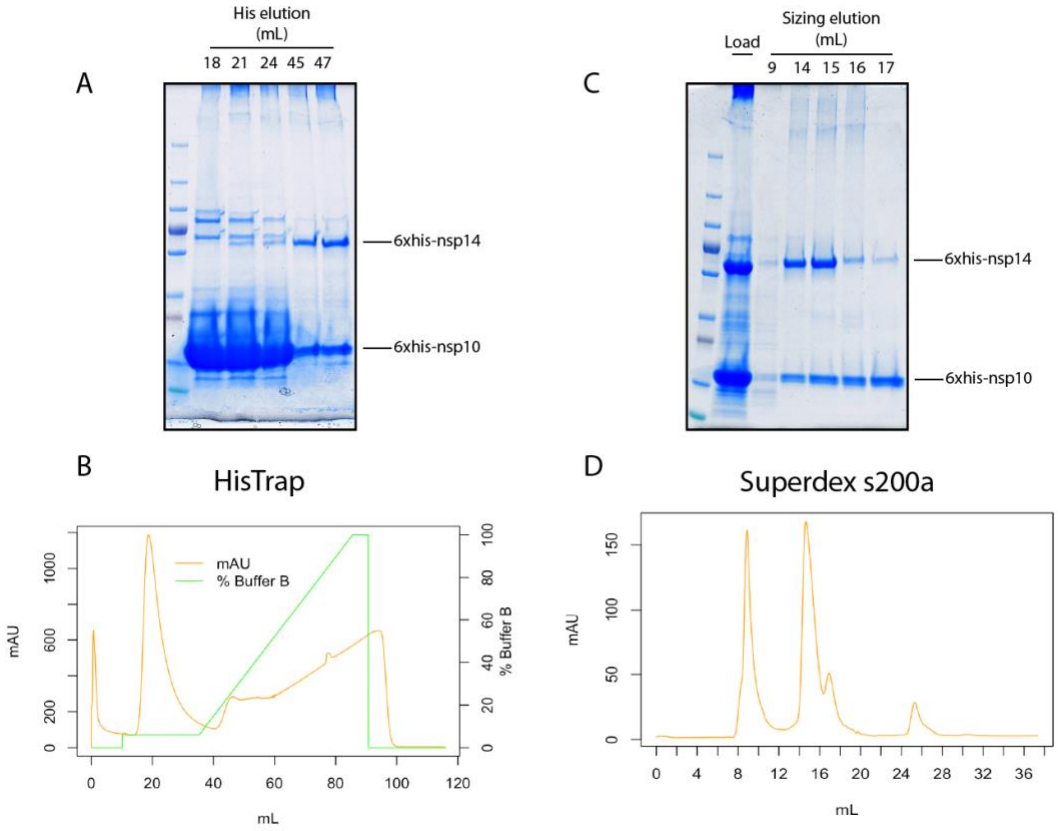

Figure 1.2: Copurification of 6xhis-nsp10/14 complex.
a, PAGE protein gel showing different elution fractions off of HisTrap column. Excess 6xhis-nsp10 washed off with a 6% buffer B wash (~60mM imidazole) at 18-24mL while 1:1 nsp10/14 complex eluted at 45mL. b, Chromatograph corresponding to the His elution gel in A. The peak at 20mL corresponds to excess nsp10 that is washed off while the 45mL peak contains 1:1nsp10/14 complex. c, PAGE protein gel of nsp10/14 complex after SEC on a Superdex200 analytical column with the 14-15mL containing properly folded 1:1 nsp10/14 protein. d, Chromatograph from SEC corresponding to the gel in c.

DSF can be used as a tool to identify compounds that bind to nsp14 and nsp10/14 complex

Because DSF allows for quick and easy initial screening of compounds, we decided to optimize and test whether it could provide useful information regarding compound binding to nsp14 and nsp10/14 complex. While nsp10 only affects nsp14 exonuclease activity and likely has no effect on cap methylation in the original SARS-CoV, we decided to develop the assay for both nsp14 alone and with nsp10/14 complex since we could not dismiss the possibility that

nsp10 could change nsp14 conformation and cap methylating activity in SARS-CoV-2 in a way that affects compound binding (11).

We tested and established this assay with two positive controls known to bind cap methyltransferases. SAM acts as the methyl donor for the methyltransferase reaction, and sinefungin is a pan methyltransferase inhibitor that interacts with the SAM binding pocket of nsp16 (15). These compounds should both bind to nsp14 to some extent and cause a shift in melting temperature.

With nsp14 alone we observed a rightward shift in peaks with increasing amounts of SAM and sinefungin. The melting temperature of nsp14 increased from 43.3°C without inhibitor to 44.3°C with 200μM SAM, and melting temperature increased from 43.2°C without inhibitor to 43.9°C with 200μM sinefungin (**Fig. 1.3a-b, Supplementary Table S1.1**).

With the nsp10/14 complex, we observed similar shifts in melting temperature peaks with SAM and sinefungin. The melting temperature of nsp10/14 increased from 43.1°C without inhibitor to 44.3°C with 200μM SAM, and melting temperature increased from 43°C without inhibitor to 43.4°C with 200μM sinefungin (**Fig. 1.3c-d, Supplementary Table S1.1**). With these large shifts in temperature differences for potential positive controls, DSF could prove useful for identifying compounds that bind and inhibit nsp14.

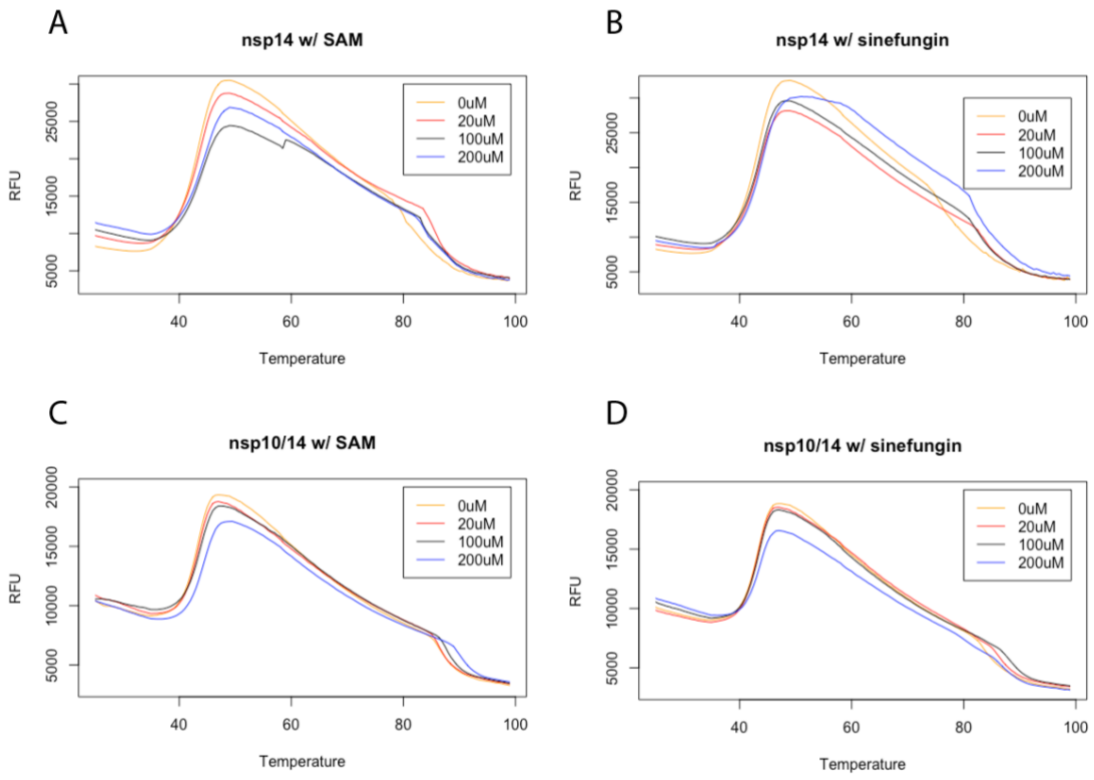

Figure 1.3: DSF of nsp14 and nsp10/14 proteins with SAM and sinefungin.
a, Relative fluorescence readout of nsp14 with different concentrations of SAM. b, Relative fluorescence readout of nsp14 with different concentrations of sinefungin. c, Relative fluorescence readout of nsp10/14 complex with different concentrations of SAM. d, Relative fluorescence readout of nsp10/14 complex with different concentrations of sinefungin.

Discussion

In vitro assays are a powerful tool at analyzing specific proteins and interactions because they can be done quickly at a large scale and provide a complement to experiments done in tissue culture or animal models. Investigating interactions of viral proteins in vitro can provide valuable insight into the function of the protein, the role it plays in the viral life cycle, and vulnerabilities that can be exploited as drug targets. Inhibiting nsp14, which plays a role in viral translation and evading the host innate immune response, could limit SARS-CoV-2 infection. As the first step to investigating drug and protein interactions of nsp14, we developed a protocol for expressing and purifying both nsp14 and nsp10/14 complex in *E. coli*. We were then able to successfully use

these proteins in the development of a DSF assay in which compounds known to bind nsp14 stabilized and shifted the melting temperature of nsp14 and nsp10/14 complex. DSF could be a quick and useful first screen for hundreds of small molecule inhibitors of nsp14 before testing them in more rigorous in vitro activity assays or viral inhibition assays in tissue culture.

Overall, the studies in this chapter provide a framework for investigating nsp14 interactions on a molecular level. We show that nsp14 can be purified alone and in complex with nsp10 from *E.* coli. Furthermore, we establish that DSF is a suitable initial assay for identifying small molecules that bind to nsp14 and nsp10/14 complex.

Methods

Expression and purification of Nsp10/14

The nsp10 and nsp14 proteins from the Wuhan strain of SARS-CoV-2 (NC_045512.2) were codon optimized, ordered as G blocks (IDT), and cloned into a pVFT1S expression vector using a HiFi DNA Assembly kit (New England Biosciences). Both nsp10 and nsp14 contained an N-terminal 6x-His tag followed by a TEV cleavage site.

E. coli BL21*(DE3) cells (Invitrogen) were transformed with the nsp10 and nsp14 expression vectors and grown in LB media containing kanamycin. Cells were induced at an OD_{600} of ~0.8 with 0.5mM IPTG for 16 hours at 16°C. Nsp10 pellets were stored at -20°C, and nsp14 pellets were flash frozen with liquid nitrogen and stored at -80°C until use.

For nsp10/14 copurification, nsp10 pellets from 1L of cells and nsp14 pellets from 6L of cells were resuspended in lysis buffer (50 mM HEPES pH 7.5, 300 mM NaCl, 5 mM MgSO4, 30mM imidazole, 1% NP-40) and combined. For nsp14 purification, pellets were resuspended in lysis buffer. The pellets were lysed using sonication and clarified using centrifugation at 14,500rpm for 40 minutes at 4°C. The supernatant was loaded onto a HisTrap HP column (GE).

The column was loaded onto FPLC and washed using 2 column volumes of Ni Buffer A (50 mM HEPES pH 7.5, 300 mM NaCl, 5 mM MgSO4, 30mM imidazole). For nsp10/14 copurification only, an additional wash was done over 5 column volumes using a buffer of 50 mM HEPES pH 7.5, 300 mM NaCl, 5 mM MgSO4, and 60mM imidazole. Proteins were eluted using 50 mM HEPES pH 7.5, 300 mM NaCl, 5 mM MgSO4, and 300mM imidazole.

The elution was then concentrated and purified further using a Superdex 200 column (GE) and a buffer of 10 mM HEPES pH 7.5, 150 mM NaCl, and 10% glycerol. The purified protein was then concentrated, flash frozen using liquid nitrogen, and stored at -80°C.

Differential Scanning Fluorimetry (DSF) of Nsp14 and Nsp10/14

Reactions for DSF were prepared in 96-well PCR plates at a final volume of 30μL per well. Each well contained a final concentration of 1μM Nsp14 or Nsp10/14 complex, 5x SYPRO Orange dye, 0.01% Triton X-100, and a final concentration of 20, 100, or 200μM sinefungin or S-adenosylmethionine (SAM). The final concentration of buffer and salts in the reaction was 10 mM HEPES pH 7.5, 150 mM NaCl, and 10% glycerol.

Samples were analyzed using the FRET setting on a Bio-Rad CFX96 qPCR machine. Fluorescence measurements (RFU) were taken starting at 25°C and at every 0.5°C up to 100°C. The derivatives of each the RFU measurements were also taken to calculate the melting temperature using the Gestwicki Lab's DSF World program.

Supplemental Data

Supplementary Table S1.1: Melting temperature (TM) of nsp14 and nsp10/14 with SAM and sinefungin.

Compound concentration (μM)	nsp14 and SAM T_M (°C)	Nsp14 and sinefungin T_M (°C)	Nsp10/14 and SAM T_M (°C)	Nsp10/14 and sinefungin T_M (°C)
0	43.3	43.2	43.1	43
20	43.4	43.4	43.2	43
100	44	43.4	43.5	43.2
200	44.3	43.9	44.3	43.4

References

1. Marra, M. A. *et al.* Characterization of a novel coronavirus associated with severe acute respiratory syndrome. *Science* **300**, 1394–1399 (2003).
2. Naqvi, A. A. T. *et al.* Insights into SARS-CoV-2 genome, structure, evolution, pathogenesis and therapies: Structural genomics approach. *Biochimica et Biophysica Acta Molecular Basis of Disease* vol. 1866 (2020).
3. Yadav, R. *et al.* cells Role of Structural and Non-Structural Proteins and Therapeutic Targets of SARS-CoV-2 for COVID-19. *Cells* **10**, 821 (2021).
4. Daffis, S. *et al.* 2′-O methylation of the viral mRNA cap evades host restriction by IFIT family members. *Nature* **468**, 452–456 (2010).
5. Case, J. B., Ashbrook, A. W., Dermody, T. S. & Denison, M. R. Mutagenesis of S -Adenosyl-l -Methionine-Binding Residues in Coronavirus nsp14 N7-Methyltransferase Demonstrates Differing Requirements for Genome Translation and Resistance to Innate Immunity. *J Virol* **90**, 7248–7256 (2016).
6. Pan, R. *et al.* N7-Methylation of the Coronavirus RNA Cap Is Required for Maximal Virulence by Preventing Innate Immune Recognition. *mBio* **13**, 1–21 (2022).
7. Park, G. J. *et al.* The mechanism of RNA capping by SARS-CoV-2. *Nature* **609**, 793–800 (2022).
8. Bouvet, M. *et al.* In vitro reconstitution of SARS-coronavirus mRNA cap methylation. *PLoS Pathog* **6**, 1–13 (2010).
9. Chen, Y. *et al.* Functional screen reveals SARS coronavirus nonstructural protein nsp14 as a novel cap N7 methyltransferase. *PNAS* **106**, 9, 3483-3489.

10. Chen, Y. *et al.* Biochemical and structural insights into the mechanisms of SARS coronavirus RNA ribose 2′-O-methylation by nsp16/nsp10 protein complex. *PLoS Pathog* **7**, (2011).
11. Bouvet, M. *et al.* Coronavirus Nsp10, a critical co-factor for activation of multiple replicative enzymes. *Journal of Biological Chemistry* **289**, 25783–25796 (2014).
12. Gao, K., Oerlemans, R. & Groves, M. R. Theory and applications of differential scanning fluorimetry in early-stage drug discovery. *Biophys Rev* **12**, 85–104 (2020).
13. Niesen, F. H., Berglund, H. & Vedadi, M. The use of differential scanning fluorimetry to detect ligand interactions that promote protein stability. *Nat Protoc* **2**, 2212–2221 (2007).
14. Ortiz-Alcantara, J. *et al.* Small molecule inhibitors of the SARS-CoV Nsp15 endoribonuclease. *Virus Adaptation and Treatment* **2**, 125–133 (2010).
15. Krafcikova, P., Silhan, J., Nencka, R. & Boura, E. Structural analysis of the SARS-CoV-2 methyltransferase complex involved in RNA cap creation bound to sinefungin. *Nat Commun* **11**, (2020).

Chapter 2

SIRT5 is a proviral factor that interacts with SARS-CoV-2 Nsp14 protein

Marius Walter[1,8]*, Irene P Chen[2,3], Albert Vallejo-Gracia[2,3], Ik-Jung Kim[1], Olga Bielska[1], Victor L Lam[3], Jennifer M Hayashi[2,3], Andrew Cruz[1], Samah Shah[1], Frank W Soveg[2,3], John D Gross[3,4], Nevan J Krogan[2,3,4,5], Keith R Jerome[6,7], Birgit Schilling[1], Melanie Ott[2,3], Eric Verdin[1]*.

Author Affiliations:

[1] Buck Institute for Research on Aging, Novato, CA, United States.

[2] Gladstone Institutes, San Francisco, CA, United States.

[3] University of California San Francisco, San Francisco, CA, United States.

[4] Quantitative Biosciences Institute (QBI), University of California San Francisco, San Francisco, CA, United States.

[5] QBI COVID-19 Research Group (QCRG), San Francisco, CA, United States.

[6] Vaccine and Infectious Disease Division, Fred Hutch Cancer Center, Seattle, WA, USA.

[7] Department of Laboratory Medicine, University of Washington, Seattle, WA, USA.

[8] Current address: Vaccine and Infectious Disease Division, Fred Hutch Cancer Center, Seattle, WA, USA.

This chapter is adapted from:

Walter, M. *et al.* SIRT5 is a proviral factor that interacts with SARS-CoV-2 Nsp14 protein. *PLoS Pathogens* **5**, 1–30 (2022).

Abstract

SARS-CoV-2 non-structural protein Nsp14 is a highly conserved enzyme necessary for viral replication. Nsp14 forms a stable complex with non-structural protein Nsp10 and exhibits exoribonuclease and N7-methyltransferase activities. Protein-interactome studies identified human sirtuin 5 (SIRT5) as a putative binding partner of Nsp14. SIRT5 is an NAD-dependent protein deacylase critical for cellular metabolism that removes succinyl and malonyl groups from lysine residues. Here we investigated the nature of this interaction and the role of SIRT5 during SARS-CoV-2 infection. We showed that SIRT5 interacts with Nsp14, but not with Nsp10, suggesting that SIRT5 and Nsp10 are parts of separate complexes. We found that SIRT5 catalytic domain is necessary for the interaction with Nsp14, but that Nsp14 does not appear to be directly deacylated by SIRT5. Furthermore, knock-out of SIRT5 or treatment with specific SIRT5 inhibitors reduced SARS-CoV-2 viral levels in cell-culture experiments. SIRT5 knock-out cells expressed higher basal levels of innate immunity markers and mounted a stronger antiviral response, independently of the Mitochondrial Antiviral Signaling Protein MAVS. Our results indicate that SIRT5 is a proviral factor necessary for efficient viral replication, which opens novel avenues for therapeutic interventions.

Author Summary

SARS-CoV-2 is a pathogen of global concern. After cellular entry, SARS-CoV-2 hijacks the cellular machinery, and the viral proteins physically interact with hundreds of human proteins. Here we described the interaction between SARS-CoV-2 protein Nsp14, a key enzyme necessary for viral replication, and human sirtuin 5 (SIRT5), a protein deacylase that removes succinyl and malonyl groups from lysine residues. We showed that SIRT5 strongly interacts with Nsp14 and that SIRT5 catalytic domain is necessary for the interaction, despite Nsp14 not being

directly deacylated by SIRT5. Furthermore, we found that knocking out or inhibiting SIRT5 reduced SARS-CoV-2 viral levels in cell-culture experiments, and that SIRT5 knock-out cells mounted a stronger antiviral response. Altogether, our result indicates that SIRT5 is a proviral factor necessary for efficient viral replication. SIRT5 is a critical metabolic enzyme that regulates several important metabolic processes, but its role during disease and infection is currently unknown. Our work suggests that SIRT5, and potentially other sirtuins, could act as a bridge between cellular metabolism and the innate responses against viral infections.

Introduction

Severe acute respiratory syndrome coronavirus 2 (SARS-CoV-2) is a pathogen of global concern that needs no further introduction. After cellular entry, SARS-CoV-2 hijacks the cellular machinery, and the viral proteins physically interact with hundreds of human proteins (1–4). In most cases, however, the exact nature of the interactions and their functions and relevance during viral infection remain unknown.

SARS-CoV-2 encodes two large open reading frames, ORF1a and ORF1b, that are processed into 16 non-structural proteins after proteolytic cleavage by viral proteases. The 16 non-structural proteins, Nsp1 to Nsp16, are involved in every aspect of viral replication and are highly conserved in coronaviruses. Coronavirus Nsp14 protein is part of the replication-transcription complex and has two conserved domains with distinct functions. The N-terminal domain acts as a 3’ to 5’ exoribonuclease (ExoN), and the C-terminal domain displays RNA cap guanine N7-methyltransferase (MTase) activity (**Fig. 2.1A**) (5–8). The N-terminal ExoN domain provides proofreading activity during RNA replication, allowing the removal of mismatched nucleotides introduced by the viral RNA polymerase (9–11). This proofreading activity ensures a high level of fidelity during RNA replication and is unique among RNA viruses (12, 13).

Coronaviruses and related viruses in the order nidovirales have some of the largest genomes (26–32 kb) among known RNA viruses (14), and the acquisition of ExoN activity is thought to have allowed nidoviruses to evolve these large genomes (9, 15). The C-terminal MTase domain of Nsp14 is an S-adenosyl methionine (SAM)-dependent methyltransferase critical for viral RNA capping that methylates the 5′ guanine of the Gppp-RNA cap at the N7 position (6, 7). The 5′ cap is important for viral mRNA stability and translation and for escaping host innate antiviral responses. Importantly, Nsp14 forms a stable complex with the non-structural protein Nsp10, a small zinc-binding co-factor with no reported enzymatic activity on its own (7, 10). Nsp10 binds and stabilizes the N-terminal ExoN domain of Nsp14 and is necessary for ExoN activity, but not for MTase activity. Interestingly, mutations that abolish ExoN activity cause a lethal phenotype in SARS-CoV-2 and MERS-CoV, but not in SARS-CoV or other coronaviruses (16), suggesting that ExoN has additional functions beyond its proofreading activity. Indeed, Nsp14 triggers translational shutdown, participates in evasion of innate immunity, activates proinflammatory signals, and mediates viral recombination (17–20).

Large-scale protein-protein interaction analyses of SARS-CoV-2 and human proteins revealed putative interacting partners for all of the SARS-CoV-2 proteins. Several independent studies, from us and others, suggested that SARS-CoV-2 Nsp14 protein interacts with human sirtuin 5 (SIRT5) (1–4). Sirtuins are a family of conserved protein deacylases and mono-ADP-ribosyltransferases found in organisms ranging from bacteria to humans. Sirtuins use nicotinamide adenine dinucleotide (NAD) as a co-substrate and are important regulators of cellular metabolism and aging (21, 22). Most sirtuins act as NAD-dependent protein deacetylases, removing acetyl groups from lysine residues and, as such, tightly connect post-translational protein regulation with cellular metabolism. The seven mammalian sirtuins (SIRT1–

7) are found in different cellular compartments. They deacylate histones and transcriptional regulators in the nucleus and also specific proteins in the cytoplasm and mitochondria. Sirtuins are crucial regulators of cellular metabolism and energy homeostasis and have emerged as key regulators of aging and age-related diseases.

SIRT5 is unique among the seven mammalian sirtuins. It is only a weak protein deacetylase, but it efficiently removes longer-chain acyl groups from proteins, such as succinyl, malonyl or glutaryl groups (23, 24). By preferentially catalyzing the removal of these negatively charged acidic modifications, SIRT5 functions as the main cellular desuccinylase, demalonylase, and deglutarylase (24–26). SIRT5 is predominantly found in the mitochondria, but also exerts regulatory activity in the cytoplasm. It is involved in several important metabolic processes, such as glycolysis, fatty acid oxidation and ketone body production (27). Despite elevated succinylation or malonylation levels in several tissues, no obvious phenotype or abnormalities are observed in *Sirt5* knockout mice under basal conditions (28). The roles of SIRT5 in disease, infection, and aging, are unclear.

Here we investigated the role of SIRT5 during infection with SARS-CoV-2. We showed that SIRT5 interacts with Nsp14, but not with its cofactor Nsp10, and that SIRT5 catalytic activity is necessary for the interaction. Furthermore, knock-out or inhibition of SIRT5 reduced viral levels in cell-culture experiments, revealing that SIRT5 is a proviral factor necessary for efficient viral replication.

Results

SARS-CoV-2 Nsp14 interacts with human SIRT5

Protein-protein interaction mass-spectrometry studies suggested that SARS-CoV-2 Nsp14 binds to SIRT5 (1–4). We first sought to confirm and characterize the nature of this interaction.

We used a mammalian expression vector developed by Gordon et al. that contains Nsp14 with a 2xStrep affinity tag (Nsp14-strep) that can be used for affinity purification (1). Plasmids expressing Nsp14-strep or a GFP control were transfected into HEK-293T cells for 48 hours, and tagged proteins were purified by affinity purification using magnetic beads. Using western blots, we found that SIRT5 was specifically co-purifying with Nsp14, confirming published mass spectrometry results (**Fig. 2.1B**). Immunofluorescence in human alveolar basal epithelial A549 cells transfected with Nsp14 expression plasmid further showed that Nsp14 and SIRT5 co-localized into the same cellular compartments, with a predominantly cytoplasmic and peri-nuclear localization (**Fig. 2.1C**).

We next used Cellular Thermal Shift Assay (CETSA) to quantify the changes in the thermal stability of Nsp14 and SIRT5 in intact cells. The thermal stability of proteins changes upon ligand binding, and CETSA can be used to record the strength of the interaction in the physiological context. HEK-293T cells were transfected with plasmids expressing Nsp14 and SIRT5, either alone or in combination, and the shift in thermal stability was assessed by western blot (**Fig. 2.1D**). We observed an important increase in the stability of both proteins when they were co-transfected together. Nsp14, in particular, was poorly expressed and barely detectable when transfected alone, but a strong signal appeared in the presence of SIRT5. Overall, these initial observations showed that SIRT5 and Nsp14 were interacting in human cells and that SIRT5 strongly stabilized Nsp14 expression.

Nsp14 forms a stable complex with the small viral protein Nsp10 (7, 10). We thus tested whether SIRT5 also interacted with Nsp10, or whether they were parts of independent complexes. To eliminate endogenous expression of SIRT5, we generated a *SIRT5* knockdown cell line (*SIRT5*-KD), using CRISPR interference in HEK-293T cells (29). Several guide RNAs

were tested, and one was selected for the rest of the study. SIRT5 was undetectable in this cell line (**Fig. 2.1E**). Expression plasmids for SIRT5, Nsp14-strep and Nsp10 with a Flag tag (Nsp10-Flag) were transfected alone or in combination for 48 hours in *SIRT5*-KD cells. Proteins were then co-purified either by strep affinity purification (Strep-AP) or Flag immunoprecipitation (Flag-IP) (**Fig. 2.1F**). Strep-AP confirmed that both SIRT5 and Nsp10 interacted with Nsp14. By contrast, pulling down Nsp10 by Flag-IP showed that only Nsp14 co-purified with Nsp10. This indicates that Nsp10 and SIRT5 do not interact. Besides, the SIRT5 signal after Strep-AP appeared to be lower in the presence of Nsp10, and we hypothesized that Nsp10 and SIRT5 compete for Nsp14 binding. To test this hypothesis, Nsp14, SIRT5, and an increasing quantity of Nsp10 plasmids were co-transfected in *SIRT5*-KD cells. SIRT5 binding was lost with high concentrations of Nsp10 (**Fig. 2.1G**). Thus, SIRT5 and Nsp10 competitively bind Nsp14, and Nsp14/SIRT5 and Nsp14/Nsp10 likely form independent complexes.

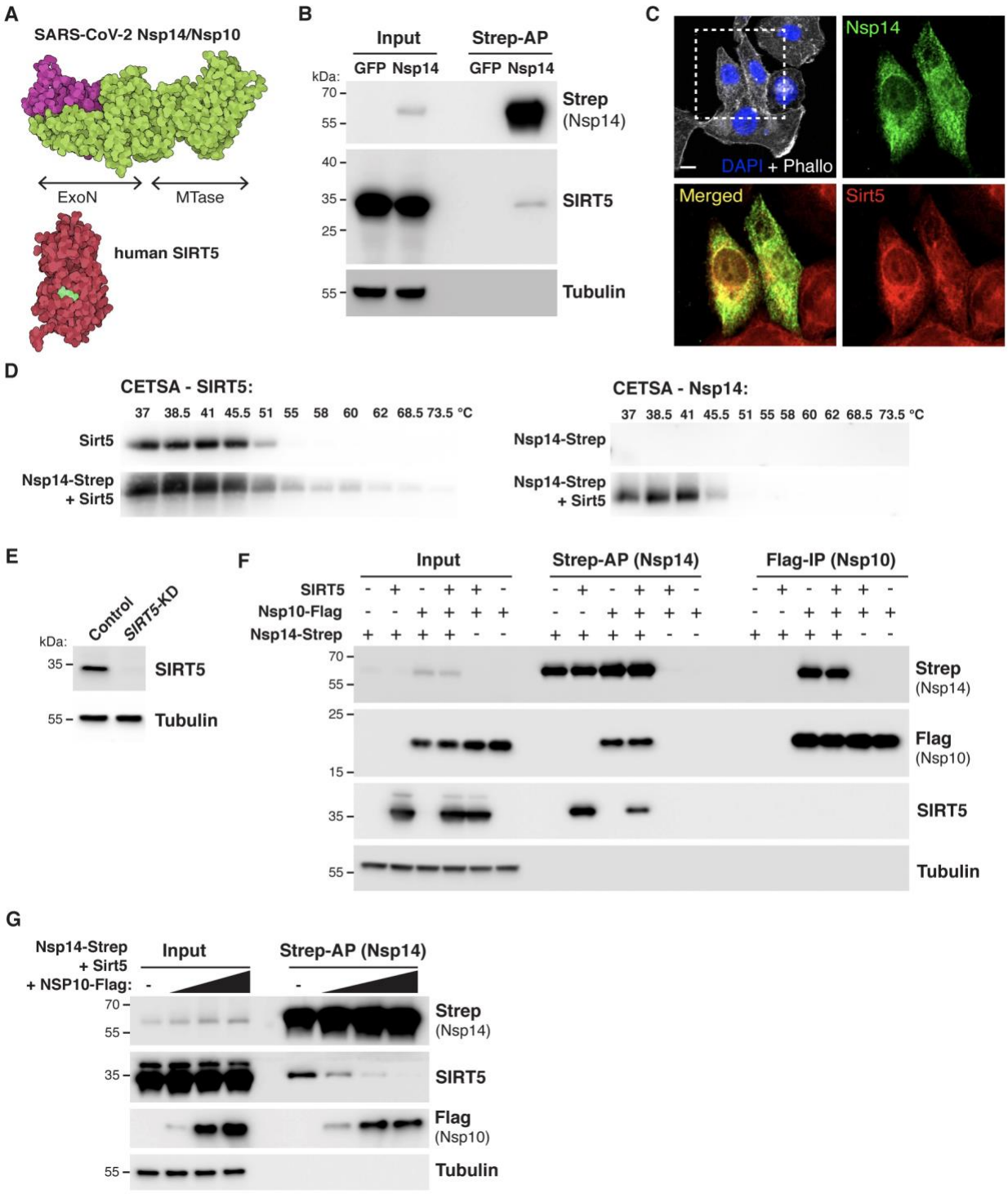

Figure 2.1: SARS-CoV-2 Nsp14 interacts with human SIRT5.
A. Cartoon representation of the protein structure of Nsp14/Nsp10 (PDB 7N0B) and SIRT5 (PDB 3YIR) shows the Nsp14 N-terminal ExoN domain and C-terminal MTase domain. B. Affinity-purification of Nsp14-strep and co-purification of endogenous SIRT5 after transfection in HEK293T cells, as shown by western blot. C. Immunofluorescence of transfected Nsp14-Strep and endogenous SIRT5 in A549 cells. (Figure caption continued on the next page.)

(Figure caption continued from the previous page.) D. CETSA in HEK293T cells transfected with Nsp14-step and/or SIRT5, showing an increase in the stability of SIRT5 and Nsp14 by western blot. E. Western blot showing the absence of SIRT5 in *SIRT5*-KD HEK293T cells. F. Strep-tag affinity-purification or Flag-tag immunoprecipitation, followed by western blot, after transfection with Nsp14-strep, Nsp10-flag and SIRT5 expression constructs. SIRT5 does not interact with Nsp10. 0.5 µg of each construct or of empty control plasmids were transfected in *SIRT5*-KD HEK293T cells in a six-well plate. G. Strep-tag affinity-purification and western blot after transfection of Nsp14-strep, SIRT5 and increasing concentrations of Nsp10-tag indicate competitive binding of SIRT5 and Nsp10. 0.5 µg of Nsp14-strep and SIRT5 plasmid were used in a 6-well plate, with 0, 0.5, 1 or 2 µg of Nsp10-Flag.

SIRT5 catalytic activity is necessary for the interaction with Nsp14

SIRT5 is the main cellular desuccinylase, demalonylase, and deglutarylase, and a weak deacetylase (24–26). SIRT5 can physically bind to some of its enzymatic targets, such as Mitochondrial Antiviral Signaling Protein MAVS (30), mitochondrial serine hydroxymethyltransferase SHMT2 (31), or pyruvate kinase PKM2 (32). In these examples, SIRT5 both desuccinylates and binds the target protein as determined by co-immunoprecipitation. We thus hypothesized that SIRT5 could enzymatically modify Nsp14 and remove a putative succinyl, malonyl or glutaryl group.

To test this hypothesis, we determined if SIRT5 catalytic mutants bind Nsp14. Based on the structure of the SIRT5 catalytic domain and the homology with other sirtuins, we used or generated several expression constructs with mutations in conserved residues: H158 is catalytically required to abstract a proton from NAD, Q140 and I142 are involved in NAD binding, and Y102 and T105 interact with the extended acidic chains of succinyl or malonyl groups (**Fig. 2.2A**). H158, Q140 and I142 are universally conserved in sirtuins, but Y102 and T105 are specific to SIRT5 and mediate the specificity to longer-chain acidic groups (23, 33). Mutation of these residues is known (for H158Y, Y102F and R105M) or predicted (for Q140A and I142A, based on homology with other sirtuins) to abolish SIRT5 desuccinylation activity. After transfection of Nsp14-strep and SIRT5 mutants in *SIRT5*-KD cells, the binding of SIRT5 to

Nsp14 was lost or severely reduced in most mutants (**Fig. 2.2B**). In particular, SIRT5 binding completely disappeared in H158Y and Q140A mutants, and only remained in significant amounts with the Y102F mutation. This result shows that an intact SIRT5 catalytic domain is necessary for the interaction with Nsp14. Of note, treatment of HEK293T cells with the proteasome inhibitor MG-132 did not affect the stability of the overexpressed catalytic mutants, which suggested that the different proteins could fold properly (**Supplementary Fig. S2.1A**).

To further establish that the catalytic activity of SIRT5 is necessary for the interaction with Nsp14, we used a recently described, potent and specific SIRT5 inhibitor (Sirt5-i) (34). This inhibitor has a published IC_{50} of 0.11 μM, and we measured an IC_{50} of 0.44 μM in desuccinylation assays *in vitro* (**Supplementary Fig. S2.1B**). *SIRT5*-KD cells were transfected with Nsp14 and SIRT5 and incubated with increasing concentrations of Sirt5-i. The binding of SIRT5 was lost at high concentrations of Sirt5-i, with the interaction almost absent at 25 and 100 μM (**Fig. 2.2C**). This observation again suggested that the SIRT5 catalytic activity was necessary for the interaction. Notably, until now, Sirt5-i had not been characterized in cell culture. This experiment suggested that Sirt5-i could be efficiently used in cells, with a putative IC_{50} of approximately 10 μM. Next, we tested whether the interaction depended on cellular NAD levels. NAD is a necessary co-substrate, and SIRT5 activity is highly correlated with cellular NAD levels. In cells, most NAD is synthesized through the NAD salvage pathway (35). Treating cells with the NAMPT inhibitor FK866 blocks the rate-limiting step in the pathway and rapidly depletes NAD levels, and supplementing cells with the NAD precursor nicotinamide mononucleotide (NMN) rescues the depletion (36) (**Supplementary Fig. S2.1C**). *SIRT5*-KD cells were transfected for 24 hours with Nsp14 and SIRT5 and for an additional 24 hours with FK866 and/or NMN (**Fig. 2.2D**). SIRT5 binding was highly reduced in the presence of FK866

(low NAD levels), but the binding was rescued in presence of NMN, and appeared slightly stronger when cells were treated with NMN alone (high NAD levels). This finding indicated that the interaction of Nsp14 and SIRT5 positively correlated with cellular NAD levels. Altogether, by directly inhibiting SIRT5 or modulating the level of its co-substrate NAD, these experiments confirmed that SIRT5 catalytic activity was necessary for the interaction with Nsp14.

Finally, we determined if Nsp14 was directly modified by SIRT5 and if we could detect changes in the levels of acetylation, succinylation or malonylation. *SIRT5*-KD cells were transfected with SIRT5, Nsp14 and/or a GFP expression control. After affinity purification, pan-acetylation/succinylation/malonylation antibodies were used to detect changes in the levels of different lysine modifications (**Fig. 2.2E**). Independent of the presence of SIRT5, we detected no measurable changes in acetylation, succinylation or malonylation, either among input or purified proteins. Weak bands were observed for purified GFP and Nsp14, but the intensity of the signal was not affected by the presence or absence of SIRT5, suggesting that it is not specific. Pan-modification antibodies are often not very sensitive, and we tested whether we could detect changes in lysine modifications by mass spectrometry. Nsp14-strep was transfected in *SIRT5*-KD cells, purified by affinity purification, and analyzed by mass spectrometry. The experiment was done with and without SIRT5 co-transfection, in three biological replicates each. In both conditions, Nsp14 had high coverage (65% coverage in presence of SIRT5, 88% without SIRT5), and we confirmed the interaction of Nsp14 with the two human proteins GLA and IMDH2 as reported (1). However, despite 94% of lysine residues being covered (28 out of 30) and high quality of the data, we found no acetylated, succinylated, malonylated or glutarylated sites. We detected a previously characterized phosphorylation site at serine 56 (37) and a nitrosylation site on tyrosine 351. Since SIRT5 is the only known cellular desuccinylase, demalonylase, and

deglutarylase, we had hoped that analyzing Nsp14 post-translational modifications in the presence or absence of SIRT5 would reveal changes in the level of these acylations marks. On the contrary, the absence of detectable acetylation, succinylation, malonylation and glutarylation suggested that Nsp14 was not directly modified by SIRT5. This series of experiments revealed that, even though SIRT5 catalytic activity is necessary for the interaction with Nsp14, Nsp14 did not appear to be a direct target of SIRT5.

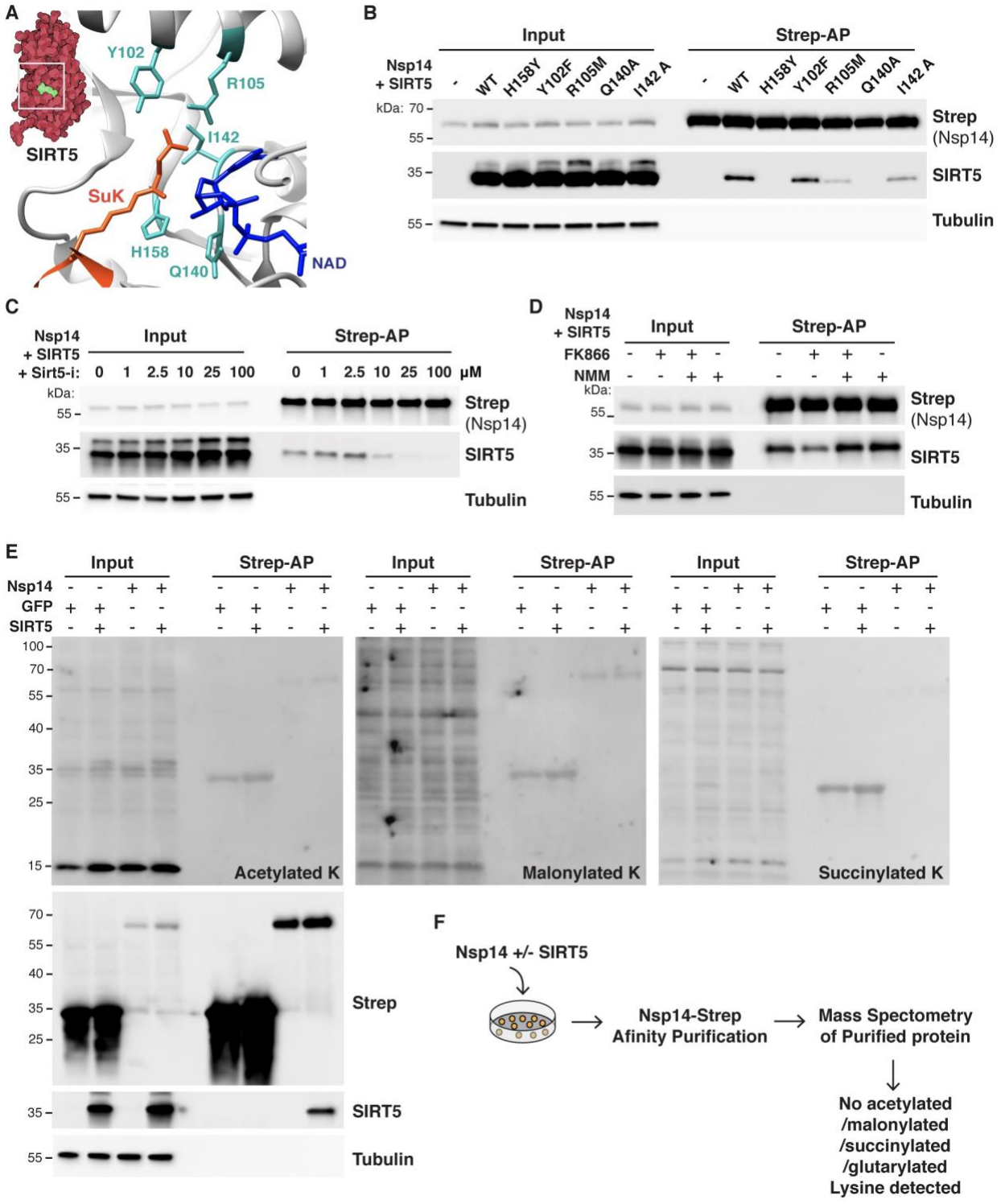

Figure 2.2: SIRT5 catalytic activity is necessary to interact with Nsp14.
A. Cartoon representation of the protein structure of SIRT5 catalytic site in complex with cofactor NAD and succinylated lysine substrate (SuK), showing conserved residues mutated in panel B. B. Strep-tag affinity-purification and western blot after transfection of *Sirt5*-KD HEK293T cells with Nsp14-strep and (Figure caption continued on the next page.)

(Figure caption continued from the previous page.) SIRT5 catalytic mutants, showing that the interaction with Nsp14 is lost in several mutants. C. Strep-tag affinity-purification and western blot after transfection with Nsp14-strep and SIRT5, in *SIRT5*-KD HEK293T cells incubated with increasing concentrations of SIRT5 inhibitor Sirt5-i. High concentrations of Sirt5-i prevent the interaction. D. Strep-tag affinity-purification and western blot after transfection with Nsp14-strep and SIRT5, in *SIRT5*-KD HEK293T cells incubated with NAMPT FK866 inhibitor (low cellular NAD), FK866 and NMN, or NMN alone (high cellular NAD). SIRT5 binding strength correlated with NAD levels. E. Pan-acetylation, malonylation and succinylation in *SIRT5*-KD HEK293T total or Strep-purified proteins, after transfection with Nsp14-Strep, GFP-strep control and/or SIRT5. No specific lysine modifications could be detected. F. Summary of mass spectrometry experiments. Nsp14-strep proteins purified from *SIRT5*-KD HEK293T, with or without co-transfection with SIRT5, were analyzed by mass spectrometry. No acetylation, malonylation, succinylation or glutarylation modifications could be detected.

Nsp14 also interacts with SIRT1

The seven human sirtuins share conserved domains, and we tested whether Nsp14 also interacts with the other sirtuins. We found that Nsp14 interacted with SIRT1, but not with SIRT2, 3, 6 or 7 (**Fig. 2.3A**). We could not investigate the interaction with SIRT4 because we lacked a specific antibody. The signal from SIRT1 was specific but appeared weaker than with SIRT5, which might explain why it was not detected by mass spectrometry (1). Interestingly, and as we observed with SIRT5, mutating SIRT1 catalytic domain or treating cells with the SIRT1 inhibitor Ex-527 eliminated the interaction (**Fig. 2.3B, C**). This finding suggested again that SIRT1 catalytic activity is necessary for the interaction with Nsp14. By contrast, treating cells with the specific SIRT1 activator SRT1720 or the non-specific activator Resveratrol had no measurable effect on Nsp14 binding (**Fig. 2.3D, E**). Both activators were toxic to cells at high concentrations, and the apparent decrease in binding after affinity purification correlated with reduced levels of Nsp14 and SIRT5 in input lanes.

To uncover a putative molecular function of the Nsp14-SIRT5 interaction, Nsp14 and SIRT5 were expressed in *E. coli* and purified. Unfortunately, and even though the complex could be readily observed in mammalian cells, we could not reconstitute it *in vitro* with purified proteins, either by column chromatography or gel electrophoresis. This was the case when the

two proteins were expressed separately and purified, or when co-expressed in *E. coli*. This observation suggests that the *in vitro* conditions that we used were inadequate and that additional parameters in mammalian cells were likely missing, such as other protein cofactors, post-translational modifications, or specific buffer conditions. Even though the complex could not be observed *in vitro*, we determined if the enzymatic activities of SIRT5 or Nsp14 were perturbed when in presence of each other. We measured the desuccinylation activity of SIRT5 alone or when incubated with increasing concentrations of Nsp14, using an *in vitro* desuccinylation assay. We detected no changes in desuccinylation activity in presence of Nsp14, whereas adding known inhibitors, such as nicotinamide or the specific SIRT5 inhibitor Sirt5-i, completely inhibited the activity (**Fig. 2.3F**). Similarly, we used a methyltransferase assay to characterize the MTase activity of Nsp14 in presence of SIRT5. This assay measures the conversion of the methyl donor S-adenosyl methionine (SAM) into S-adenosyl homocysteine and can be used to measure the activity of any SAM-dependent methyltransferase. Nsp14 methylates the mRNA cap and Nsp14 was incubated with an unmethylated GpppG cap-analog, in presence of SAM, NAD and increasing concentrations of SIRT5 (**Fig. 2.3G**). The Nsp14/Nsp10 complex and Nsp14 alone had similar activities, as predicted. We detected a small 10% increase of methyltransferase activity with excess SIRT5, but this increase persisted in presence of the SIRT5 inhibitor Sirt5-i. Since we showed above that Sirt5-i disrupted the interaction (**Fig. 2.3G**), this small increase might not be specific. Besides, Nsp14 ExoN activity depends on Nsp10, and Nsp14 has no ExoN activity by itself. We showed that Nsp10 and SIRT5 are parts of separate complexes (**Fig. 2.1F-G**), suggesting that the Nsp14/SIRT5 complex is very unlikely to have any ExoN activity either. Overall, these enzymatic assays failed to uncover a clear molecular function of the Nsp14/SIRT5 complex.

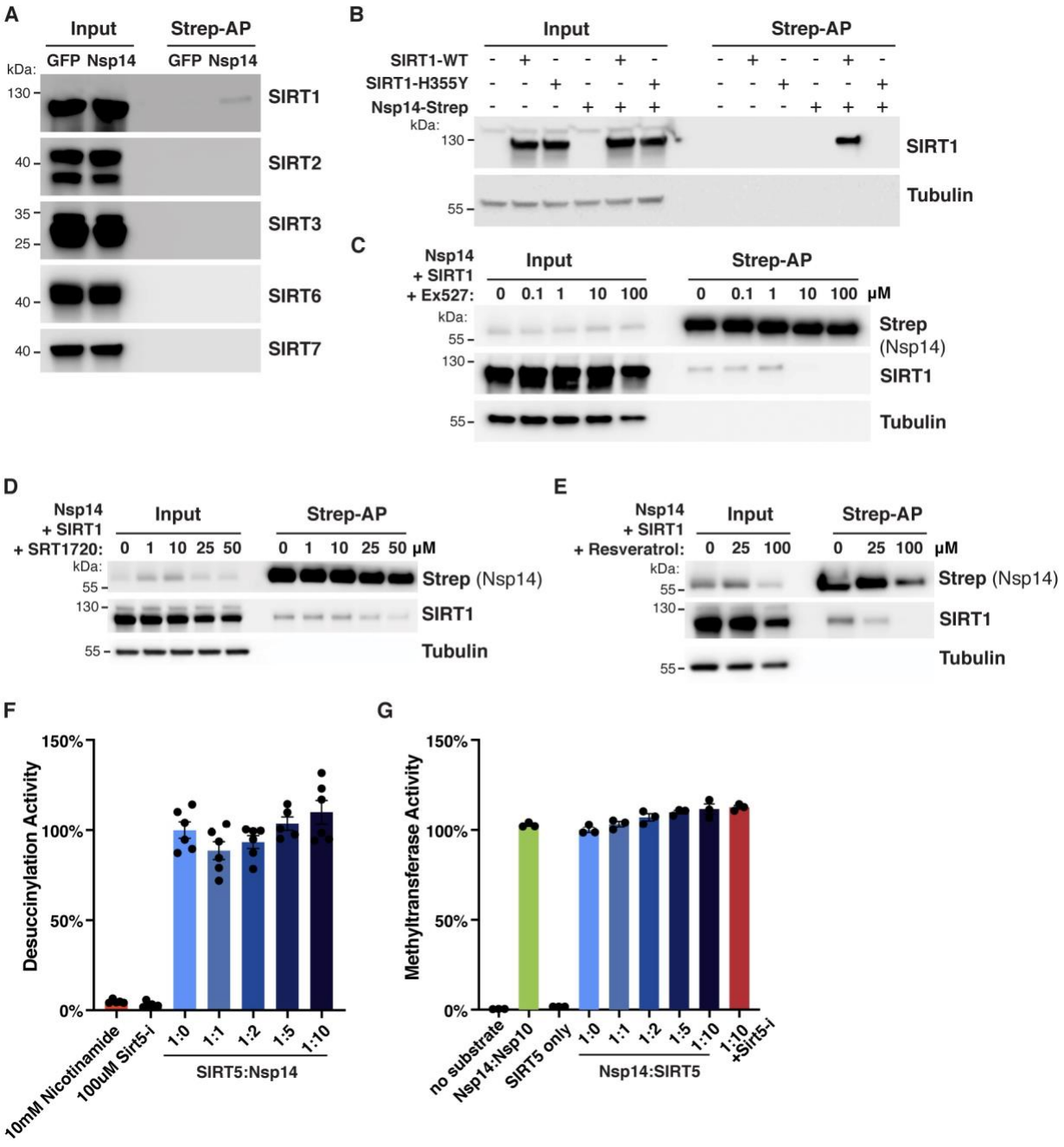

Figure 2.3: SARS-CoV-2 Nsp14 interacts with human SIRT1.
A. Co-purification of endogenous sirtuins SIRT1, 2 , 3, 6 and 7 after transfection of Nsp14-strep in HEK293T cells, as shown by western blot. Loading and purification controls are the same as in **Fig. 2.1B**. B. Strep-tag affinity-purification and western blot after transfection of HEK293T cells with Nsp14-strep and SIRT1 WT and H355Y catalytic mutant, showing that the interaction with Nsp14 is lost in H355Y mutant. C. Strep-tag affinity-purification and western blot after transfection with Nsp14-strep and SIRT1, in HEK293T cells incubated with increasing concentrations of SIRT1 inhibitor Ex-527. High concentrations of Ex-527 prevent the interaction. (Figure caption continued on the next page.)

(Figure caption continued from the previous page.) D-E. Strep-tag affinity-purification and western blot after transfection with Nsp14-strep and SIRT1, in HEK293T cells incubated with increasing concentrations of SIRT1 specific activator SRT1720 (D) or non-specific activator resveratrol (E). Both drugs were cytotoxic at high concentrations and the apparent decrease in SIRT1 binding correlated with a similar decrease in the input lanes. F. *In vitro* desuccinylation activity of purified SIRT5 incubated with increasing concentrations of Nsp14, showing no effect. G. *In vitro* methyltransferase activity of purified Nsp14 incubated with increasing concentrations of SIRT5, showing no specific effect. Unmethylated GpppG cap-analog was used as a substrate.

SIRT5 is a proviral factor

We next wanted to examine the role of SIRT5 during SARS-CoV-2 infection. We generated a *SIRT5* knockout (*Sirt5*-KO) in A549 cells overexpressing ACE2 (A549-ACE2), using CRISPR-Cas9 editing and three commercially designed guide RNAs. The knockout was generated by transfecting cells with Cas9-gRNA ribonucleoproteins, and cells transfected with Cas9 alone and no guide RNAs were used as wild-type (WT) controls. As expected, SIRT5 was undetectable in *SIRT5*-KO cells (**Fig. 2.4A**). WT and *SIRT5*-KO cells were infected with SARS-CoV-2 (Wuhan strain, USA/WA-1/2020 isolate) at a multiplicity of infection (MOI) of 0.1 and 1, and viral RNA was quantified by RT-qPCR after 3 days (**Fig. 2.4B**). At both MOIs, we observed a significant 2–3-fold decrease of SARS-CoV-2 mRNA in *SIRT5*-KO cells ($p<0.0001$ and $p=0.0002$ at MOI=0.1 and 1, respectively, by ANOVA). These results were confirmed by plaque assay, and we measured a significant sixfold decrease of viral titers in *SIRT5*-KO cells (**Fig. 2.4C**, $p<0.0001$, ANOVA). These observations suggested that SIRT5 is necessary for SARS-CoV-2 replication and/or propagation.

To confirm this result, A549-ACE2 cells were infected with SARS-CoV-2 in presence of the specific inhibitor Sirt5-i. Sirt5-i caused no measurable cytotoxicity (**Fig. 2.4D**) and significantly reduced cell-associated viral mRNA levels by almost twofold (**Fig. 2.4E**, $p=0.0001$ and $p<0.0001$ at 25 and 100 μM, respectively, ANOVA). Viral titers measured by plaque assay were also significantly reduced by fourfold in presence of Sirt5-i inhibitor (**Fig. 2.4F**, $p<0.0001$,

ANOVA). Human lung-cancer cells Calu-3 endogenously express ACE2 and are often considered a better model for SARS-CoV-2 infection. Calu-3 cells were infected with SARS-CoV-2 and treated with SIRT5 inhibitor Sirt5-i. Viral RNA levels were significantly reduced, with a twofold reduction in viral mRNA at 100 μM (**Fig. 2.4G**, p= 0.011, ANOVA). Viral titers measured by plaque assay were also significantly reduced by twofold in Calu3 cells in presence of Sirt5-i inhibitor (**Fig. 2.4H,** p=0.009). Altogether, this showed that knocking out or inhibiting SIRT5 resulted in a decrease in SARS-CoV-2 levels.

We obtained similar results with SIRT1. SARS-CoV-2 replication was reduced in *SIRT1*-KO A549-ACE2 cells, with a significant twofold decrease in mRNA levels (p=0.0002 and p=0.0011 at MOI = 0.1 and 1, respectively), and a significant twofold decrease in viral titers as well (**Fig. 2.4A-C, I,** p<0.0001). SIRT1 inhibitor Ex-527 significantly reduced viral titers by sixfold in A549-ACE2 cells, and by twofold in Calu3 cells (p<0.0001 and p=0.011, respectively, **Fig. 2.4E-H**). This showed that SIRT1 is also necessary for efficient SARS-CoV-2 infection. Interestingly, treating A549-ACE2 or Calu3 cells with both SIRT5 and SIRT1 inhibitors did not further reduce viral levels. Titers significantly decreased by two to fourfold in cells treated with Sirt5-I and Ex-527 together, a level similar to cells treated with the inhibitors alone (**Fig. 2.4F, H**). This suggested that the roles of SIRT1 and SIRT5 during SARS-CoV-2 infection might be interdependent or that they act in the same pathway. In summary, our observations indicated that SIRT5 and SIRT1 are proviral factors necessary for coronaviruses replication and/or propagation. The reduction of viral levels without SIRT1 was less pronounced and consistent than without SIRT5, and we focused the rest of our investigation on SIRT5.

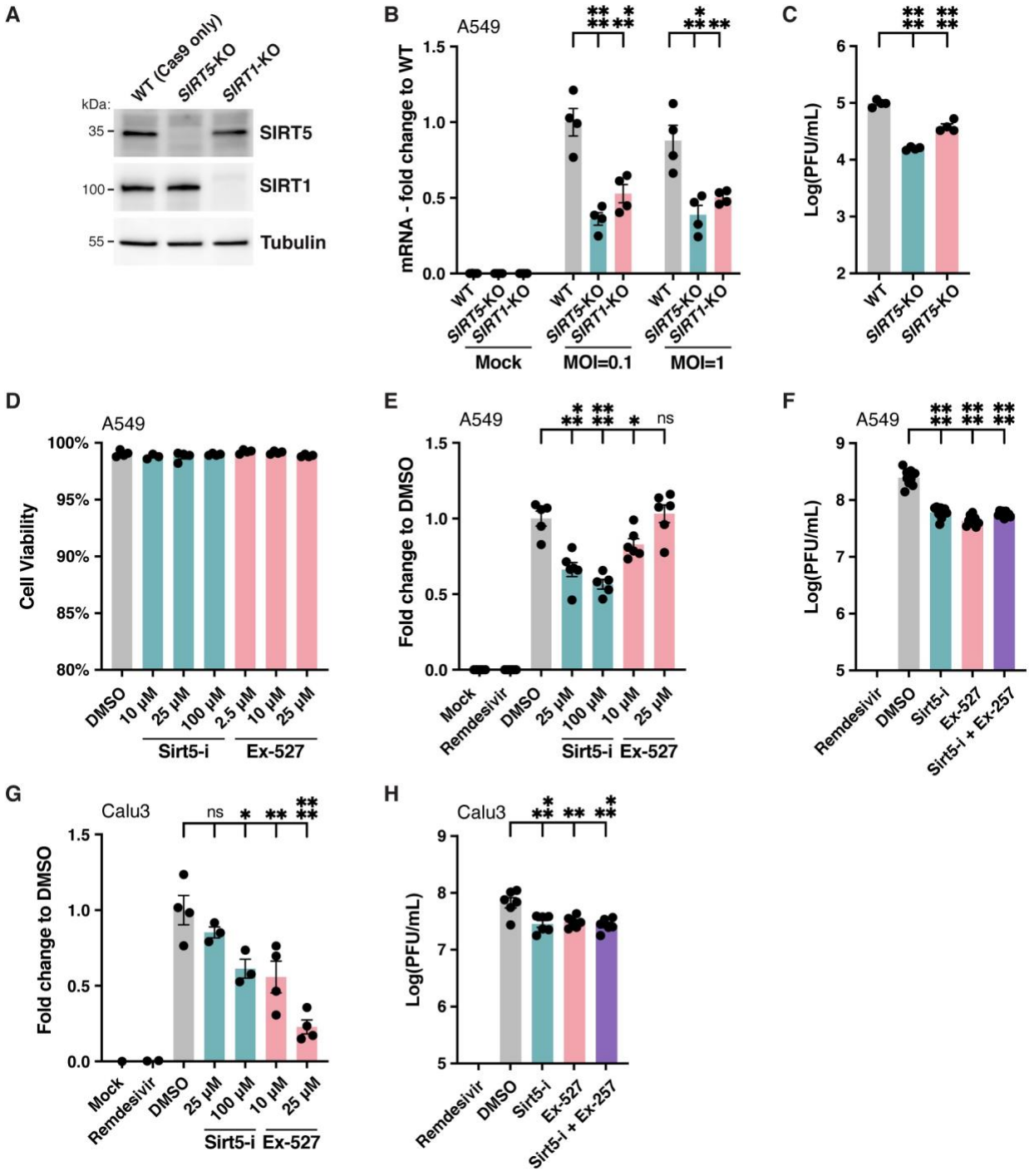

Figure 2.4: SIRT5 is a proviral factor

A. Western blot showing the absence of SIRT5 and SIRT1 in *SIRT5*- and *SIRT1*-KO A549-ACE2 cells, after CRISPR knockout. B. Decrease in cell-associated viral mRNA levels in *SIRT5*- and *SIRT1*-KO cells infected with SARS-Cov-2 for 3 days at MOI=0.1 or MOI=1, as shown by RT-qPCR. Data show fold-changes compared to WT levels at MOI=0.1. n=4. C. Decrease in viral titers in *SIRT5*- and *SIRT1*-KO cells infected with SARS-Cov-2 for 3 days at MOI=1, as shown by plaque assay. n=4. (Figure caption continued on the next page.)

(Figure caption continued from the previous page.) D. Absence of cytotoxicity in A549-ACE2 cells treated with Sirt5-i and Ex-527 inhibitor, as measured by flow cytometry. n=4. E. Decrease in cell-associated viral mRNA levels in A549-ACE2 cells infected with SARS-Cov-2 for 3 days at MOI=0.1, and treated with SIRT5 and SIRT1 inhibitors Sirt5-i and Ex-527, as shown by RT-qPCR. Data show fold-change compared to DMSO-treated levels. n=6. F. Decrease in viral titers in A549-ACE2 cells infected with SARS-Cov-2 for 3 days at MOI=0.1, and treated with SIRT5 and SIRT1 inhibitors Sirt5-i and Ex-527, as shown by plaque assay. n=9. G/H. Same as E. (with n=4), and F. (n=6), using Calu3 cells.
B-H. Data show mean and standard error of the mean (SEM) between biological replicates. RT-qPCR results were internally normalized with *GAPDH* and *ACTIN* reference genes. Viral titers after plaque assay are expressed in log-transformed PFU (plaque-forming unit) per mL of supernatant. Asterisks summarize the results of one-way ANOVAs followed by Holm–Šidák multiple comparisons test (on log-transformed data for plaque assays) *: $p < 0.05$, **: $p < 0.01$, ***: $p < 0.001$, ****: $p < 0.0001$.

SIRT5 proviral activity is partially independent of the interaction with Nsp14

To determine if the proviral role of SIRT5 could be explained by its interaction with Nsp14, we analyzed the role of SIRT5 during infection with human coronavirus HCoV-OC43, a distantly related beta-coronavirus. SIRT5 interacts with Nsp14 from SARS-CoV-2 and SARS-CoV, but not from MERS-CoV (2). Similarly, we observed by affinity co-purification in HEK293T cells that SIRT5 was not interacting with Nsp14 from HCoV-OC43 (**Fig. 2.5A**). This result further confirmed that SIRT5 interaction with Nsp14 is specific to SARS-like coronaviruses. Human colon adenocarcinoma cells HCT-8 were infected with HCoV-OC43 in presence of Sirt5-i inhibitor, and we observed a significant decrease in viral levels (**Fig. 2.5B, C**). At 100 μM, viral mRNA in the cell-culture supernatant and viral titers measured by plaque assay were both reduced 10-fold ($p=0.0021$ and $p < 0.0001$, respectively, ANOVA). This observation suggested that the role of SIRT5 during infection might be partially independent of its interaction with Nsp14.

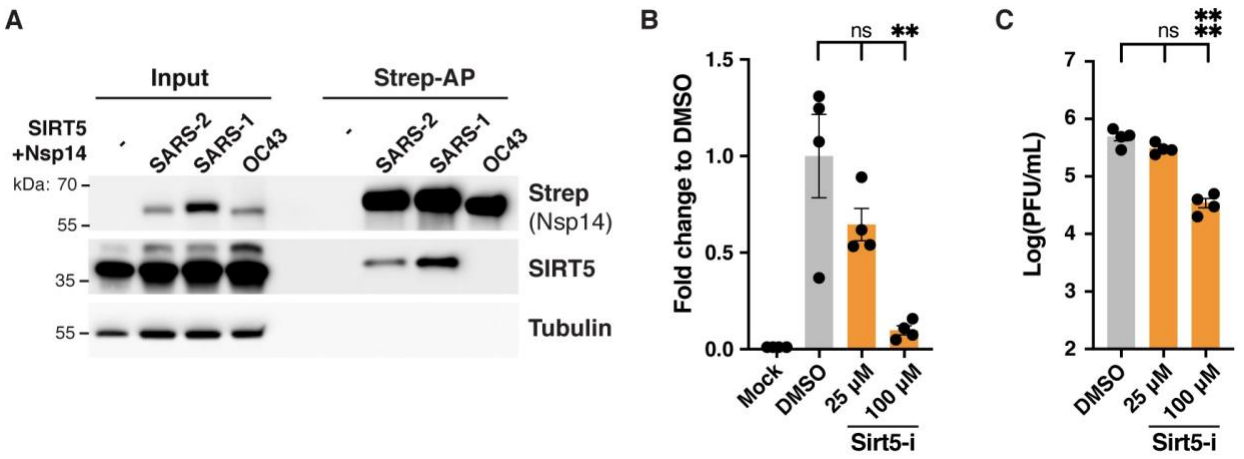

Figure 2.5: SIRT5 proviral activity is partially independent from the interaction with Nsp14

A. Strep-tag affinity-purification and western blot after transfection of *SIRT5*-KD HEK293T cells with SIRT5 and Nsp14-strep from different coronaviruses, showing that the interaction with SIRT5 is specific to SARS-like coronaviruses. B. Decrease in supernatant-associated viral mRNA levels in HCT-8 cells infected with HCoV-OC43 for 5 days at MOI=0.1, and treated with SIRT5 inhibitor Sirt5-i, as shown by RT-qPCR. Data show fold-change compared to DMSO-treated levels. n=4. C. Decrease in viral titers in HCT-8 cells infected with HCoV-OC43 for 5 days at MOI=0.1, and treated with SIRT5 inhibitors Sirt5-i, as shown by plaque assay. n=4. B-C. Data show mean and SEM between biological replicates. Asterisks summarize the results of one-way ANOVAs followed by Holm–Šidák multiple comparisons test (on log-transformed data for plaque assays) *: $p < 0.05$, **: $p < 0.01$, ***: $p < 0.001$, ****: $p < 0.0001$.

SIRT5 knockout cells express a higher basal level of viral restriction factors

To gain insight into the role of SIRT5 during SARS-CoV-2 infection, we performed RNA-seq in A549-ACE2 cells, WT and *SIRT5*-KO, after 3 days of infection with SARS-CoV-2 (MOI=1). Sequencing was done in four biological replicates for each condition. Principal-component analysis showed that samples separated well, based on knockout and infection status (**Supplementary Fig. S2.2A**). When comparing uninfected WT and *SIRT5*-KO cells, 1139 and 869 genes were significantly up- and downregulated, respectively (q-value threshold q=0.05). Most of these changes were modest, and only 69 genes were up- or downregulated by more than twofold (**Fig. 2.6A**, left panel). Gene Ontology and pathway enrichment analysis showed that up-regulated genes were principally involved in metabolism and, in particular, protein catabolism

processes in the lysosome, whereas down-regulated genes were involved in DNA replication and mitosis. These findings were in line with reports showing that SIRT5 is implicated in autophagy and controls cell proliferation in cancer cells by targeting multiple metabolic enzymes (31, 32, 38–41). In WT infected samples, around 5% of total reads mapped to the SARS-CoV-2 genome, indicating substantial and successful viral replication. Despite this high level of viral expression, we observed a muted response to infection, at least in WT cells (**Fig. 2.6A**, middle panel). SARS-CoV-2 efficiently evades innate immune defense through multiple mechanisms, and this absence of a strong transcriptional response is characteristic of SARS-CoV-2 infection and has been documented in numerous studies (42–44). For example, we could not detect induction of *IFN-α*, *IFN-β*, *CXCL10*, interleukin *IL-6* or tumor necrosis factor (*TNF*). When comparing WT infected and WT mock-infected samples, 275 and 385 genes were significantly up- and down-regulated, respectively (threshold q=0.05), with only the chemokine *CXCL8* (IL-8) and the transcription factor *ATF3* being increased with a fold-change higher than 2 (**Fig. 2.6A**, middle). Gene Ontology and pathway enrichment analysis indicated that genes involved in response to virus infections were upregulated, with the two most upregulated pathways being the NOD-like and RIG-I-like receptors signaling pathways, which are implicated in the intracellular recognition of viruses. Notably, other studies that reported a higher number of differentially expressed genes often had higher levels of viral infection, with a fraction of SARS-CoV-2 reads of 10–50%, compared to 5% in this study. This might explain why the transcriptional response that we observed is comparatively smaller (42, 45).

We next analyzed the effect of *SIRT5* knockout on SARS-CoV-2 infection. SARS-CoV-2 levels were almost fourfold less in *SIRT5*-KO infected cells than in WT infected cells, confirming that SIRT5 is a proviral factor ($q=8.4 \times 10^{-13}$, **Fig. 2.6B**). We focused our analysis on

the 3221 genes that were differentially expressed between at least two of the four conditions (threshold q=0.01). Hierarchical consensus clustering of the differentially expressed genes generated eight clusters, representing groups of genes that behaved similarly between the different sample conditions (**Fig. 2.6C, D**). Enrichment analysis of biological gene sets then allowed the identification of the cellular pathways over-represented in the identified clusters (**Fig. 2.6E**). For example, clusters 2 and 3 corresponded to genes with a lower expression in *SIRT5*-KO cells, independently of the infection status, and pathways linked to the cell cycle and cellular metabolism were significantly enriched in these clusters. In most of the clusters (clusters 2–6), pathways linked to cellular metabolism were significantly enriched, highlighting that SIRT5 is an important metabolic enzyme. Clusters 7 and 8 were particularly interesting. They represent genes that are expressed at a higher basal level in *SIRT5*-KO cells, and whose expression is further increased during infection (**Fig. 2.6C, D**). Strikingly, pathways linked to innate immunity, such as type I and II interferon and NFκB signaling, were significantly enriched in these clusters (**Fig. 2.6E**). Genes in clusters 7 and 8 are up-regulated in *SIRT5*-KO cells, even in uninfected cells, which suggested that *SIRT5*-KO cells had a higher basal level of innate immunity markers and could mount a stronger immune response.

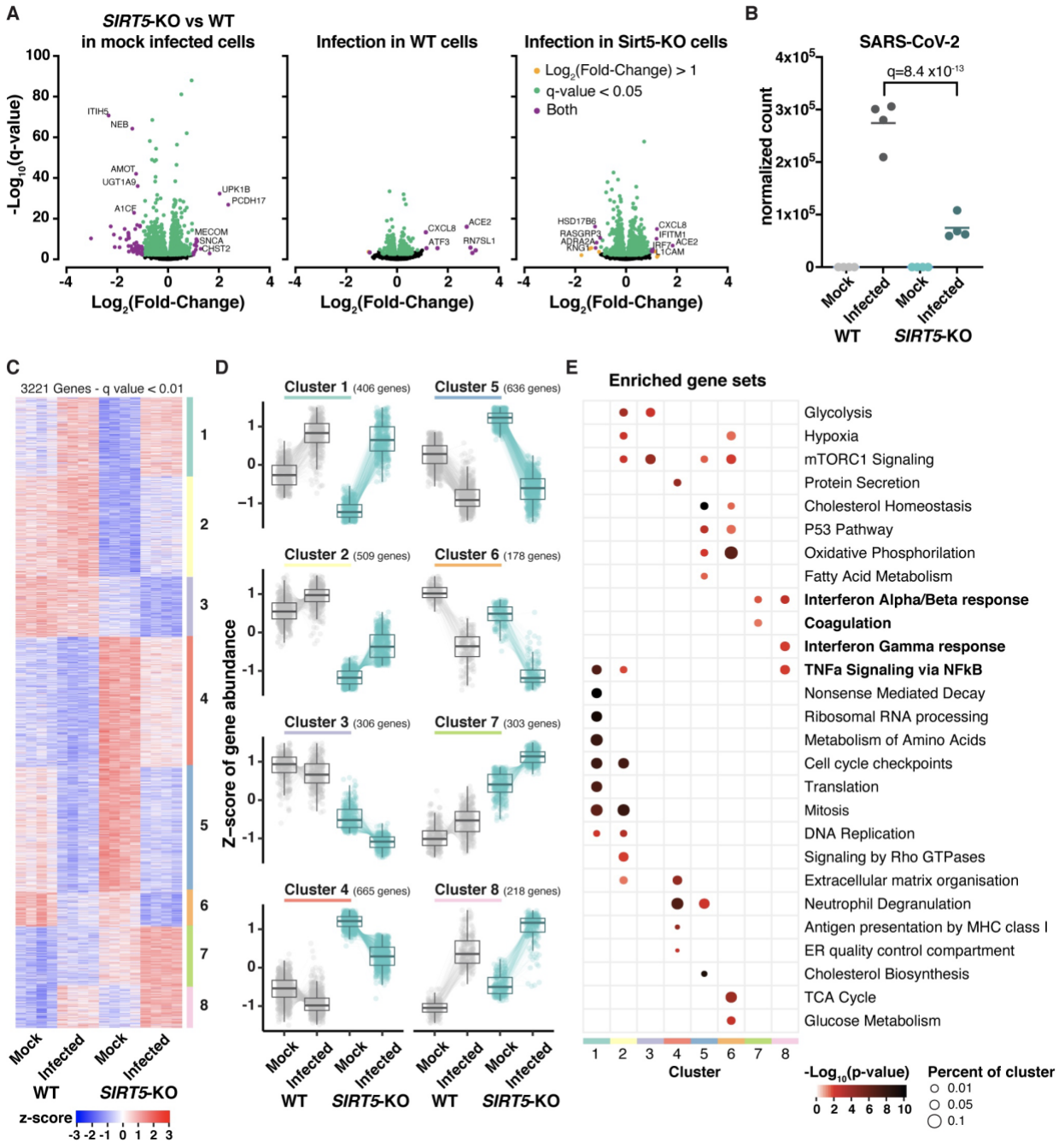

Figure 2.6: *SIRT5*-KO cells mount a stronger innate immune response
RNA-seq analysis of WT and *SIRT5*-KO A549-ACE2 cells infected or mock-infected for 3 days with SARS-CoV-2 at MOI=1. n=4. A. Volcano plots showing differentially expressed genes between the different conditions. Highlighted genes display a q-value q<0.05 (green), log2 fold-change >1 (orange), or both (purple). Left panel: *SIRT5*-KO vs WT in mock-infected cells. Middle: Infected vs mock-infected WT cells. Right: Infected vs mock-infected *SIRT5*-KO cells. B. Normalized gene count of SARS-CoV-2. C-D. Unsupervised clustering of the 3221 genes differentially expressed between at least two of the four conditions (q<0.01). C: heatmap of normalized expression. (Figure caption continued on the next page.)

(Figure caption continued from the previous page.) D. Z-scores of differentially expressed genes as grouped by clustering. Colored lines represent the quantification of an individual gene whereas solid black lines show the cluster Tukey boxplot. E. Enrichment analysis of biological gene sets in the identified gene clusters (C and D).

We thus investigated whether innate immunity pathways were up-regulated in *SIRT5*-KO cells, even without viral infection. In mock-infected cells, the Gene Ontology term "Innate Immune Response" was significantly enriched in *SIRT5*-KO samples (q=0.0071, Supplementary Table S3). Type-I interferon responses are one of the most important lines of defense against viruses. We analyzed the expression of known Type-I interferon-stimulated genes, as well as of other genes broadly linked to innate immune responses and present in clusters 7 and 8 (**Fig. 2.7A**). As could be expected, most of these genes were upregulated in infected cells. Strikingly, many of these genes, which are normally involved in the response to pathogens, were also upregulated in *SIRT5*-KO cells in absence of infection, with 39 out of the 71 selected genes being significantly upregulated in mock-infected *SIRT5*-KO cells ($q < 0.05$). Many of these genes were expressed at similar levels between infected WT cells and mock-infected *SIRT5*-KO cells, and were further increased in infected *SIRT5*-KO cells (**Fig. 2.7A**). This included cytokines (*IL33*, *CXCL5*, and *CSF1*), the transmembrane restriction factors *IFITM2* and 3, members of the complement system (*C1S*, *C1R* and *C3*), the MHC class I subunit *B2M*, and other interferon-stimulated genes or restriction factors (e.g., *IFIT3*, *TRIM22*, *STAT3*, *MMP7*, *LCN2*, *MUC5AC*, *SLFN5*, *NT5E*, *CAST* and *SNCA*) (46–52). The upregulation between WT and *SIRT5*-KO in mock-infected cells was modest but statistically significant, ranging from 20 to 50%, and was further increased up to twofold in infected *SIRT5*-KO cells (**Fig. 2.7A, Supplementary Fig. S2.2A**). These results suggest that *SIRT5*-KO cells express a higher basal level of numerous restriction factors and mount a stronger antiviral response, which could explain why SARS-CoV-2 levels are decreased in absence of SIRT5.

To confirm these observations, we validated by RT-qPCR the upregulation of several restriction factors between WT and *SIRT5*-KO cells, in absence of infection (**Fig. 2.7B**). This confirmatory analysis was done with new samples and independently of the RNA-seq experiment, using eight biological replicates per group to increase statistical power and measure subtle effects. The cytokines *IFN-β* and *IL33* were significantly upregulated two to threefold in *SIRT5*-KO cells ($p=0.0004$, and $p<0.0001$, respectively, t-test). Other markers such as *STAT3, IFIT3* and *B2M* showed modest but statistically significant upregulation ranging from 20 to 70%, while *IFITM2* and *SCNA* had increased expression that did not reach statistical significance. These results confirmed that *SIRT5*-KO cells express a higher basal level of viral restriction factors.

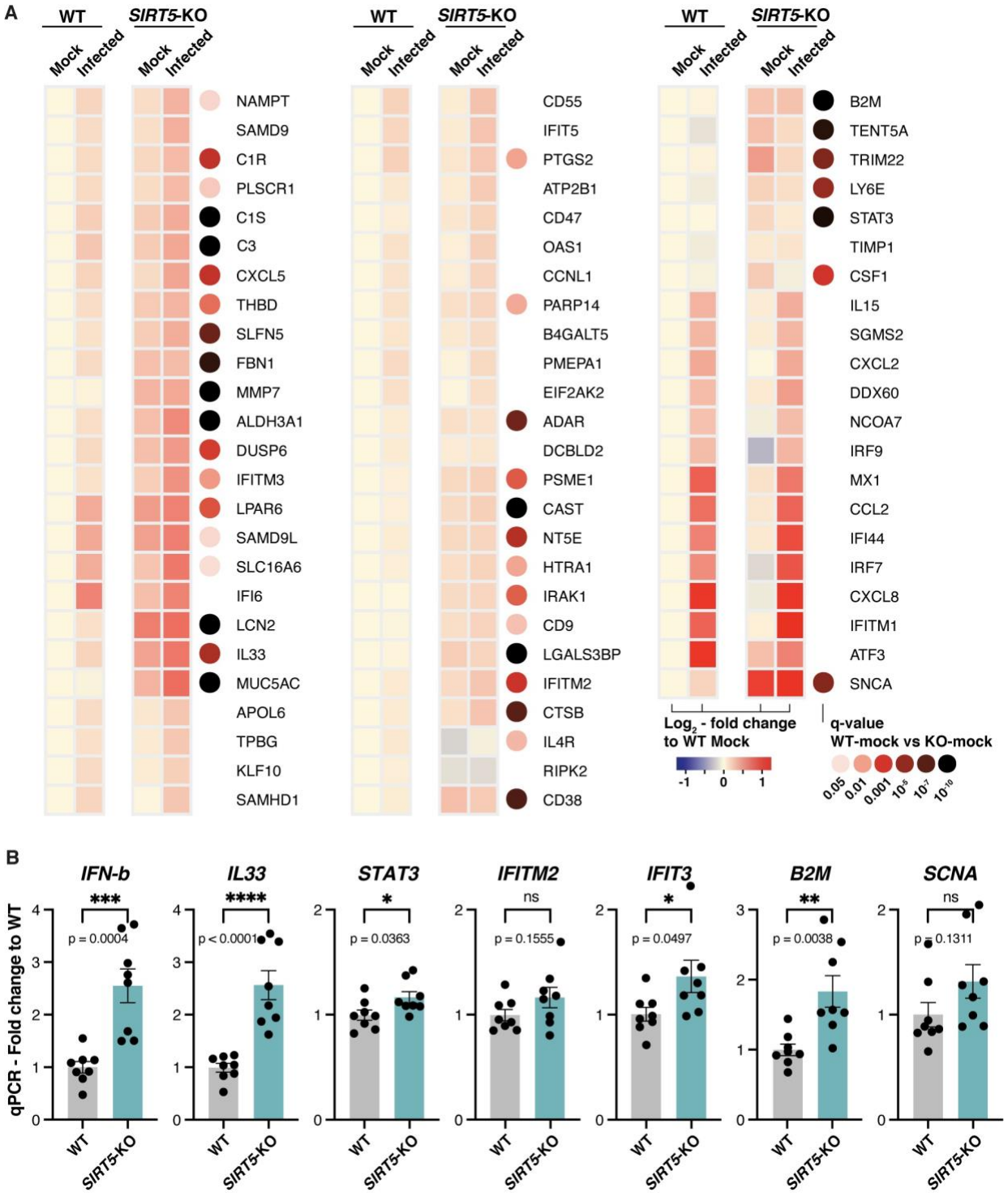

Figure 2.7: *SIRT5*-KO cells express a higher basal level of viral restriction factors
A. Expression heatmap of interferon-stimulated genes and other restriction factors, showing that mock-infected *SIRT5*-KO cells express higher basal levels of restriction factors, and that antiviral responses are stronger in *SIRT5*-KO cells. Data show mean log2 fold-change, compared to mock-infected WT, (Figure caption continued on the next page.)

(Figure caption continued from the previous page.) and the q-value between mock-infected WT and *SIRT5*-KO cells. Only genes differentially expressed between at least two conditions were included in the analysis (q<0.01). B. RT-qPCR confirmation of restriction factors upregulated in non-infected *SIRT5*-KO cells (n=8). Data show fold-changes compared to WT levels after normalization with *ACTIN*. Data show mean and SEM between replicates. p-values after unpaired two-tailed t-test are shown and asterisks summarize the results. *: $p < 0.05$, **: $p < 0.01$, ***: $p < 0.001$, ****: $p < 0.0001$.

SIRT5 proviral activity is independent of the MAVS signaling pathway

SIRT5 is implicated in RIG-1/MAVS antiviral signaling, a key innate immune pathway that recognizes viral RNA in the cytosol and activates type I interferon. Specifically, SIRT5 desuccinylate MAVS and reduce MAVS aggregation on the mitochondrial surface, resulting in lower interferon activation (**Supplementary Fig. S2.3A**) (30). To explain the reduced viral replication in *SIRT5*-KO cells, we hypothesized that SIRT5 absence could lead to stronger MAVS aggregation and in turn a stronger antiviral response. To test this hypothesis, we used CRISPR-Cas9 to delete MAVS in A549 cells stably co-expressing ACE2 and TMPRSS2 (A549-A/T cells). A549-A/T cells can be infected more efficiently and represent an improvement over cells expressing ACE2 only, and were used for this experiment. Cells were transduced with a lentiviral vector expressing Cas9 and a gRNA against *MAVS,* which resulted in a 90% knockdown of MAVS by western blot (**Fig. 2.8A**). *MAVS* knockdown (*MAVS*-KD) cells were then infected with SARS-CoV-2 in presence or absence of SIRT5 inhibitor (**Fig. 2.8B**). *MAVS* knockdown resulted in a three to five-fold increase in viral levels in both DMSO or Sirt5-i-treated cells ($p<0.0001$, ANOVA), indicating that MAVS is implicated in the antiviral response against SARS-CoV-2, independently of SIRT5. If SIRT5 was acting primarily by reducing MAVS activation, inhibiting SIRT5 in *MAVS*-KD cells would be expected to have little effect. However, we found that inhibiting SIRT5 had the same effect in WT and *SIRT5*-KO cells, with a significant reduction of titers of about twofold in both WT and *MAVS*-KD cells ($p=0.0052$ and

$p<0.0001$, respectively, ANOVA). This important result invalidated our hypothesis and suggested that SIRT5 role in innate immunity is not limited to regulating MAVS. In fact, this showed that SIRT5 function during SARS-CoV-2 infection is likely independent of the RIG-I/MAVS pathway.

Finally, we wanted to elucidate whether Nsp14 played a role in modulating SIRT5 proviral activity. A549 cells cannot be transfected efficiently, and we attempted to generate cell lines expressing Nsp14. Nsp14 is cytotoxic, and we could not build cell lines stably expressing Nsp14 from a constitutive lentiviral vector. To circumvent this toxicity issue, we used doxycycline-inducible Nsp14 and GFP lentiviral vectors. A549-ACE2 WT and *SIRT5*-KO cells were transduced with inducible Nsp14 and GFP constructs, and cells were successfully selected with puromycin. In absence of doxycycline, cells stably transduced with inducible Nsp14 had no apparent replicative or morphological defects. As expected, doxycycline treatment induced a strong overexpression of *GFP*, with a 2000-fold induction compared to basal levels as measured by RT-qPCR (**Fig. 8C**). However, we did not observe any change in *Nsp14* expression after doxycycline treatment. The continuous puromycin selection ensured that the lentivirus vector had been stably integrated, but *Nsp14* induction was nonetheless not functional. It is possible that leaky basal expression of *Nsp14* in absence of doxycycline was sufficient to negatively select against permissive integration events. Unfortunately, these results prevented us from further investigating if Nsp14 could impact SIRT5 activity in cells.

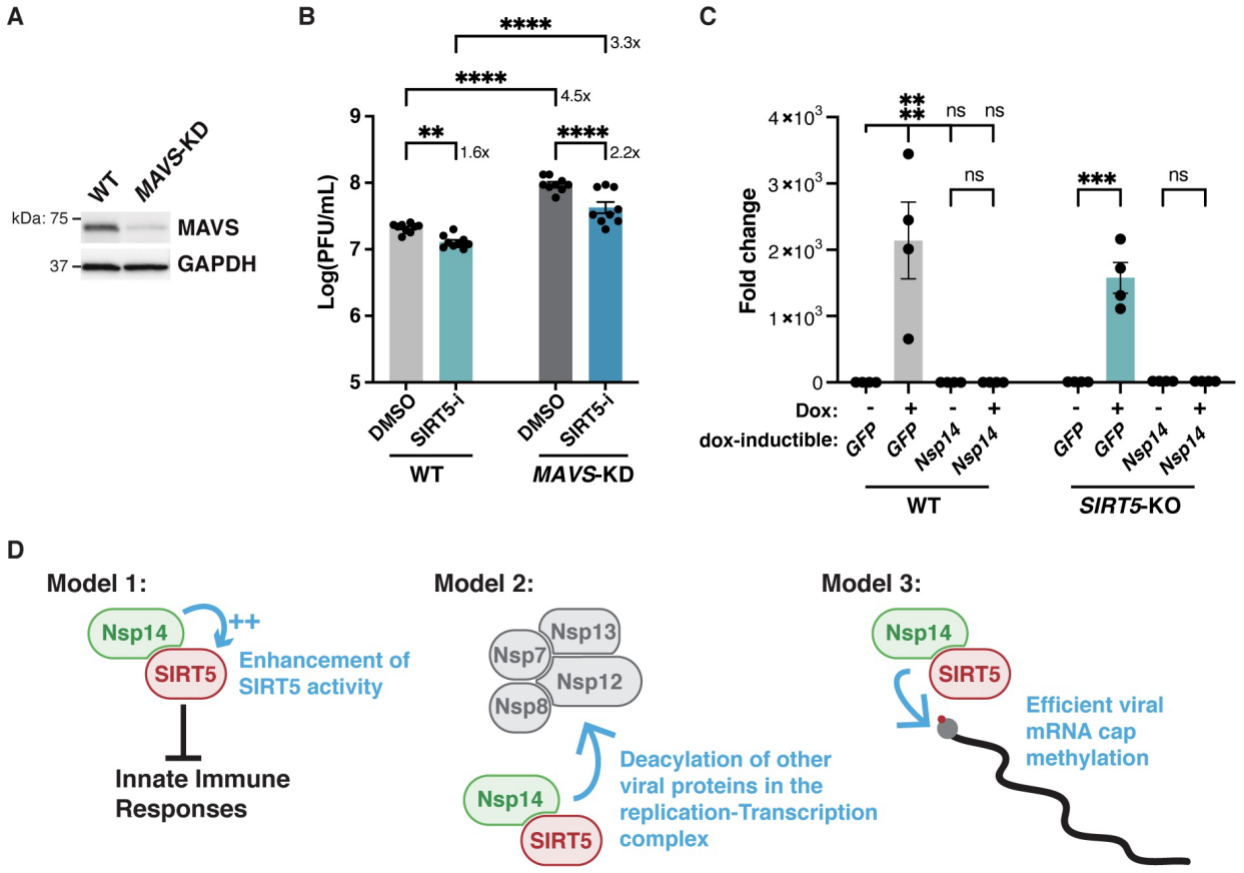

Figure 2.8: SIRT5 proviral activity is independent of the MAVS signaling pathway.
A. Western blot showing 90% reduction of MAVS in A549-A/T cells transduced with a CRISPR lentivirus against MAVS. A549-A/T cells stably co-express ACE2 and TMPRSS2. B. Viral titers in *MAVS*-KD cells treated with DMSO or SIRT5 inhibitor Sirt5-i, after infection with SARS-Cov-2 for 3 days at MOI=0.1, as shown by plaque assay. Sirt5-i had a similar effect in WT and *MAVS*-KO, suggesting that SIRT5 function is independent of MAVS. n=9. C. RT-qPCR of *GFP* or *Nsp14* after doxycycline induction. WT and *SIRT5*-KO A549-ACE2 cells were stably transduced with doxycycline-inducible constructs for GFP and Nsp14. After doxycycline treatment for 48 hours at 100ng/mL, *GFP* was strongly overexpressed, but *Nsp14* failed to be expressed. Data show fold-changes compared to the first column (WT cells transduced with GFP without doxycycline), after normalization with *ACTIN*. n=4. D. Hypotheses for the role of the SIRT5/Nsp14 interaction during SARS-CoV-2 infection. In model 1, Nsp14 could enhance SIRT5 activity, which would decrease innate immune responses and favor viral replication. In model 2, Nsp14 could redirect SIRT5 to novel targets, potentially in the replication-transcription complex, where SIRT5 could deacylate other viral proteins. In model 3, the Nsp14/SIRT5 complex could be primarily involved in mRNA cap methylation. Absence or inhibition of SIRT5 would lead to incomplete cap methylation and stronger immune recognition of viral mRNA.
B-C. Data show mean and SEM between biological replicates. Asterisks summarize the results of one-way ANOVAs followed by Holm–Šidák multiple comparisons test (on log-transformed data for plaque assays). *: $p < 0.05$, **: $p < 0.01$, ***: $p < 0.001$, ****: $p < 0.0001$.

Discussion

In this study, we investigated the role of SIRT5 during SARS-CoV-2 infection. Our results show that SIRT5 interacts with the non-structural viral protein Nsp14, and that this interaction is independent of Nsp10. Interestingly, we found that the catalytic activity of SIRT5 was necessary for the interaction, as several SIRT5 catalytic mutants could not bind to Nsp14, and the interaction was blocked by specific SIRT5 inhibitors. SIRT5 is the main cellular desuccinylase, demalonylase, and deglutarylase, but we could not detect these lysine modifications on Nsp14 protein, suggesting that Nsp14 is not directly modified by SIRT5. We further showed that SIRT5 is a proviral factor and that SARS-CoV-2 levels decrease when SIRT5 is deleted or inhibited in cell-culture experiments, independently of the MAVS signaling pathway. We observed that *SIRT5*-KO cells express innate immunity markers at a higher basal level and mount a stronger antiviral response, which might explain the decrease in viral levels. Taken together, our study uncovered a novel and unexpected role for SIRT5 during SARS-CoV-2 infection.

The interaction between SIRT5 and Nsp14 is intriguing. Mutating the SIRT5 catalytic domain or treating cells with a SIRT5 inhibitor blocked the interaction (**Fig. 2.2B, C**), and the strength of the interaction appeared to be modulated by cellular NAD levels (**Fig. 2.2D**). NAD is necessary for SIRT5 activity, and these results highlight that SIRT5 catalytic activity or at the very least a functional catalytic domain is necessary to interact with Nsp14. SIRT5 binds to some of its targets in co-purification experiments, such as with MAVS, SHMT2, or PKM2 (30–32). However, in these examples, SIRT5 was also desuccinylating the target proteins. Here we found no lysine modifications on Nsp14, either by mass spectrometry or immunoblotting. Our experiments might not have been sensitive enough to detect it, but our mass spectrometry data

had very high purity, covered 94% of Nsp14 lysine residues, and our pipeline routinely detects such modifications. Besides, SIRT5 is the only known desuccinylase, demalonylase, and deglutarylase, and these experiments were performed in *SIRT5*-KD cells, which would have enriched the presence of these lysine modifications if they were present. The unusual nature of the interaction might explain why we were unable to reconstitute the complex *in vitro* with proteins purified in *E. coli,* and why our enzymatic assays failed to uncover a clear molecular function. Interestingly, an interaction of a similar nature has been described between SIRT1 and the HIV viral protein Tat (53, 54). Tat interacted with the SIRT1 catalytic domain and mutation of conserved residues disrupted the interaction. In this case however, Tat was deacetylated by SIRT1 and blocked SIRT1 activity. Here, we could not determine if SIRT5 activity was altered by Nsp14, and global succinylation and malonylation levels appeared unaffected as well (**Fig. 2.2E**). Further studies will be necessary to understand the nature of the interaction and its function. They could reveal a novel interaction mechanism, in which an enzyme binds to a partner through its catalytic domain, which has rarely been observed.

The role of SIRT5 and other sirtuins in disease is unclear. SIRT5, by modulating key metabolic enzymes, could be involved in cancer (31, 32, 38–41). *SIRT5*-KO mice display no obvious phenotype and mount strong innate immune responses against several bacterial infections (55). The role of SIRT5 and other sirtuins during viral infection is understudied and likely depends on the pathogen. Knocking out SIRT5 enhances the replication of several DNA viruses, such as herpes simplex 1, human cytomegalovirus and adenovirus type 5, and the same study reported a potential increase in influenza replication, albeit non-significantly (56). By contrast, here we showed that inhibition or deletion of SIRT5 led to a decrease in viral levels with two distinct coronaviruses, SARS-CoV-2 and HCoV-OC43, indicating that SIRT5 is a

proviral factor in this context (**Fig. 2.4, 2.5**). A recent study showed that replication of vesicular stomatitis virus (VSV) and Sendai virus (SeV), two negative-strand RNA viruses, was also diminished in absence of SIRT5 (30). Whether SIRT5 broadly acts as a restriction factor against DNA viruses and as a proviral factor against RNA viruses will be an interesting hypothesis to investigate in the future.

The decrease of SARS-CoV-2 levels in *SIRT5*-KO cells correlated with elevated basal levels of numerous viral restriction factors, even in mock-infected cells (**Fig. 2.7**). This upregulation was modest but highly significant and may account for why SARS-CoV-2 propagated slower in *SIRT5*-KO cells. Several hypotheses could explain this elevation of innate defenses. SIRT5 has been directly implicated in the RIG-I/MAVS pathway, a critical component of the innate sensing of RNA virus (**Supplementary Fig. S2.3A**) (30). Recognition of cytosolic RNA molecules by RIG-I-like receptors, including RIG-I and MDA5, causes recruitment of MAVS, which forms large aggregates on the surface of mitochondria, ultimately leading to type I IFN production (57). MAVS is succinylated upon viral challenge with VSV and SeV, and desuccinylation of MAVS by SIRT5 diminishes MAVS aggregation, resulting in lower interferon activation. By preventing MAVS aggregation, SIRT5 therefore enhances viral replication, at least with VSV and SeV (30). However, by infecting *MAVS*-KD cells in presence of SIRT5 inhibitor, here we showed that SIRT5 likely acts independently of MAVS during SARS-CoV-2 infection (**Fig. 2.8B**). Besides, SARS-CoV-2 efficiently counteracts MAVS activation of innate defense. The coronavirus proteins M, Orf9b and Orf3b directly antagonize MAVS aggregation or downstream signaling (58–60), and MAVS knockout was reported to have no effect on SARS-CoV-2 replication (43). Our results indicated otherwise, but altogether this suggests that the desuccinylation of MAVS by SIRT5 is not the main mechanism for explaining the decrease of

viral levels in *SIRT5*-KO cells. Other mechanisms could be involved. For example, SIRT5 is involved in the detoxification of reactive oxygen species (ROS) and attenuates cellular ROS levels (27). Elevated ROS levels activate innate immune responses, and the absence of SIRT5 could cause the activation of innate immune responses through this pathway (61). Furthermore, SIRT5 regulates proteins involved in glycolysis, the TCA cycle, and fatty acid oxidation. These pathways were impaired without SIRT5, as well as mTOR signaling (**Fig. 2.6E**). mTOR and the cellular sensing of energy and nutrient levels can directly influence immune activity (62), highlighting another pathway that could lead to immune activation in absence of SIRT5.

The potential link between our two key findings, namely the Nsp14/SIRT5 interaction and the proviral role of SIRT5, will be the subject of further investigation. Several hypotheses can be considered (**Fig. 2.8D**). First, Nsp14 might work by enhancing SIRT5 activity, which would favor viral replication by dampening innate immune responses. In this model, increased deacylation of cellular targets of SIRT5 could result in a weaker immune response and favor viral replication. Second, Nsp14 could redirect SIRT5 toward novel targets, for example other viral proteins. Nsp14 is part of the viral replication-transcription complex, and SIRT5 could be involved in the deacylation of other members of the complex such as Nsp7, Nsp8, Nsp12 or Nsp13. Third, we observed that SIRT5 and Nsp10 were part of separate complexes, and that Nsp14 MTase activity increased slightly in presence of SIRT5 (**Fig. 2.3G**). SIRT5 and Nsp10 could be separately involved in the two enzymatic activities of Nsp14, with the Nsp14/SIRT5 complex primarily responsible for viral mRNA Cap methylation. Absence of SIRT5 would result in a defect in cap methylation, more efficient immune recognition of viral RNA, and stronger immune response, as we observed.

To summarize, further studies will be necessary to elucidate how SIRT5 enhances SARS-CoV-2 replication, and how the interaction with Nsp14 plays in this context. Potent inhibitors of SIRT5 are in development, and SIRT5 is a potential target against cancer (34, 40, 63). Our manuscript highlights that SIRT5 is a potential pharmaceutical target that could help against viral infections as well, and SARS-CoV-2 in particular. Currently, very few antiviral drugs are approved. Inhibiting SIRT5 will probably never represent a first line of defense, but it could be used in combination with drugs that directly target viral enzymes, leading to novel therapeutic regimens against COVID-19.

Materials and Methods

Mammalian cell lines and culture conditions

All cell lines were maintained at 37 °C in a 5% CO_2 humidified incubator. Cells were frequently tested for mycoplasma contamination and consistently tested negative.

HEK293T cells were obtained from ATCC (Cat. CRL-11268) and maintained in high glucose Dulbecco's minimal Eagle's medium (DMEM) with 10% fetal bovine serum (FBS) (Sigma-Aldrich, USA) and 100 μm/L penicillin-streptomycin (Corning, USA). Calu3 cells were obtained from ATCC (Cat. HTB-55) and cultured in AdvancedMEM (Gibco, USA), supplemented with 2.5% FBS (GeminiBio, USA), 1% GlutaMax, and 100 μm/L penicillin-streptomycin. Wild-type A549 cells were purchased from ATCC (Cat. CCL-185). A549 cells stably expressing ACE2 (A549-ACE2) were a gift from O. Schwartz (Pasteur Institute, Paris). A549-ACE2 cells were cultured in DMEM, supplemented with 10% FBS (GeminiBio, USA) and blasticidin (20 μg/ml) (Sigma-Aldrich, USA). Short-terminal repeat (STR) analysis by the Berkeley Cell Culture Facility on 17 July 2020 authenticated these as A549 cells with 100% probability. Vero-E6 cells were obtained from ATCC (Cat. CRL-1586) and cultured in DMEM (Corning, USA), supplemented with 10% FBS (GeminiBio, USA), 1% glutamine (Corning), and 100 μm/L penicillin-streptomycin (Corning). HCT-8 cells (ATCC Cat. CCL-244) were cultured in DMEM with 10% FBS and penicillin-streptomycin.

Plasmids

Plasmids expressing GFP and Nsp14 proteins (from SARS-CoV-2, SARS-CoV and HCoV-OC43) with a C-terminus strep tag were a gift from Nevan Krogan (1, 2), and are also available on Addgene (pLVX-EF1alpha-SARS-CoV-2-nsp14-2xStrep-IRES-Puro, Addgene

#141380). Nsp10-Flag plasmid was a gift from the Ott lab. Doxycycline-inducible plasmids were also a gift from the Krogan lab.

Mammalian expression plasmids for SIRT5 and SIRT5-H158Y with a myc-his tag in a pCDNA 3.1 vector were available in the Verdin lab (26). Y102F, R105M, Q140A and I142A mutants were generated by Q5 site-directed mutagenesis (NEB, USA).

Generation of CRISPR cell lines

Stable cell lines transduced with lentiviral vectors were generated as follow: lentiviruses expressing the constructs of interest were produced in HEK293T cells by standard protocols (64). Cells were plated and transduced 24h later at low MOI when 50-80% confluent. Puromycin, hygromycin or other selection antibiotics were added 48h later and cells passaged at least three time in presence of antibiotics before being used for experiments.

The *SIRT5* knockdown (*SIRT5*-KD) cell line was generated using CRISPR interference in HEK293T cells. First, we generated a stable cell line expressing dCas9-KRAB-MeCP2. Early passage HEK293T cells were transfected with 1.5 μg of dCas9-KRAB-MeCP2 repressor plasmid (Addgene #110824) and 0.5 μg of Piggyback Transposase (gift from Maxim Greenberg), using PEI 25K transfection reagent (Polysciences Inc, Cat. 23966-1), according to the manufacturer's instructions. Cells stably expressing dCas9-KRAB-MeCP2 were selected with Blasticidin (Invivogen, USA) for 10 days before generating *SIRT5*-KD cells. Second, sequences for sgRNA against human *SIRT5* (5'- GGCGCTCCGGACCTGAGCCA-3') or non-targeting sgRNA (5'-GCTGCATGGGGCGCGAATCA-3') were obtained from Horlbeck et al. (65) and cloned into Addgene #84832 by annealing and ligation using T4 ligase. Plasmids were validated by Sanger sequencing (Elim Biopharmaceuticals. HEK293T cells expressing dCas9-KRAB-MeCP2 were transduced with lentiviruses expressing the gRNAs in medium containing 1 μg/ml polybrene and

30% lentivirus-containing supernatant (v/v). Cells were then selected with Blasticidin at 5 μg/mL and Puromycin (1 μg/mL, Invivogen, USA) to select for cells stably expressing both dCas9 and the sgRNAs. Stable knockdowns were validated by western blot.

The *SIRT5* knockout (*SIRT5*-KO) cell line was generated using CRISPR-Cas9 editing in A549-ACE2 cells. sgRNAs were commercially designed by Synthego (Redwood, California, USA) and are designed to work cooperatively to generate small-fragment deletions in early exons causing knockout. We combined 10 pmol of *Streptococcus pyogenes* NLS-Sp.Cas9-NLS (SpCas9) nuclease (Aldevron, USA, Cat. 9212) with 30 pmol of total synthetic sgRNA (10 pmol each sgRNA) to form ribonucleoproteins (RNPs) in 20 μL of total volume with SE Buffer for A549-ACE2 cells. The RNP assembly reaction was mixed by pipetting up and down and incubated at room temperature for 10 minutes. Cells were resuspended in transfection buffer, according to cell type, added to the preformed RNP solution, and gently mixed. Nucleofections were performed on a Lonza nucleofector system (Lonza, Switzerland, Cat. AAU-1001), using program CM-120 for A549-ACE2 cells. Cells were grown for several passages and genotyped by PCR and Sanger sequencing to confirm efficient editing. Absence of SIRT5 was confirmed by western blot.

A549 cells stably co-expressing ACE2 and TMPRSS2 (A549-A/T) were generated through sequential transduction of A549 cells with TMPRSS2-encoding (generated using Addgene plasmid #170390, a gift from Nir Hacohen) and ACE2-encoding (generated using Addgene plasmid #154981, a gift from Sonja Best) lentiviruses and selection with hygromycin (250 μg/mL) and blasticidin (20 μg/mL) for 10 days, respectively. ACE2 and TMPRSS2 expression was verified by western blot. CRISPR/Cas9-mediated deletion of MAVS was accomplished using lentiviral transduction. A gRNA specific to the third exon of the *MAVS* gene

was designed using Benchling.com and cloned into the lentiCRISPR v2 plasmid (Addgene #52961, gRNA sequence: 5'-GCTGGTAGCTCTGGTAGACAG-3'). A549 A/T were transduced with lentiviruses packaged with control (annotated WT) or MAVS-targeting gRNAs in the presence of polybrene (Sigma, TR-1003-G). Cells were selected with Puromycin for seven days and MAVS reduction was validated by western blot.

Transfection, Strep affinity purification, and Flag immunoprecipitation in HEK-293T cells

HEK-293T cells were plated in six-well plates or 10-cm dishes. After 24 hours, cells were transfected using polyethylenimine (PEI). Nsp14 is cytotoxic, and we used 0.5 μg of Nsp14-strep plasmid for a six-well plate and 4 μg for a 10-cm dish. Other co-transfecting plasmids, such as pcDNA-SIRT5, were used at the same concentration except when specifically mentioned. The total amount of plasmid was normalized using empty vectors when necessary. Plasmids were complexed with PEI in Opti-MEM medium (Thermofisher) at a 1:3 ratio, and the mixture was deposited onto cells dropwise. After 48 hours, cells were washed once with PBS, scraped off the plate by thorough pipetting, pelleted by centrifugation at 200g and 4 °C for 3 minutes, and frozen at −80 °C.

Affinity purification followed the methods of Gordon et al. 2020 (1). Frozen cell pellets were thawed on ice and resuspended in 0.5 ml of lysis buffer (IP buffer: 50 mM Tris-HCl, pH 7.4, 150 mM NaCl, and 1 mM EDTA), supplemented with 0.5% Nonidet P40 substitute (NP40; Fluka Analytical) and cOmplete mini EDTA-free protease and PhosSTOP phosphatase inhibitor cocktails (Roche)). Samples were frozen on dry ice for 10–20 minutes and partially thawed at 37 °C before incubation on a tube rotator for 30 minutes at 4 °C, and centrifugation (13,000g, 4 °C, 15 minutes) to pellet debris. 30 μL of "input" was saved and frozen at −80 °C. 20 μL of MagStrep 'type3' beads (IBA Lifesciences) were equilibrated twice with 1 mL of wash buffer (IP

buffer supplemented with 0.05% NP40) and incubated with 0.5 ml of lysate for two hours at 4 °C on a tube rotator. Tubes were placed on a magnetic rack, and beads were washed three times with 1 ml of wash buffer, and samples were shortly vortexed between washes. Bound proteins were eluted for 30 minutes using 30 µL of BXT elution buffer (IBA Lifesciences) with constant shaking at room temperature. Tubes were placed back on the magnetic rack, and the eluate was recovered and frozen at −80 °C.

Flag-immunoprecipitation was performed the same way using Anti-FLAG M2 Magnetic Beads (Sigma-Aldrich M8823) and elution was done using 3x-Flag peptide (Sigma-Aldrich F4799) at a concentration of 3 µg/50µL in IP buffer. When performing side by side Strep-affinity purification and Flag-immunoprecipitation, the same frozen cell sample was divided in two after lysis.

Western blot

Western blot was performed using standard protocols. Briefly, protein lysate was mixed with 4x Laemmli sample buffer containing DTT and boiled for 5 minutes at 95 °C. Proteins were separated on a precast 4–20% gradient gel (Biorad, USA) and transferred on a nitrocellulose membrane using a semi-dry Trans-Blot Turbo Transfer System and Trans-Blot Turbo Transfer Buffer (Biorad, USA). Membranes were blocked for 1 hour with 5% milk in TBST (Tris-buffered saline and Tween 20) buffer, rinsed, and incubated overnight at 4 °C with primary antibodies in 2% BSA in TBST. Membranes were washed three times with TBST and incubated for 2 hours at room temperature with horseradish peroxidase–linked secondary antibody. The chemiluminescent signal was revealed with SuperSignal West Pico PLUS Substrate (ThermoFisher, USA) and imaged with an Azure 600 Imaging system (Azure Biosystem, USA).

Cellular Thermal Shift Assay (CETSA)

CETSA was performed as described (66). Shortly, HEK-293T cells in six wells were transfected with plasmids expressing Nsp14-strep and/or SIRT5. After 48 hours, cells were harvested, washed with PBS, and resuspended in PBS supplemented with EDTA-free complete protease inhibitor cocktail (Roche). Intact cells were divided into 100-µl aliquots and heated individually at different temperatures for 3 minutes in a PCR machine (Biorad), followed by cooling for 2 minutes at room temperature. Cell suspensions were freeze-thawed three times with liquid nitrogen, and the soluble fraction was separated from the cell debris by centrifugation at 20,000 × g for 20 minutes at 4 °C. Supernatants containing soluble proteins were transferred to new microcentrifuge tubes and analyzed by western blot.

Immunofluorescence

A549 cells plated in an eight-well chamber slide (Nunc Lab-Tek II, Thermo Fisher) were transfected with 500 ng of nsp14-strep plasmid encoding nsp14-strep using Lipofectamine 3000 (Thermo Fisher). The next day, cells were fixed in PBS-buffered 4 % formaldehyde at room temperature. After 15 minutes, cells were briefly rinsed with PBS once and incubated in permeabilization buffer (0.1 % Triton X-100 in PBS). After 15 additional minutes, cells were incubated in blocking buffer (permeabilization buffer supplemented with 1 % BSA), and further incubated in blocking buffer containing anti-Strep mouse antibody (1:1000 dilution), and anti-SIRT5 rabbit antibody (1:1000 dilution). The next day, the cells were washed with PBS three times and incubated in the blocking buffer containing anti-mouse IgG donkey antibody conjugated with Alexa 488 (1:500 dilution, Thermo Fisher), anti-rabbit IgG donkey antibody conjugated with Alexa 555 (1:500 dilution, Thermo Fisher), and for counter-staining, DAPI (1 µg/ml, Sigma Aldrich) and Phalloidin conjugated with Alexa 647 (1: 1000 dilution, Abcam).

After 30 minutes, the cells were washed with PBS three times, and mounted in prolong gold anti-fade (Thermo Fisher), followed by curing overnight. The cells were visualized using a confocal fluorescence microscope (LSM 700, Carl Zeiss) at 63 X magnification, imaged, and analyzed using ZEN imaging software (blue edition, Ver 3.4, Carl Zeiss).

Protein purification and enzymatic assays

Nsp10 and Nsp14 proteins from the Wuhan strain of SARS-CoV-2 (NC_045512.2) were codon-optimized, ordered as Gblocks (IDT), and cloned into a pVFT1S expression vector using a HiFi DNA Assembly kit (NEB). Both nsp10 and nsp14 contained an N-terminal 6x-His tag, followed by a TEV cleavage site. *E. coli* BL21*(DE3) cells (Invitrogen, USA) were transformed with the nsp10 and nsp14 expression vectors and grown in LB medium containing kanamycin. Cells were induced at an OD_{600} of ~0.8 with 0.5 mM IPTG for 16 hours at 16°C. Nsp10 pellets were stored at -20°C, and nsp14 pellets were flash-frozen with liquid nitrogen and stored at -80°C until use. For nsp10/14 copurification, nsp10 pellets from 1 L of cells and nsp14 pellets from 6 L of cells were resuspended in lysis buffer (50 mM HEPES, pH 7.5, 300 mM NaCl, 5 mM $MgSO_4$, 30 mM imidazole, and 1% NP-40) and combined. For nsp14 purification, pellets were resuspended in lysis buffer. The pellets were lysed using sonication and clarified using centrifugation at 14,500 rpm for 40 minutes at 4°C. The supernatant was loaded onto a HisTrap HP column (GE Healthcare, USA). Proteins were purified by fast protein liquid chromatography and washed using two column volumes of Ni Buffer A (50 mM HEPES, pH 7.5, 300 mM NaCl, 5 mM $MgSO_4$, and 30 mM imidazole). For nsp10/14 copurification only, an additional wash was done over five column volumes using a buffer of 50 mM HEPES, pH 7.5, 300 mM NaCl, 5 mM $MgSO_4$, and 60 mM imidazole. Proteins were eluted using 50 mM HEPES, pH 7.5, 300 mM NaCl, 5 mM $MgSO_4$, and 300 mM imidazole. The elution was then concentrated and purified

further using a Superdex 200 column (GE) and a buffer of 10 mM HEPES, pH 7.5, 150 mM NaCl, and 10% glycerol. The purified protein was then concentrated, flash-frozen using liquid nitrogen, and stored at -80°C.

SIRT5 purified protein was obtained commercially (BPS Bioscience, USA, Cat. 50016). In vitro desuccinylation assays were performed using Fluorogenic SIRT5 Assay Kit (BPS Bioscience, USA, Cat. 50085), following the manufacturer's instructions. Methyltransferase assays were performed using MTase-Gl Methyltransferase Assay (Promega, USA), following the manufacturer's instructions. Nsp14 and SIRT5 recombinant proteins were first incubated together in the reaction buffer, with a ratio of 1:1 corresponding to 100 nM of each protein. Desuccinylation assays were performed in a reaction buffer (25 mM Tris/HCl, pH 8.0, 137 mM NaCl, 2.7 mM KCl, 1 mM $MgCl_2$, and 0.1 mg/ml BSA) with 0.5 mM NAD+ for 30 minutes at 37°C. Methyltransferase assays were performed in reaction buffer (50 mM Hepes, pH 7.0, 6 mM KCl, 2 mM DTT, 1 mM $MgCl_2$, and 0.1 mg/ml BSA) in presence of 0.1 mM NAD+ and 10 µM SAM.

Sample Preparation for Proteomic Analysis

HEK-293T *SIRT5-KD* cells were transfected with plasmids expressing Nsp14-strep in the presence or absence of SIRT5 with 3 biological replicates for each condition. Nsp14-strep and bound proteins were purified by affinity purification as described above, and eluted in 35 µL of elution buffer (100 mM Tris pH 7.4; 150 mM NaCl; 1 mM EDTA; 50 mM biotin). Each sample was subjected to a lysis buffer containing 5% SDS and 50 mM triethylammonium bicarbonate (TEAB) for proteomics sample preparation.

The samples enriched for NSP14 were reduced with 20 mM dithiothreitol (DTT) in 50 mM TEAB buffer at 50 °C for 10 minutes, left to cool at room temperature for 10 minutes, and

alkylated with 40 mM iodoacetamide (IAA) in 50 mM TEAB buffer in the dark at room temperature for 30 minutes. Samples were acidified with a final concentration of 1.2% phosphoric acid. Subsequently, 90% methanol in 100 mM TEAB was added. The entire sample volume was spun through the micro S-Trap columns (Protifi) to bind the proteins to the S-Trap column. The S-Trap columns were washed again with 90% methanol in 100 mM TEAB. S-Trap columns were placed in a clean elution tube and incubated with trypsin digestion buffer (50 mM TEAB, pH ~8) at a 1:25 ratio (protease:protein, wt:wt) for 1 hour at 47 °C. The same volume of trypsin digestion buffer was added again for an overnight incubation at 37 °C. Peptides were eluted from the S-Trap column first with 50 mM TEAB spun through at 1,000 x g, then with 50 mM TEAB and 0.5% formic acid at 1,000 x g, and finally with 50% acetonitrile in 0.5% formic acid at 4,000 x g. These pooled elutions were dried in a vacuum concentrator and then re-suspended in 0.2% formic acid. The re-suspended peptide samples were desalted with stage tips generated in-house using C18 disks. They were subsequently dried again in a vacuum concentrator, and re-suspended in aqueous 0.2% formic acid containing "Hyper Reaction Monitoring" indexed retention time peptide standards (iRT, Biognosys).

Mass Spectrometry Analysis

Briefly, samples were analyzed by reverse-phase HPLC-ESI-MS/MS using an Eksigent Ultra Plus nano-LC 2D HPLC system (Dublin, CA) with a cHiPLC system (Eksigent) which was directly connected to a quadrupole time-of-flight (QqTOF) TripleTOF 6600 mass spectrometer (SCIEX, Concord, CAN). After injection, peptide mixtures were loaded onto a C18 pre-column chip (200 µm x 0.4 mm ChromXP C18-CL chip, 3 µm, 120 Å, SCIEX) and washed at 2 µl/min for 10 min with the loading solvent (H_2O/0.1% formic acid) for desalting. Subsequently, peptides were transferred to the 75 µm x 15 cm ChromXP C18-CL chip, 3 µm, 120 Å, (SCIEX), and

eluted at a flow rate of 300 nL/min with a 3 h gradient using aqueous and acetonitrile solvent buffers.

Data-dependent acquisitions: For peptide and protein identifications the mass spectrometer was operated in data-dependent acquisition (DDA) mode, where the 30 most abundant precursor ions from the survey MS1 scan (250 msec) were isolated at 1 m/z resolution for collision-induced dissociation tandem mass spectrometry (CID-MS/MS, 100 msec per MS/MS, 'high sensitivity' product ion scan mode) using the Analyst 1.7 (build 96) software with a total cycle time of 3.3 sec as previously described (67)

Data Processing: Mass spectrometric data-dependent acquisitions (DDA) were analyzed using the database search engine ProteinPilot (SCIEX 5.0 revision 4769) allowing for biological modifications and with 'emphasis' on succinylation. A fasta file was generated appending the viral NSP14 protein sequence to the human proteome fasta file. A confidence score threshold of 99 was set to filter for high quality peptide identifications.

SARS-CoV-2 virus culture and Infections

SARS-CoV-2 isolate USA-WA1/2020 (BEI NR-52281) was used for all infection studies. All live virus experiments were performed in a Biosafety Level 3 laboratory. SARS-CoV-2 stocks were propagated in Vero-E6 cells, and their sequences were verified by next-generation sequencing. Viral stock titer was measured by plaque assays.

For infection experiments, A549-ACE2 or Calu3 cells were seeded into 12- or 24-well plates and rested for at least 24 hours prior to infection. At the time of infection, medium containing compound and/or viral inoculum (MOI 0.01 or 0.1) was added to the cells. After 3 days, the supernatant was collected and mixed with two volumes of RNA STAT-60 extraction

buffer (AMSbio, UK). Cells were similarly harvested by adding RNA STAT-60 extraction buffer. Samples were stored at -80°C.

Infections of HCT-8 cells with HCoV-OC43 were performed similarly.

Plaque assays

Viral inoculations were harvested from experiments and serially diluted in DMEM (Corning). At the time of infection, the media on Vero-E6 cells were replaced with viral inoculation for 1 hour. After the 1-hour absorption period, 2.5% Avicel (Dupont, RC-591 was layered on the cells and incubated for 72 hours. Then, Avicel was removed and cells were fixed in 10% formalin for 1 hour, stained with crystal violet for 10 minutes, and washed multiple times with water. Plaques were counted and averaged from two technical replicates.

RNA extraction and RT-qPCR

RNA in cells and supernatants resuspended in RNA STAT-60 buffer was extracted using Direct-zol RNA Miniprep kit (ZymoResearch, USA). For extraction from the supernatant, RNA was eluted in 20 µL of water, and 18 µL was directly used for reverse-transcription. RNA extracted from cells was DNAse-treated, eluted in 30 µL quantified by Nanodrop, and 2 µg of RNA was used reverse-transcription. Reverse-transcription was performed using the High-Capacity cDNA Reverse Transcription Kit (ThermoFisher), and quantitative PCR was done using a BioRad qPCR machine and Sybr Green (ThermoFisher). RT-qPCRs were normalized using the ΔΔCt method with the reference genes *ACTIN* and *GAPDH*. Missing data points in RT-qPCR figures represent samples where RNA extraction was of poor quality. No outliers were removed.

Statistics and reproducibility

Experiments were carried out in multiple replicates. For affinity-purification and western blot data, one representative experiment out of several replicates is shown. For statistical analysis

of RT-qPCR data, we used ordinary one-way ANOVA, followed by Holm–Šidák multiple comparisons test, with a single pooled variance. For RT-qPCR in figure 7, we used unpaired two-tailed t-tests. Plaque assay data do not satisfy the normality condition required for parametric tests, but are closer to a lognormal distribution (68). As a consequence, statistical tests on plaque assay data were performed on log-transformed data. Analyses were run using GraphPad Prism version 9.1.2 for macOS (GraphPad Software, USA, www.graphpad.com). Exact p-values and summaries are reported in the text and figures, respectively.

RNA-sequencing preparation and analysis

Library preparation and sequencing were performed by the DNA Technologies and Expression Analysis Core at the UC Davis Genome Center (Davis, CA, USA), supported by NIH Shared Instrumentation Grant 1S10OD010786-01. Strand-specific and barcode-indexed RNA-seq libraries were generated from 500 ng of total RNA each, after poly-A enrichment, using the Kapa mRNA-seq Hyper kit (Kapa Biosystems-Roche, Basel, Switzerland), following the instructions of the manufacturer. The fragment size distribution of the libraries was verified via micro-capillary gel electrophoresis on a LabChip GX system (PerkinElmer, Waltham, MA). The libraries were quantified by fluorometry on a Qubit instrument (LifeTechnologies, Carlsbad, CA) and pooled in equimolar ratios. The pool was quantified by qPCR with a Kapa Library Quant kit (Kapa Biosystems) and sequenced on an Illumina NovaSeq 6000 (Illumina, San Diego, CA) with paired-end 150-bp reads.

Paired-end sequencing reads were mapped to a composite human/SARS-CoV-2 genome using Subread Aligner v2.0.3 (69). A genome index was constructed using GRCh38 genome build with Gencode v38 annotation of the transcriptome, and Genbank MT246667.1 for the sequence of SARS-CoV-2, USA/WA-1/2020 isolate. Reads mapping to annotated genes were

counted using Subread featurecount v2.0.3 (70). Downstream analyses were performed with R. Differential gene expression analysis was done with DEseq2, which was also used to generate normalized gene counts (71). Low-expressed genes with less than three counts in at least three out of 16 samples were excluded from downstream analysis. q-Values were calculated using the q-value R package v2.24.0. For DEseq2 analysis, we used a one-factor design with four groups (WT mock, KO mock, WT infected and KO infected) and then likelihood ratio testing (LRT) to find all genes that were differentially expressed between at least two groups (q-value threshold <0.01), and with a basemean expression >15. Consensus clustering of the 3221 differentially expressed genes was performed with the degPatterns function of R DEGreport package v1.28.0, using default parameters and rlog-transformed counts. This generated eight clusters. Over-representation of biological gene sets in the gene clusters was investigated using the R clusterProfiler package and enricher function (72). Gene sets were downloaded from the MSIG data bank via the msigdbr R-project package, including “Hallmark,” and “Reactome”. (73). Gene sets were considered significantly enriched in a cluster if q values were < 0.05. For analysis of restriction factors in figure 6, we first selected genes in clusters 1 to 8 that belonged to the hallmark curated data set “Interferon Alpha response”. We complemented this list with additional genes from clusters 7 and 8 that belonged to the “Interferon Gamma response”, “Inflammatory response” and “TNFa signaling via NfKB" hallmark datasets, and finally added genes that we manually identified as potential restriction factors from literature searches. Average log2 fold-change compared to mock-infected WT was calculated and plotted, as well as the q-value between mock-infected WT and KO. Code developed for this study is available at https://github.com/mariuswalter/SIRT5_paper. This analysis relied heavily on code made

available by the laboratory of Denis Goldfarb (https://github.com/GoldfarbLab/H522_paper_figures), and described in ref (45).

Data and code availability

The data supporting the findings of this study are available within the paper and its Supplementary files. RNA-seq data have been deposited to the GEO repository (GSE188382). Code developed for RNA-seq analysis is available on Github (github.com/mariuswalter/SIRT5_paper). Mass spectrometric raw data have been deposited to the MassIVE repository (MSV000088589) and are also available at ProteomeXchange (PXD030530). Plasmids, viruses and other reagents developed in this study are available upon request and subject to standard material transfer agreements with the Buck Institute. Any other relevant data are available upon reasonable request.

Acknowledgments

We thank the QCRG Virology group at UCSF for technical and conceptual help, as well as members of the Verdin and Ott lab, in particular Rebeccah Riley, Rosalba Perrone and Anthony Covarrubias. We thank Michelle Moritz at UCSF for attempting co-purification experiments in *E. coli*. We thank David Gordon for quickly sharing the plasmid library early in the study and Max Greenberg at Paris University for sharing the Transposase plasmid.
This study was funded through institutional support from the Buck Institute for Research on Aging. IPC received support from the NIH (F31 AI164671-01). M.O. gratefully acknowledges support through gifts by Pamela and Edward Taft, and the Roddenberry Foundation. We acknowledge the support of instrumentation from the NCRR shared instrumentation grant 1S10 OD016281 (Buck Institute) for Mass Spectrometry Analysis, and the NIH Shared Instrumentation Grant 1S10OD010786-01 (UC Davis) for RNA-sequencing.

Supplemental Figures

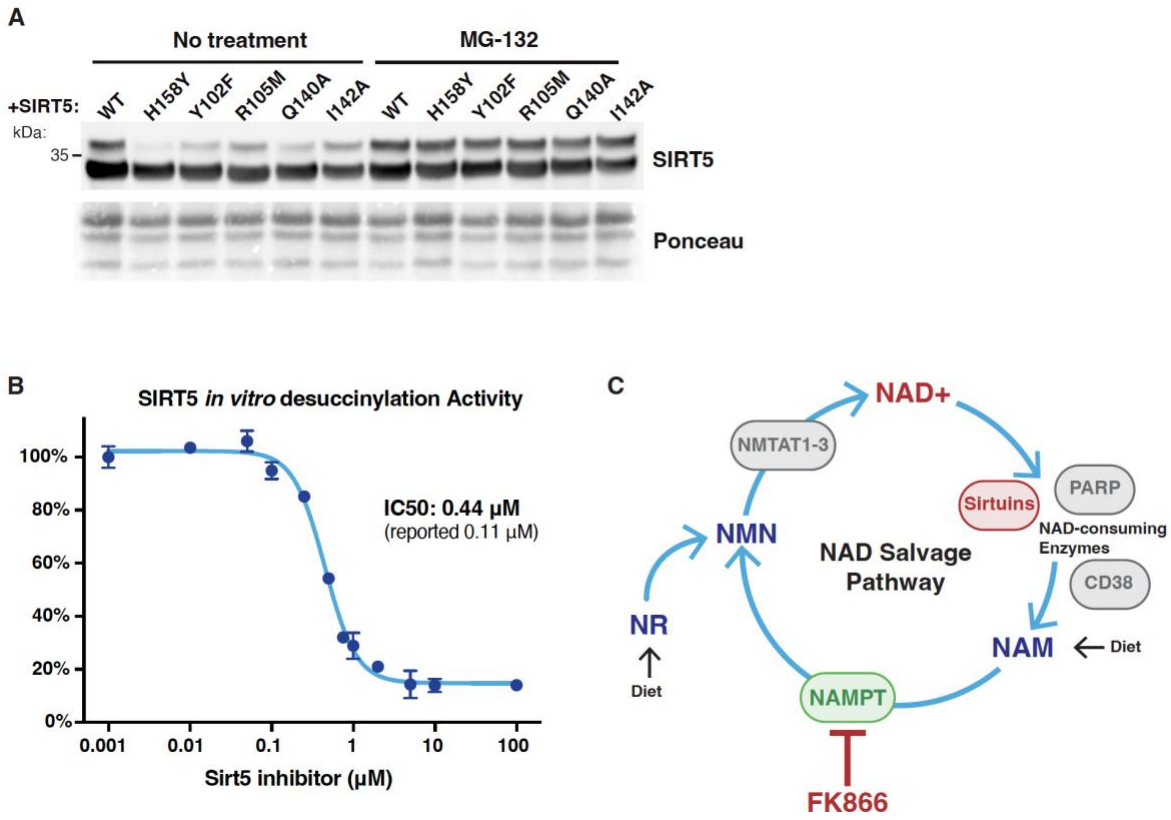

Supplementary Figure S2.1: Characterization of inhibitors.
A. Western Blot after transfection of HEK-293T cells with SIRT5 WT and catalytic mutants, with or without treatment for 6h with the proteasome inhibitor MG-132. No major defect in protein folding could be detected. B. SIRT5 in vitro desuccinylation activity in the presence of Sirt5-i inhibitor. n=3. C. Diagram of the NAD salvage pathway. Inhibition of NAMPT by FK866 inhibitor depletes cellular NMN and NAD levels. Supplementation by exogenous NMN rescues NAD.

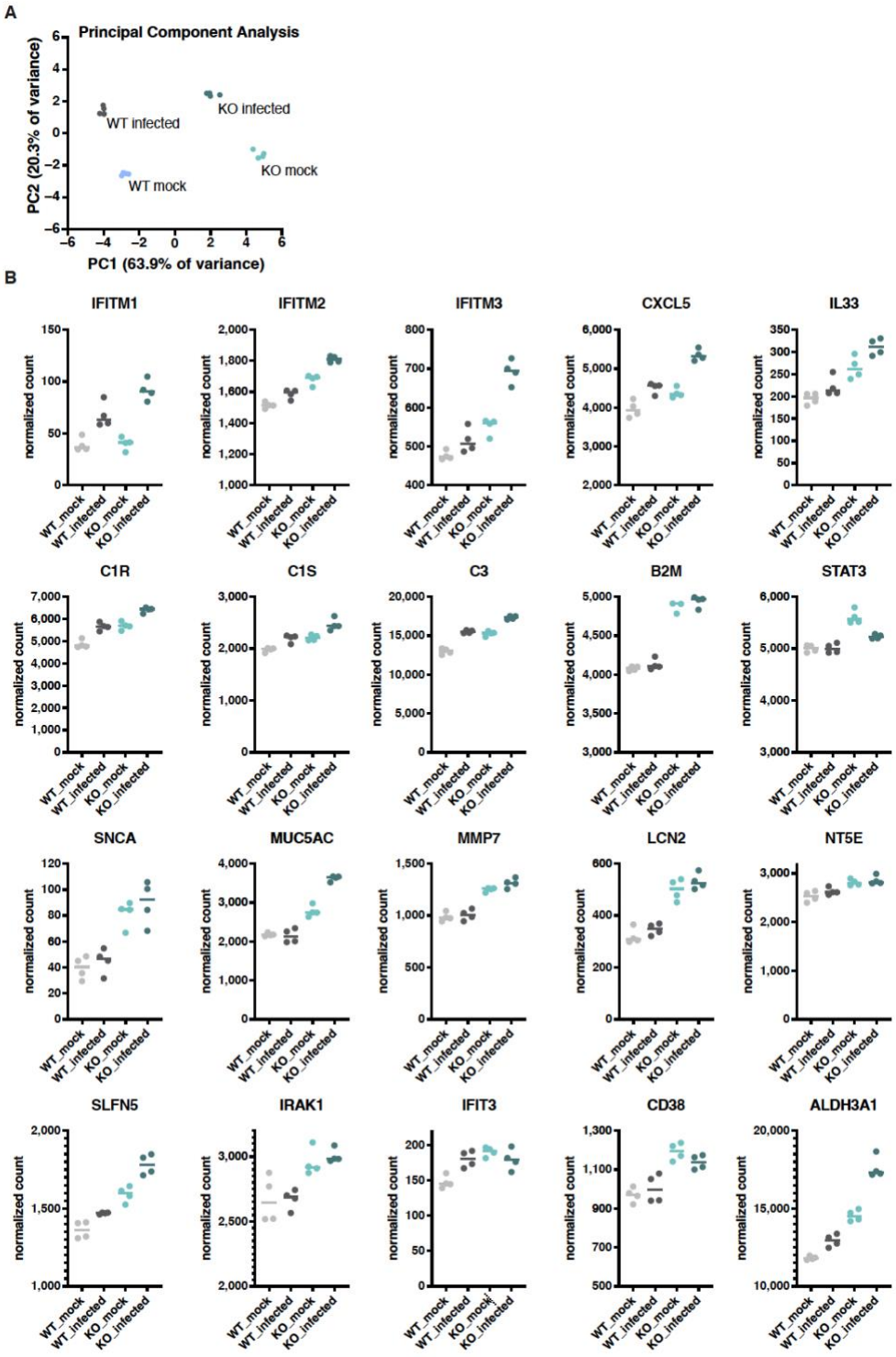

Supplementary Figure S2.2: Levels of viral restriction factors

A. Principal component analysis of RNA-seq samples, showing that replicates are well separated based on knockout and infection status. B. Normalized gene count of interferon-stimulated genes and restriction factors, from **Figure 2.7**.

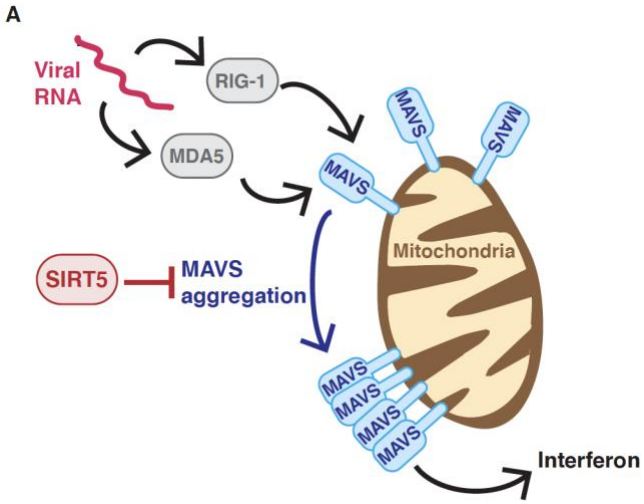

Supplementary Figure S2.3: Role of SIRT5 in the RIG-1/MAVS antiviral signaling pathway.
A. Recognition of cytosolic viral RNA by RIG-1 or MDA5 leads to MAVS aggregation on the mitochondrial surface, which in turn causes type I interferon production. SIRT5 desuccinylation of MAVS impairs MAVS aggregation and reduces interferon production. Adapted from Liu et al. (30).

Author contributions

MW and EV designed the study and analyzed the data. MW, IJK, OB, AC performed molecular biology experiments. IPC, AVG, and JMH performed SARS-CoV-2 assays and analyses. VL and JDG provided purified Nsp14 proteins. SS and BS performed mass spectrometry experiments and analysis. MW analyzed RNA-seq data. EV and OT supervised and funded the project. M.W. and E.V. wrote the manuscript with input from all authors.

References

1. D. E. Gordon, *et al.*, A SARS-CoV-2 protein interaction map reveals targets for drug repurposing. *Nature* **583**, 459–468 (2020).
2. D. E. Gordon, *et al.*, Comparative host-coronavirus protein interaction networks reveal pan-viral disease mechanisms. *Science* **370** (2020).
3. J. Li, *et al.*, Virus-Host Interactome and Proteomic Survey Reveal Potential Virulence Factors Influencing SARS-CoV-2 Pathogenesis. *Med (N Y)* **2**, 99-112.e7 (2021).
4. E. M. N. Laurent, Y. Sofianatos, A. Komarova, J. P. Gimeno, Global BioID-based SARS-CoV-2 proteins proximal interactome unveils novel ties between viral polypeptides and host factors involved in multiple COVID19 …. *BioRxiv* (2020).
5. E. Minskaia, *et al.*, Discovery of an RNA virus 3'->5' exoribonuclease that is critically involved in coronavirus RNA synthesis. *Proc. Natl. Acad. Sci. U. S. A.* **103**, 5108–5113 (2006).
6. Y. Chen, *et al.*, Functional screen reveals SARS coronavirus nonstructural protein nsp14 as a novel cap N7 methyltransferase. *Proc. Natl. Acad. Sci. U. S. A.* **106**, 3484–3489 (2009).
7. Y. Ma, *et al.*, Structural basis and functional analysis of the SARS coronavirus nsp14-nsp10 complex. *Proc. Natl. Acad. Sci. U. S. A.* **112**, 9436–9441 (2015).
8. L. Yan, *et al.*, Coupling of N7-methyltransferase and 3'-5' exoribonuclease with SARS-CoV-2 polymerase reveals mechanisms for capping and proofreading. *Cell* **184**, 3474-3485.e11 (2021).
9. F. Ferron, *et al.*, Structural and molecular basis of mismatch correction and ribavirin excision from coronavirus RNA. *Proc. Natl. Acad. Sci. U. S. A.* **115**, E162–E171 (2018).
10. M. Bouvet, *et al.*, RNA 3'-end mismatch excision by the severe acute respiratory syndrome

coronavirus nonstructural protein nsp10/nsp14 exoribonuclease complex. *Proc. Natl. Acad. Sci. U. S. A.* **109**, 9372–9377 (2012).

11. C. Liu, *et al.*, Structural basis of mismatch recognition by a SARS-CoV-2 proofreading enzyme. *Science* (2021) https:/doi.org/10.1126/science.abi9310 (July 28, 2021).
12. L. D. Eckerle, X. Lu, S. M. Sperry, L. Choi, M. R. Denison, High fidelity of murine hepatitis virus replication is decreased in nsp14 exoribonuclease mutants. *J. Virol.* **81**, 12135–12144 (2007).
13. L. D. Eckerle, *et al.*, Infidelity of SARS-CoV Nsp14-exonuclease mutant virus replication is revealed by complete genome sequencing. *PLoS Pathog.* **6**, e1000896 (2010).
14. A. E. Gorbalenya, L. Enjuanes, J. Ziebuhr, E. J. Snijder, Nidovirales: evolving the largest RNA virus genome. *Virus Res.* **117**, 17–37 (2006).
15. C. Lauber, *et al.*, The footprint of genome architecture in the largest genome expansion in RNA viruses. *PLoS Pathog.* **9**, e1003500 (2013).
16. N. S. Ogando, *et al.*, The Enzymatic Activity of the nsp14 Exoribonuclease Is Critical for Replication of MERS-CoV and SARS-CoV-2. *J. Virol.* **94** (2020).
17. J. C.-C. Hsu, M. Laurent-Rolle, J. B. Pawlak, C. B. Wilen, P. Cresswell, Translational shutdown and evasion of the innate immune response by SARS-CoV-2 NSP14 protein. *Proc. Natl. Acad. Sci. U. S. A.* **118** (2021).
18. M. Hayn, *et al.*, Systematic functional analysis of SARS-CoV-2 proteins uncovers viral innate immune antagonists and remaining vulnerabilities. *Cell Rep.* **35**, 109126 (2021).
19. T. Li, *et al.*, SARS-CoV-2 Nsp14 activates NF-κB signaling and induces IL-8 upregulation. *bioRxiv* (2021) https:/doi.org/10.1101/2021.05.26.445787.
20. J. Gribble, *et al.*, The coronavirus proofreading exoribonuclease mediates extensive viral

recombination. *PLoS Pathog.* **17**, e1009226 (2021).

21. R. H. Houtkooper, E. Pirinen, J. Auwerx, Sirtuins as regulators of metabolism and healthspan. *Nat. Rev. Mol. Cell Biol.* **13**, 225–238 (2012).
22. S.-I. Imai, L. Guarente, It takes two to tango: NAD+ and sirtuins in aging/longevity control. *NPJ Aging Mech Dis* **2**, 16017 (2016).
23. J. Du, *et al.*, Sirt5 is a NAD-dependent protein lysine demalonylase and desuccinylase. *Science* **334**, 806–809 (2011).
24. M. Tan, *et al.*, Lysine glutarylation is a protein posttranslational modification regulated by SIRT5. *Cell Metab.* **19**, 605–617 (2014).
25. M. J. Rardin, *et al.*, SIRT5 regulates the mitochondrial lysine succinylome and metabolic networks. *Cell Metab.* **18**, 920–933 (2013).
26. Y. Nishida, *et al.*, SIRT5 Regulates both Cytosolic and Mitochondrial Protein Malonylation with Glycolysis as a Major Target. *Mol. Cell* **59**, 321–332 (2015).
27. S. Kumar, D. B. Lombard, Functions of the sirtuin deacylase SIRT5 in normal physiology and pathobiology. *Crit. Rev. Biochem. Mol. Biol.* **53**, 311–334 (2018).
28. J. Yu, *et al.*, Metabolic characterization of a Sirt5 deficient mouse model. *Sci. Rep.* **3**, 2806 (2013).
29. N. C. Yeo, *et al.*, An enhanced CRISPR repressor for targeted mammalian gene regulation. *Nat. Methods* **15**, 611–616 (2018).
30. X. Liu, *et al.*, SIRT5 impairs aggregation and activation of the signaling adaptor MAVS through catalyzing lysine desuccinylation. *EMBO J.* **39**, e103285 (2020).
31. X. Yang, *et al.*, SHMT2 Desuccinylation by SIRT5 Drives Cancer Cell Proliferation. *Cancer Res.* **78**, 372–386 (2018).

32. Y. Xiangyun, *et al.*, Desuccinylation of pyruvate kinase M2 by SIRT5 contributes to antioxidant response and tumor growth. *Oncotarget* **8**, 6984–6993 (2017).

33. A. M. Davenport, F. M. Huber, A. Hoelz, Structural and functional analysis of human SIRT1. *J. Mol. Biol.* **426**, 526–541 (2014).

34. N. Rajabi, *et al.*, Mechanism-Based Inhibitors of the Human Sirtuin 5 Deacylase: Structure-Activity Relationship, Biostructural, and Kinetic Insight. *Angew. Chem. Int. Ed Engl.* **56**, 14836–14841 (2017).

35. E. Verdin, NAD^+ in aging, metabolism, and neurodegeneration. *Science* **350**, 1208–1213 (2015).

36. A. J. Covarrubias, *et al.*, Senescent cells promote tissue NAD+ decline during ageing via the activation of CD38+ macrophages. *Nat Metab* **2**, 1265–1283 (2020).

37. M. Bouhaddou, *et al.*, The Global Phosphorylation Landscape of SARS-CoV-2 Infection. *Cell* **182**, 685-712.e19 (2020).

38. L. Polletta, *et al.*, SIRT5 regulation of ammonia-induced autophagy and mitophagy. *Autophagy* **11**, 253–270 (2015).

39. Y.-Q. Wang, *et al.*, Sirtuin5 contributes to colorectal carcinogenesis by enhancing glutaminolysis in a deglutarylation-dependent manner. *Nat. Commun.* **9**, 545 (2018).

40. Y. L. N. Abril, *et al.*, Pharmacological and genetic perturbation establish SIRT5 as a promising target in breast cancer. *Oncogene* **40**, 1644–1658 (2021).

41. L. Chang, *et al.*, SIRT5 promotes cell proliferation and invasion in hepatocellular carcinoma by targeting E2F1. *Mol. Med. Rep.* **17**, 342–349 (2018).

42. D. Blanco-Melo, *et al.*, Imbalanced Host Response to SARS-CoV-2 Drives Development of COVID-19. *Cell* **181**, 1036-1045.e9 (2020).

43. T. Yamada, *et al.*, RIG-I triggers a signaling-abortive anti-SARS-CoV-2 defense in human lung cells. *Nat. Immunol.* **22**, 820–828 (2021).

44. Y. Kasuga, B. Zhu, K.-J. Jang, J.-S. Yoo, Innate immune sensing of coronavirus and viral evasion strategies. *Exp. Mol. Med.* **53**, 723–736 (2021).

45. M. Puray-Chavez, *et al.*, Systematic analysis of SARS-CoV-2 infection of an ACE2-negative human airway cell. *Cell Rep.* **36**, 109364 (2021).

46. C. Sanders, P. Thomas, MMP-7 promotes host recovery and lung function to influenza virus infection (VIR2P.1016). *The Journal of Immunology* **192**, 75.5-75.5 (2014).

47. T. H. Flo, *et al.*, Lipocalin 2 mediates an innate immune response to bacterial infection by sequestrating iron. *Nature* **432**, 917–921 (2004).

48. C. Ehre, *et al.*, Overexpressing mouse model demonstrates the protective role of Muc5ac in the lungs. *Proc. Natl. Acad. Sci. U. S. A.* **109**, 16528–16533 (2012).

49. A. D. Arslan, *et al.*, Human SLFN5 is a transcriptional co-repressor of STAT1-mediated interferon responses and promotes the malignant phenotype in glioblastoma. *Oncogene* **36**, 6006–6019 (2017).

50. J. Niemelä, *et al.*, IFN-alpha induced adenosine production on the endothelium: a mechanism mediated by CD73 (ecto-5'-nucleotidase) up-regulation. *J. Immunol.* **172**, 1646–1653 (2004).

51. F. Blanc, *et al.*, Targeting host calpain proteases decreases influenza A virus infection. *Am. J. Physiol. Lung Cell. Mol. Physiol.* **310**, L689-99 (2016).

52. A. R. Massey, J. D. Beckham, Alpha-Synuclein, a Novel Viral Restriction Factor Hiding in Plain Sight. *DNA Cell Biol.* **35**, 643–645 (2016).

53. H.-S. Kwon, *et al.*, Human immunodeficiency virus type 1 Tat protein inhibits the SIRT1

deacetylase and induces T cell hyperactivation. *Cell Host Microbe* **3**, 158–167 (2008).

54. S. Pagans, *et al.*, SIRT1 regulates HIV transcription via Tat deacetylation. *PLoS Biol.* **3**, e41 (2005).
55. T. Heinonen, *et al.*, Sirtuin 5 Deficiency Does Not Compromise Innate Immune Responses to Bacterial Infections. *Front. Immunol.* **9**, 2675 (2018).
56. E. Koyuncu, *et al.*, Sirtuins are evolutionarily conserved viral restriction factors. *MBio* **5** (2014).
57. F. Hou, *et al.*, MAVS forms functional prion-like aggregates to activate and propagate antiviral innate immune response. *Cell* **146**, 448–461 (2011).
58. Y.-Z. Fu, *et al.*, SARS-CoV-2 membrane glycoprotein M antagonizes the MAVS-mediated innate antiviral response. *Cell. Mol. Immunol.* **18**, 613–620 (2021).
59. C.-S. Shi, *et al.*, SARS-coronavirus open reading frame-9b suppresses innate immunity by targeting mitochondria and the MAVS/TRAF3/TRAF6 signalosome. *J. Immunol.* **193**, 3080–3089 (2014).
60. E. C. Freundt, L. Yu, E. Park, M. J. Lenardo, X.-N. Xu, Molecular determinants for subcellular localization of the severe acute respiratory syndrome coronavirus open reading frame 3b protein. *J. Virol.* **83**, 6631–6640 (2009).
61. Y. Chen, Z. Zhou, W. Min, Mitochondria, Oxidative Stress and Innate Immunity. *Front. Physiol.* **9**, 1487 (2018).
62. T. Weichhart, M. Hengstschläger, M. Linke, Regulation of innate immune cell function by mTOR. *Nat. Rev. Immunol.* **15**, 599–614 (2015).
63. J. Guan, *et al.*, Sirtuin 5 regulates the proliferation, invasion and migration of prostate cancer cells through acetyl-CoA acetyltransferase 1. *J. Cell. Mol. Med.* **24**, 14039–14049

(2020).

64. A. Vallejo-Gracia, *et al.*, FOXO1 promotes HIV latency by suppressing ER stress in T cells. *Nat Microbiol* **5**, 1144–1157 (2020).
65. M. A. Horlbeck, *et al.*, Compact and highly active next-generation libraries for CRISPR-mediated gene repression and activation. *Elife* **5**, e19760 (2016).
66. T. Tezil, *et al.*, Lifespan-increasing drug nordihydroguaiaretic acid inhibits p300 and activates autophagy. *NPJ Aging Mech Dis* **5**, 7 (2019).
67. D. G. Christensen, *et al.*, Identification of Novel Protein Lysine Acetyltransferases in Escherichia coli. *MBio* **9** (2018).
68. M. Walter, E. Verdin, Viral gene drive in herpesviruses. *Nat. Commun.* **11**, 4884 (2020).
69. Y. Liao, G. K. Smyth, W. Shi, The Subread aligner: fast, accurate and scalable read mapping by seed-and-vote. *Nucleic Acids Res.* **41**, e108 (2013).
70. Y. Liao, G. K. Smyth, W. Shi, featureCounts: an efficient general purpose program for assigning sequence reads to genomic features. *Bioinformatics* **30**, 923–930 (2014).
71. M. I. Love, W. Huber, S. Anders, Moderated estimation of fold change and dispersion for RNA-seq data with DESeq2. *Genome Biol.* **15**, 550 (2014).
72. G. Yu, L. G. Wang, Y. Han, Q. Y. He, clusterProfiler: an R package for comparing biological themes among gene clusters. *OMICS* (2012).
73. A. Liberzon, *et al.*, Molecular signatures database (MSigDB) 3.0. *Bioinformatics* **27**, 1739–1740 (2011).

Chapter 3

Molecular mechanisms of primate lentiviral Vif adaptation that enable cross species transmission and the birth of HIV-1

Victor L. Lam[1], Nicholas M. Chesarino[2], Michael Emerman[2], John D. Gross[1,3,4]

Affiliations:

[1] University of California San Francisco, San Francisco, CA, United States.

[2] Divisions of Human Biology and Basic Sciences, Fred Hutchinson Cancer Center, Seattle, WA, USA.

[3] Department of Pharmaceutical Chemistry, University of California San Francisco, San Francisco, CA, United States.

[4] Quantitative Biosciences Institute (QBI), University of California San Francisco, San Francisco, CA, United States.

Abstract

Host innate immune systems pose a barrier to the cross-species transmission of zoonotic viruses. Viruses overcome these barriers by encoding suppressors of the innate immune response, and this suppression can enable adaption to new hosts as part of the host-virus arms race. One paradigm of this interaction is the SIV/HIV Vif and APOBEC3 interaction. Vif binds to APOBEC3G (A3G), an antiviral host protein, along with host ubiquitin ligase complexes. This ubiquitination marks A3G for degradation and allows the virus to replicate successfully. While millions of years of diversifying selection allow for A3G to escape Vif antagonism, adaptations in Vif can reestablish the interaction and allow for antagonism of A3Gs of new hosts.

Due to diversifying selection, A3G is a potent barrier to cross-species transmission of primate lentiviruses. SIV that infects red-capped mangabey SIV (SIVrcm), the precursor to chimpanzee SIV and HIV-1, is unable to cross the species barrier without further adaptation in Vif. Previous work from our labs identified a single amino acid mutation in Vif from SIVrcm that allows for the virus to replicate in cells expressing A3G from chimpanzees and overcome the species barrier. We recently determined the structure of HIV-1 Vif bound to human A3G which can be used as a guide for further functional studies[1]. However, it is unclear whether the adaptation in Vif affected its binding affinity for A3G in a new species or its ability to ubiquitinate a new A3G. Here we report quantitative in vitro ubiquitination assays and pulldowns on mammalian cell lysates to test this question. Our study addresses the possibility the viral adaptation to restriction factors play out through binding and positioning with respect to catalytic machinery for ubiquitin transfer. By investigating the mechanism behind this mutation in Vif, we link how the molecular effects of this mutation could allow for SIVrcm to cross the species barrier and eventually allow for the rise of HIV-1.

Introduction

HIV-1 is a lentivirus that first gained attention in the 1980s as being the causative agent of AIDS, and it has infected over 85 million people worldwide since its discovery[2]. HIV-1 emerged as a result of zoonotic transmission of Simian Immunodeficiency Virus from chimpanzees (SIVcpz)[3]. SIVcpz itself is a result of a recombination event between SIV from red-capped mangabey (SIVrcm), from which genes on the 5′ end of the genome like Vif originate, and SIV from guenons[4,5]. Due to the impact retroviruses can cause in both the short and long term, hosts express a wide variety of proteins to limit their proliferation and integration and viruses must adapt to and overcome these defenses.

APOBECs are a family of potent innate immune antiviral proteins that can cause C-to-U hypermutations due to their cytidine deaminase activity[6–9]. One member of this family, APOBEC3G (A3G), restricts retroviruses by binding to genomic RNA and getting packaged into the virion. At this stage, many cytidine bases in the viral genome are deaminated into uracil, and the accumulation of these mutations are detrimental to downstream processes such as integration and protein production once the virion is introduced into the next host cell. Lentiviruses like HIV and SIV integrate into the host genome as part of their life cycle, and remnants of ancient endogenized retroviruses can be found scattered across our genome[10].

As a result of A3G's antiviral activity, retroviruses tend to encode proteins to counteract this effect. Simian Immunodeficiency Viruses (SIV) and HIV encode a protein called Vif which can hijack different components of the host ubiquitin ligase E3 complex, including Cul5, Rbx2, Elongin B, and Elongin C, and other host proteins such as CBFβ to cause the polyubiquitination of A3G in host cells[11–15]. The initial priming ubiquitin on A3G is added by ARIH2 and UBE2L3 which then allows for subsequent polyubiquitination and chain formation to happen much faster

rate compared to reactions lacking ARIH2 and its priming activity[16]. This modification rids the infected cell of A3G via proteasomal degradation, and the resulting A3G-free virions can successfully replicate in the next host cell.

Like many host-viral interfaces, the interaction between A3G and Vif is under strong positive selection as part of an "arms race" between virus and host[17–19]. There is pressure for A3G to escape Vif antagonism through diversifying selection while evolution will select for variants of Vif that reestablish this antagonism. Due to A3G's potent antiviral activity, it serves as one of the barriers that an SIV must overcome when establishing infection in a new species. Many genetic studies, later confirmed by cryo-EM A3G-Vif structures, have identified residues 128 through 130 on A3G as being the residues that directly interact with Vif and determine species-specificity[1,7,20–25].

While the Vif-interacting arms race residues on A3G have been identified long ago, identifying the corresponding mutations that changed from rcmVif to cpzVif and HIV Vif has been elusive until recently. When SIVrcm jumped into a new chimpanzee host, there were numerous changes in Vif that convoluted the hunt for the mutation responsible for allowing A3G antagonism in a new host[26]. The most noticeable difference between rcmVif and cpzVif was the result of overprinting which caused the C-terminus of cpzVif to become truncated when compared to its predecessor. However, this new C-terminus on Vif was not responsible for its ability to counteract A3G in chimpanzees. Recreating just the overprinting and truncation event in rcmVif did not allow for it to counteract cpzA3G.

A separate mutation in the loop 5 region of rcmVif was later identified and tested for its ability to antagonize cpzA3G[27]. Changing a tyrosine at position 86 in rcmVif to a histidine allowed for rcmVif to now counteract chimpanzee and human A3Gs (**Fig. 3.1a**). While viruses

expressing wild type rcmVif had low infectivity after infecting cells expressing either chimpanzee or human A3G, viruses expressing the Y86H rcmVif had infectivity levels comparable to viruses expressing cpzVif or HIV Vif. This Y86H rcmVif was also able to prevent packaging of cpzA3G into virions. This mutation and loop 5 region of Vif was later shown to directly interact with the arms race 128-130 residues on A3G in the structure.

While we understood that this single point mutation allowed rcmVif to antagonize hominid A3Gs resulting in the exclusion of A3G from virions, we did not understand how this impacted Vif's ability to bind or polyubiquitinate A3G. We wanted to ask how a single point mutation in rcmVif allowed for it to remove hominid A3G from cells and establish infection in a new species. Here we explore how the Y86H mutation in rcmVif improves its ability to ubiquitinate human A3G (huA3G).

Results

Y86H rcmVif leads to the proteasomal degradation of huA3G

Previous work shows that Y86H rcmVif leads to the exclusion of hominid A3Gs from virions and improves viral infectivity over virions expressing wild type rcmVif[27]. While Vif is primarily known to act via the ubiquitination and proteasomal degradation pathway, there is a possibility that it neutralizes A3G using a ubiquitin-independent mechanism[28]. To confirm that this Y86H mutation in rcmVif acts using a ubiquitin-dependent proteasomal pathway to degrade A3G, we transfected different Vifs and huA3G in 293T cells and treated them with either a DMSO control or the proteasome inhibitor Mg132.

In the presence of HIV Hxb2 Vif, huA3G is degraded in the presence of DMSO, but bands for huA3G appear when the proteasome is blocked by Mg132 (**Fig. 3.1b, lanes 5-6**). This pattern is consistent with published literature and is indicative of Vif-mediated degradation via

the proteasome[13,29]. In contrast, with Y40/44A HIV Vif, a mutant that does not have any ability to ubiquitinate A3G, the change in huA3G levels between the DMSO and Mg132 groups is less striking (**Fig. 3.1b, lanes 7-8)**[30]. Y86H rcmVif appears similar to the HIV Hxb2 Vif in terms of degradation since huA3G is not present in the DMSO well but is restored in the presence of Mg132 (**Fig. 3.1b, lanes 3-4**). Meanwhile, the wild type rcmVif can cause huA3G degradation to some extent, but to a lesser degree than Y86H rcmVif or Hxb2 Vif (**Fig. 3.1b, lanes 1-2**). These results suggest that the Y86H rcmVif mutant is better than wild type rcmVif at causing the degradation of huA3G via the proteasome.

Interestingly, when we performed this experiment with rcmA3G, we saw that all three Vifs maintained the ability to degrade rcmA3G via the proteasome (**Fig. 3.1c, lanes 1-6**). This suggests that the Y86H mutation in rcmVif could broaden the spectrum of A3Gs that rcmVif can antagonize rather than as a toggle that completely switches species specificity. This result is consistent with the observation that Y86H rcmVif has comparable effects in rescuing viral infectivity in presence of rcmA3G or human A3G[27]. After seeing how different Vifs affect A3G degradation via the proteasome, we explored whether the Y86H mutation in rcmVif affects its ability to bind to A3G of a new species and whether the Y86H mutation affects rcmVif's ability to polyubiquitinate A3G.

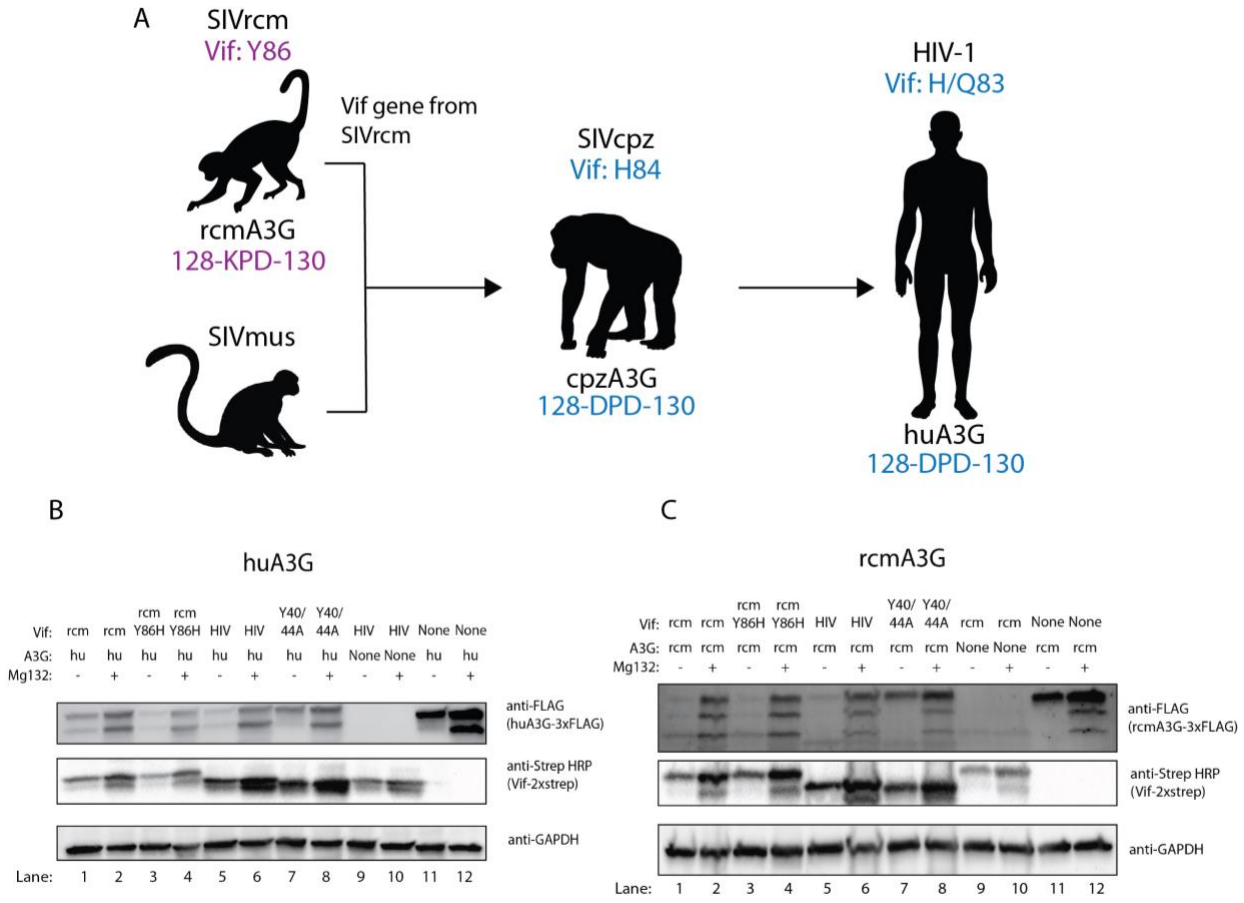

Figure 3.1: Y86H rcmVif mutation antagonizes both rcm and huA3G.
a, Diagram showing evolutionary history of HIV-1 and the adaptations in various SIV Vifs required to adapt to residues 128 and 130 in different host A3Gs. Changing Y86 to a histidine in rcmVif allows it to now counteract hominid A3G. Position 86 in rcmVif is equivalent to position 83 or 84 in cpz and HIV-1 Vif. b, Western blot showing degradation and rescue of FLAG-tagged huA3G in the presence of various Vifs. If a Vif is able to cause huA3G proteasomal degradation, the blot will show lower levels of A3G without Mg132 and these levels are rescued when Mg132 is added. The middle blot shows expression of transfected strep-tagged Vif while the bottom blot shows the GAPDH loading control. c, Western blot showing degradation and rescue of FLAG-tagged rcmA3G with different Vifs.

Y86H rcmVif and wild type rcmVif do not bind well to huA3G in coIPs

To examine the binding affinity between the various Vifs and rcmA3G and huA3G, we performed coIPs on 293T lysates from transfected cells. By pulling down on the FLAG tag of A3G, we can determine qualitatively whether a Vif variant binds to it. We found that all Vifs (rcmVif, Y86H rcmVif, and HIV-1 Hxb2 Vif) pulled down with rcmA3G which suggests that all

three were able to bind rcmA3G (**Fig. 3.2a, lanes 1-4**). Interestingly, neither rcmVif nor Y86H rcmVif pulled down with huA3G (**Fig. 3.2b, lanes 1-2**). Meanwhile Hxb2 Vif and the non-ubiquitinating mutant Y40/44A Vif both appeared in the pull down (**Fig. 3.2b, lanes 3-4**). This suggests that Y86H rcmVif's ability to cause huA3G degradation might not be a result of a binding affinity increase. Alternatively, changes in binding affinity may not be observed by coIP due to sensitivity to buffer conditions employed (see below). Furthermore, the Y86H mutation could modestly improve binding affinity to huA3G that leads to larger downstream effects when it comes to ubiquitination, but measuring this activity would require a more sensitive and quantitative assay.

Recent HIV Vif and huA3G structures have shown the presence of RNA in the interface between these proteins, so we tested whether adding RNase A and RNase T1 during the IP incubation step could disrupt the interaction. Removing RNA in rcmA3G samples appeared to somewhat disrupt wild type rcmVif and Y86H rcmVif binding to rcmA3G because less Vif is seen in pulldowns that have been RNase-treated compared to those that have not (**Fig. 3.2c, lanes 1-4**). Hxb2 Vif binding to rcmA3G appeared to be unaffected as similar amounts of Hxb2 Vif were pulled down in RNase-treated and untreated samples (**Fig. 3.2c, lanes 5-6**). When the pull downs were performed with huA3G, Hxb2 Vif pulled down at similar levels with huA3G regardless of whether the sample was RNase-treated (**Fig. 3.2d, lanes 5-6**).

Another unexpected result was that the Y40/44A Vif which was unable to lead to the degradation rcmA3G or huA3G in the whole cell lysate assay bound to and pulled down with both rcmA3G and huA3G (**Fig. 3.2c, lanes 7-8; Fig. 3.2d, lanes 7-8**). Furthermore, adding RNase seemed to disrupt this interaction.

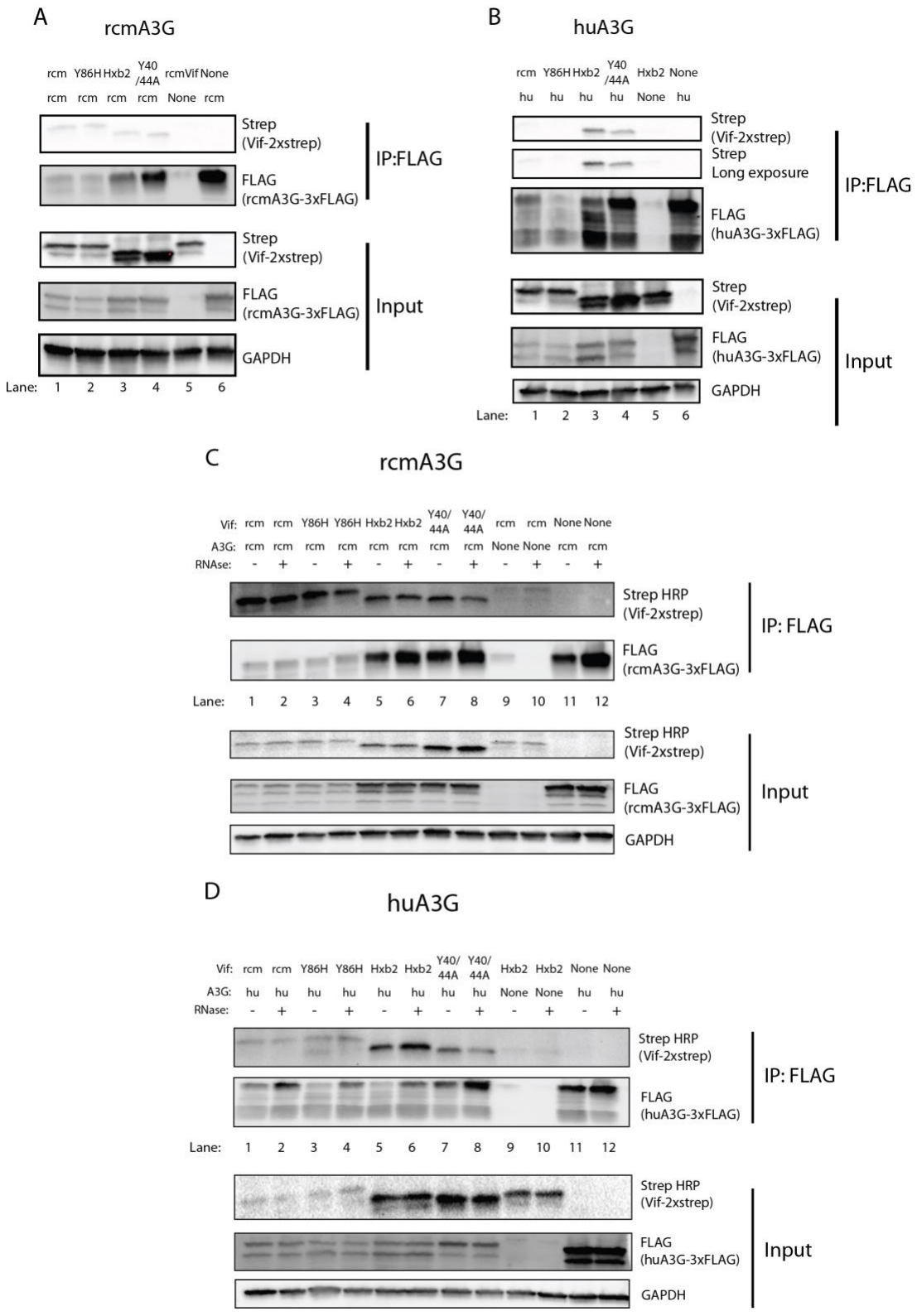

Figure 3.2: Pulldown of FLAG-tagged A3Gs to examine Vif binding.
a, Pulling down on the FLAG tag of rcmA3G shows that all Vifs are able to form a complex with rcmA3G. (Figure caption continued on the next page.)

(Figure caption continued from the previous page.) b, Pulling down on the FLAG tag of huA3G shows that only Hxb2 Vif and Y40/44A bind strongly to huA3G. Both wild type rcmVif and Y86H rcmVif are not seen in the pulldown, suggesting that the mutation does not increase Vif's binding affinity to huA3G. c, Addition of RNase to rcmA3G coIPs for 4 hours causes less wild type rcmVif and Y86H rcmVif to pull down with rcmA3G while Hxb2 pulldown is unaffected by RNase treatment. d, Addition of RNase to huA3G coIPs does not affect Hxb2 but reduces the amount of Y40/44A that is pulled down. Due to lane limitations on the gel, input samples for c and d were run on separate gels and blots than the IP samples.

Y86H mutation enhances rcmVif's ability to polyubiquitinate huA3G

Since Y86H rcmVif and Hxb2 Vif are able to send huA3G for proteasomal degradation more effectively than wild type rcmVif, we next asked whether the Y86H mutation improves Vif's ability to ubiquitinate huA3G in cells. Y86H rcmVif did not bind to huA3G any better than rcmVif, so it is possible that the mutation affects Vif's interaction with the ability to promote that catalytic step of ubiquitination of A3G instead of binding. We transfected cells with various Vifs as before but also included a myc-ubiquitin expression vector to easily look for ubiquitin chain formation using Western blot. Additionally, we isolated huA3G by immunoprecipitation (IP) to only look at huA3G and ubiquitin chains formed on it. We find that rcmVif is unable to polyubiquitinate huA3G to a great extent and was comparable to the non-degrading, non-ubiquitinating Y40/44A Vif mutant (**Fig. 3.3a, lanes 7, 10)**. While huA3G had some polyubiquitination in the presence of rcmVif and Y40/44A Vif, this is likely due to basal levels of non-Vif mediated ubiquitination seen in other published IPs as well[31,32]. In comparison, we see robust polyubiquitination of huA3G in the presence of Hxb2 Vif, and Y86H rcmVif is more capable of polyubiquitinating huA3G compared to rcmVif (**Fig. 3.3a, lanes 8-9)**.

Performing the same experiments with rcmA3G yielded somewhat confusing results. Although we could IP and see unmodified huA3G without the need for Mg132 due to high steady state levels of huA3G in transfected cells even in the presence of Vif, most rcmA3G is ubiquitinated in the presence of Vif and appeared to express slightly better in cells with Hxb2 Vif

and Y40/44A Vif (**Fig. 3.3b**). This made it difficult to directly compare rcmA3G ubiquitination between the different Vifs since each lane contains a different amount of A3G. We tried to remedy this by using Mg132 sixteen hours prior to harvesting the samples, but we still saw different levels of unubiquitinated rcmA3G (**Fig. 3.3c**). Still, it is interesting to note that Hxb2 Vif was able to cause the polyubiquitination of rcmA3G with or without Mg132 which further supports the possibility that Hxb2 Vif maintains its ability to antagonize rcmA3G (**Fig. 3.3b, lane 9; Fig. 3.3c, lane 9**).

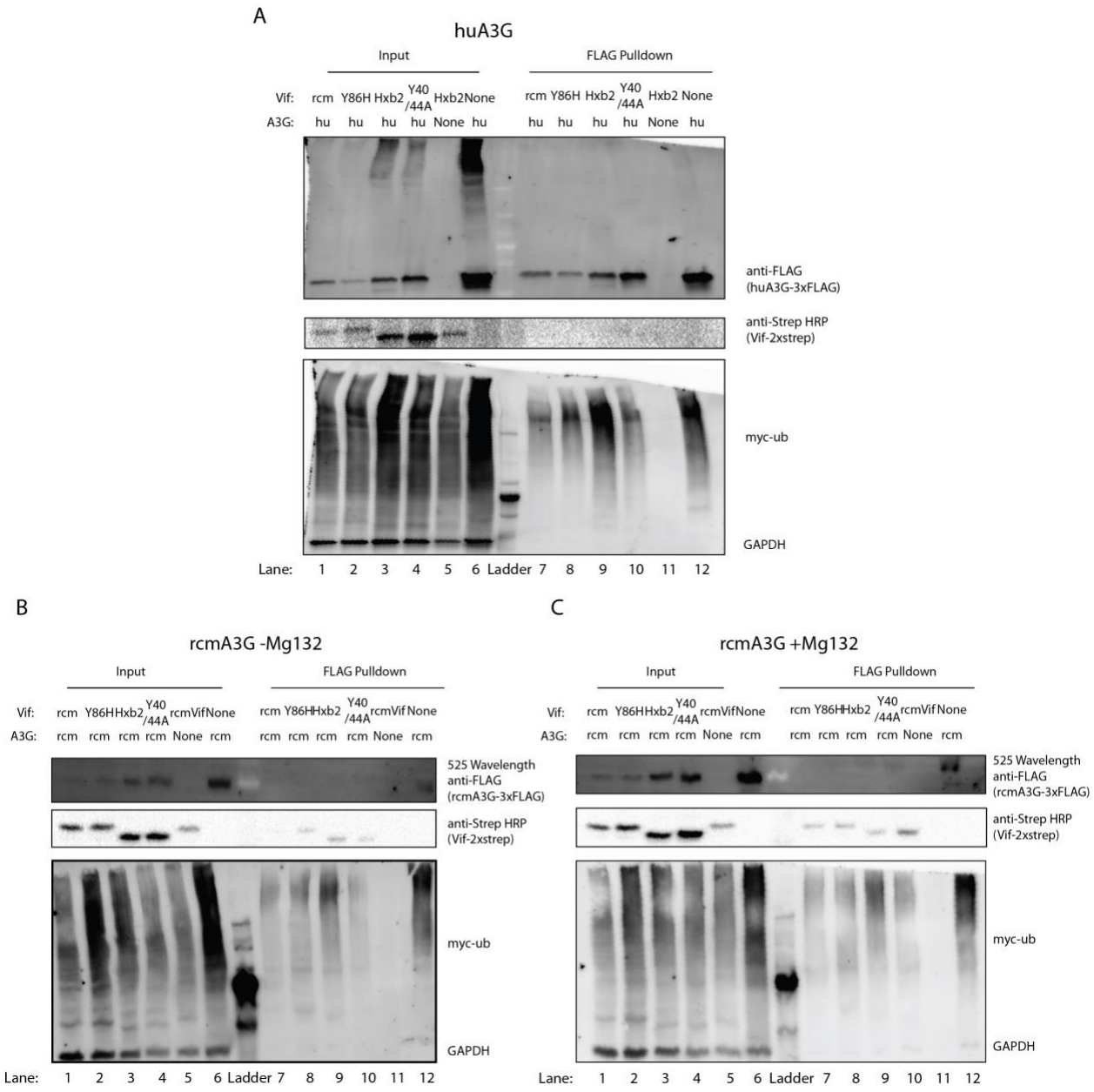

Figure 3.3: FLAG pulldown and Western blot of ubiquitinated A3G.
a, Western blot showing the ubiquitination of huA3G with different Vifs in 293T cells in the absence of Mg132. HuA3G-3xFLAG was pulled down using magnetic beads and eluted using 3x FLAG peptide. b, Western blot showing the ubiquitination of rcmA3G with different Vifs in 293T cells in the absence of Mg132. RcmA3G-3xFLAG was pulled down using magnetic beads and eluted using 3x FLAG peptide. c, FLAG pulldown and Western blot showing ubiquitination of rcmA3G-3xFLAG in the presence of different Vifs. Cells were treated with 5uM Mg132 16 hours prior to harvesting.

Y86H rcmVif also polyubiquitinates huA3G in vitro

To complement IP experiments done in tissue culture, we performed in vitro ubiquitination assays by combining components of the Cul5/Rbx2 ubiquitin pathway with huA3G and various Vifs similar to previously published work[16]. Polyubiquitin chains quickly formed on huA3G in the presence of HIV-1 Vif starting at 5 minutes (**Fig, 3.4a**). In contrast, there was little polyubiquitination of huA3G in the presence of rcmVif. Y86H rcmVif caused more polyubiquitination on huA3G compared to wild type rcmVif but less than HIV-1 Vif. Y86H rcmVif had a similar effect to what we saw in **Fig. 3.3a**. A caveat of these experiments is RNA was not completely removed from A3G during purification and addition of a specific RNA sequence may be required for efficient ubiquitination of A3G by Vif using recombinant purified proteins, as described in a recently report, showing specific RNA sequences are required for Vif to ubiquitinate a solubility optimized construct of A3G[25].

Since A3G ubiquitination is a two-step process involving both an initial priming step involving ARIH2 and UBE2L3 followed by chain elongation involving other E2s, we decided to test whether the Y86H mutation in rcmVif enhances ubiquitination at the initial priming step or the chain elongation step. We performed in vitro ubiquitination assays with ARIH2 and UBE2L3 and omitted UBE2R1, the chain elongating E2 we used in our experiments. Additionally, we replaced ubiquitin with chain-terminating methylated ubiquitin (meUb) so only monoubiquitination and multi-monoubiquitination was seen. With meUb, rcmVif could only place one or two monoubiquitins on huA3G, while HIV-1 Vif had approximately six or seven monoubiquitin sites (**Fig. 3.4b**). The Y86H rcmVif appeared to mostly have one or two monoubiquitins, but we saw additional higher molecular weight multi-monoubiquitinated huA3G

bands with Y86H rcmVif that were not seen with wild type rcmVif. Again, the Y86H rcmVif in this assay appeared to be a bit of an intermediate rcmVif and HIV-1 Vif.

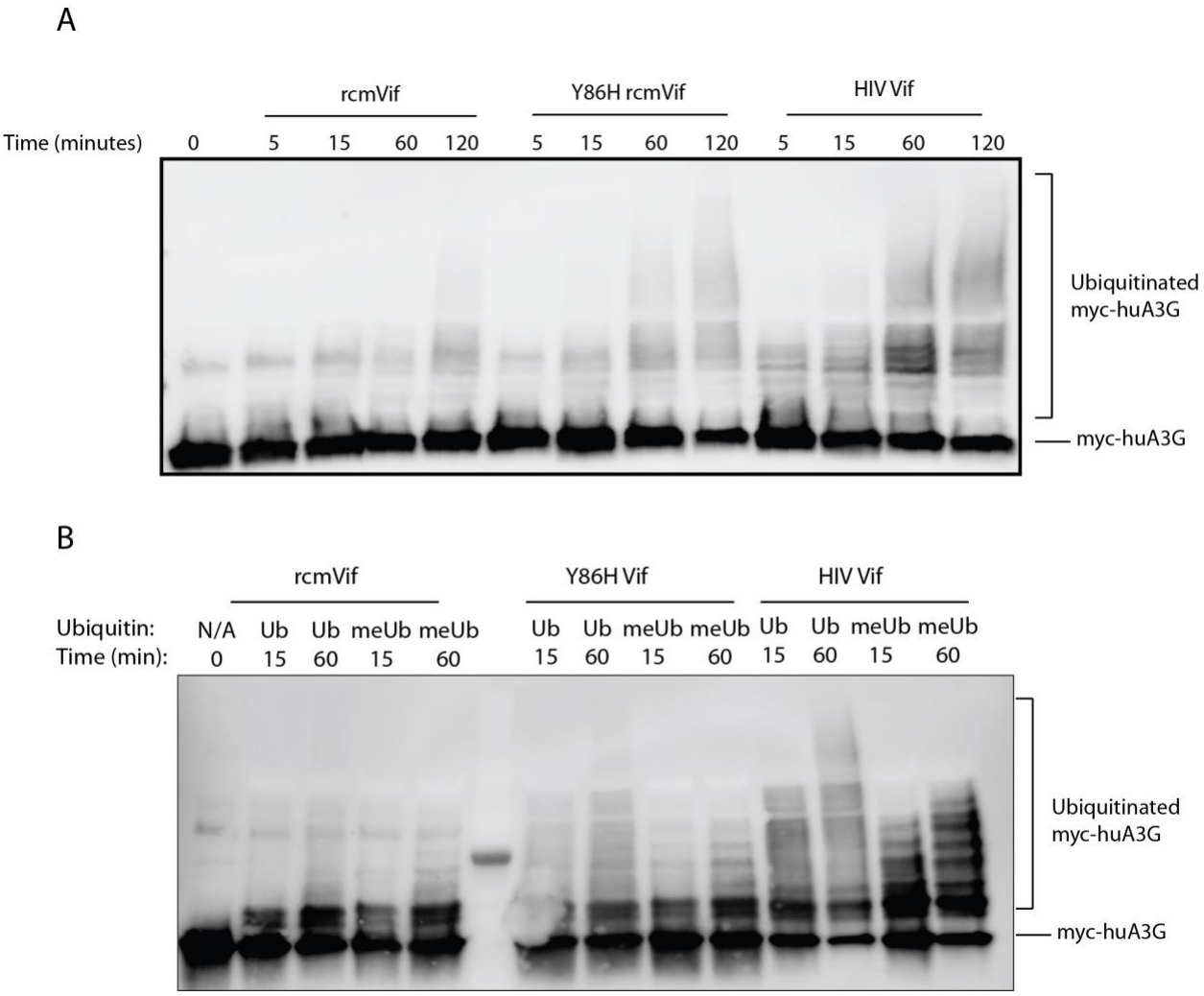

Figure 3.4: In vitro ubiquitination of huA3G with different Vifs.
a, Full in vitro ubiquitination assay of huA3G with UBE2R1, ARIH2, and UBE2L3. E1 and E2 components of the assay were charged with ubiquitin for 30 minutes and Vifs were combined with neddylated Cul5/Rbx2 prior to the addition of A3G substrate. Western blot was visualized using anti-myc antibody. b, In vitro ubiquitination assay with methylated ubiquitin (meUb) and UBE2L3 to examine effects of Y86H mutation on the initial priming and ARIH2-involved steps of huA3G ubiquitination.

Discussion

A tyrosine to histidine mutation at residue 86 in rcmVif allows for SIV to antagonize A3G defenses in both chimpanzees and humans and is a potential clue to what allowed for cross-species transmission and the origins of SIVcpz and HIV-1[27]. Even though recent structures confirmed the interaction of this residue with the arms race interface at positions 128-130 of A3G, it did not provide a clear explanation behind the function of the mutation[1,24,25]. We sought to identify the mechanism behind why such a small amino acid change is able to allow for successful antagonism of hominid A3Gs through tissue culture and in vitro ubiquitination assays.

By transfecting in different Vifs and A3Gs into 293T cells and blocking the proteasome with Mg132, we saw that Y86H rcmVif and HIV-1 Vif could cause the proteasomal degradation of huA3G to a much greater extent than rcmVif. Combined with previously published infectivity data, this confirms that Y86H rcmVif was able to exclude hominid A3Gs from virions because it was able to cause their degradation. Interestingly, both Y86H rcmVif and HIV-1 Vif maintained their ability to antagonize rcmA3G. This result was unexpected because prior studies showed that HIV-1 Vif could not antagonize A3G from African green monkeys [21]. Furthermore, R15 of HIV-1 Vif contacts D128 of huA3G, and the interaction of HIV-1 Vif with rcmA3G would be predicted to be disfavored because position 128 of rcmA3G is a lysine and would have an electrostatic repulsion[1,24,25]. However, we cannot rule out the possibility that the side chains repack at this arms race interface or a compensation for a weaker interaction due to overexpression. While degradation of rcmA3G looks about equivalent between wild type rcm, Y86H rcmVif, and HIV-1 Vifs on a Western blot, rcmVif could have a subtle advantage in rcmA3G degradation that is hard to quantify in this assay. A small amount of A3G getting packaged into a virion is sufficient to decrease infectivity 10-fold, so subtle changes in

degradation could be enough to cause much larger changes in infectivity due to A3G packaging. Performing packaging and infectivity assays with the different Vifs and rcmA3G could be more informative on how infectivity could be impacted.

The Y86H mutation did not appear to improve binding to huA3G over wild type rcmVif in our coIP assay using 293T lysates. While all four Vifs shown pulled down with rcmA3G, wild type rcm and Y86H rcmVif exhibited poor binding to huA3G compared to HIV-1 and Y40/44A Vif. It is unlikely that the Y86H mutation improves rcmVif's ability to bind huA3G under these assay conditions. The other interesting result from this experiment was Y40/44A pulling down with both rcmA3G and huA3G. Alanine mutations at these residues are commonly used as negative controls for A3G experiments because these Vifs do not lead to A3G degradation as we also saw in our Mg132 assays (**Fig. 3.1b**)[30]. The same study also found that the Y40A Vif binds A3G at low triton X-100 concentrations but loses the ability to bind A3G at 1% Triton X-100. Despite using buffer containing 1.1% Triton X-100 for our IPs, we found that Y40/44A binding to rcm and huA3G persists. It is unclear why our results differ. Nonetheless, it is possible for mutant Vifs that are unable to cause A3G to still bind to A3G. HIV Vif containing a K26R mutation was reported to have lost its ability to antagonize huA3G but still pulled down and bound to it[33]. Interestingly, residues 26, 40, and 44 on Vif are all involved in interactions with the RNA glue sandwiched between Vif and A3G[1]. It is possible that the Y40/44A mutation still binds to A3G but at an orientation that is unable to cause polyubiquitination or is unable to properly bind to the RNA glue required for A3G polyubiquitination. The recent structure shows that these residues on Vif interact with the RNA glue between Vif and A3G, and mutations to K26, another residue critical for Vif function, on HIV Vif disrupt its ability to antagonize A3G but not its ability to pull down with A3G[1,33]. It is possible that the mutation functionally disrupts this

interaction for ubiquitination purposes by affecting the orientation of different components in the complex, but we still see a nonfunctional binding interaction in pulldowns.

Since RNase A/T1 appear to affect wild type rcmVif, Y86H rcmVif, and Y40/44A Vif binding to rcmA3G alongside disrupting the Y40/44A Vif binding to huA3G while Hxb2 Vif is agnostic to RNase treatment, it is possible that high affinity binding between Hxb2 Vif and huA3G could be protecting the RNA glue at the interface from degradation. The sequence of the RNA held at the interface is also unknown, so another possibility is the RNA at the Hxb2 Vif and huA3G interface is resistant to RNase A/T1, which cleave after pyrimidines and guanosines, respectively, while the RNA bound by wild type rcmVif and Y86H rcmVif is susceptible.

Y86H rcmVif appeared to be a bit of an intermediate between wild type rcmVif and HIV-1 Vif in both the ubiquitinated A3G pulldowns and in vitro ubiquitination assays (**Fig. 3.3a, Fig. 3.4a**). Y86H rcmVif did not cause as much polyubiquitination compared to HIV-1, but it was noticeably stronger than wild type rcmVif. The effect is slightly more muted in our in vitro assays, possibly due to RNA being removed from huA3G during the purification process. Unfortunately, due to the difficulties of purifying rcmA3G, we could not perform in vitro assays on it like we have for huA3G. Even pulldowns of ubiquitinated rcmA3G from 293T cells were tricky because levels of rcmA3G are difficult to control for between lanes due to active degradation and modification (**Fig. 3.3b-c**). Nonetheless we still see HIV-1 Vif polyubiquitinate rcmA3G which is an interesting observation to note.

When we limit the reaction to only the priming step by using only ARIH2 and UBE2R1, the priming E2, and to only monoubiquitination by using meUb, we see that HIV-1 Vif is able to multi-monoubiquitinate huA3G at multiple sites while rcmVif only placed ubiquitin on one or two sites on huA3G. The Y86H mutation in rcmVif is again an intermediate in this scenario since

it did not monoubiquitinate as many sites as HIV-1 Vif, but we see higher molecular weight bands not seen in rcmVif. However, we are unsure of whether the accessibility of additional monoubiquitination sites is the explanation behind why Y86H rcmVif is able to counteract hominid A3Gs.

Overall, we connect the infectivity differences between rcmVif and Y86H rcmVif from previous studies to Vif's ubiquitination activity. We show that Y86H rcmVif causes the degradation of huA3G to levels similar to that seen with HIV-1 Vif. Although the Y86H mutation in rcmVif did not appear to increase Vif's ability to bind huA3G, it still improved Vif's ability to ubiquitinate huA3G. Our experiments suggest that substrate and E3 orientation are more important an important consideration for huA3G antagonism. Future quantitative biochemical and structural studies of the HIV Vif-huA3G interface compared to the rcmVif-rcmA3G interface could shed light on this issue. These studies bring us new understanding on how SIVrcm gained a foothold in chimpanzees and eventually allow for transmission in humans.

Methods

Mammalian Cell Lines

HEK293T cells were obtained from ATCC, and cultured in DMEM (Gibco, #10566016) supplemented with heat-inactivated fetal bovine serum (Corning, #35011CV) and 1% penicillin-streptomycin (Invitrogen, #15140122). Cells were cultured at 37°C with 5% CO_2. Cells were mycoplasma-free and regularly tested for mycoplasma by PCR using a kit (ATCC, # 301012K).

Plasmids

pET-Duet SIVrcmVif-6xhis tag, CBFb and pET-Duet Y86H SIVrcmVif-6xhis tag, CBFb plasmids were obtained by deleting out the 6xhis tag on CBFb from pET-Duet vectors from previously described vectors (24), inserting a 6xhis tag on the Vif by encoding the addition into

primers, and using these primers to amplify pET-Duet SIVrcmVif, CBFb plasmids to introduce the tag. The PCR product was then DPNI treated (NEB, # R0176S), phosphorylated (NEB, #M0201S), and ligated (NEB, # M2200S). pGEX4T1 GST-ARIH2 was cloned by Gibson assembly using an NEB HiFi DNA assembly kit (NEB #E2621). pCDF EloB/EloC vectors were previously described[27].

The pcDNA human A3G-3xFLAG and pCS2 myc-ubiquitin plasmids were a gift from the Emerman Lab. The pcDNA4 Hxb2 Vif-2xstrep plasmid was the same as previously published[34]. To generate pcDNA rcmVif-2xstrep and rcmA3G-3xFLAG constructs, G blocks containing codon-optimized genes were PCR amplified and inserted into an empty vector. The pcDNA4 Y86H rcmVif-2xstrep and Y40/44A HIV NL4-3 Vif-2xstrep were obtained by site-directed mutagenesis of pcDNA plasmids containing the wild-type versions of rcmVif and NL4-3 Vif, respectively.

Protein Expression and Purification

UbE1, CDC34, UbE2L3, Cul5/Rbx2, NEDD8 E1, NEDD8 E2, NEDD8, and Hxb2 Vif were all prepared and purified as previously described[16].

VCBC complexes containing rcmVif and Y86H rcmVif were made by cotransforming Vif and CBFb expressing pETDuet and pCDF EloBC plasmids into BL21(DE3) cells (NEB #C2527H). The cells were grown at 37°C to OD ~0.6 and induced with 0.5mM IPTG at 16°C overnight. Cells were pelleted at 4000rpm for 15 minutes at 4°C and lysed using sonication in 25mM Tris-HCl pH 8, 500mM NaCl, and 40mM imidazole. The lysate was centrifuged 14500rpm for 40 minutes at 4°C, loaded onto a nickel column (Cytiva #17524802), and eluted on an FPLC using a gradient from 10mM to 1M imidazole in 25mM Tris-HCl pH 8 and 150mM NaCl. Fractions containing the VCBC complex were diluted to 30mM salt, loaded onto a Q

column (Cytiva #17115401) and eluted on an FPLC using a gradient from 30mM to 1M NaCl in 25mM Tris-HCl pH 8 and 2mM DTT. Fractions containing the VCBC complex were concentrated and purified using size exclusion chromatography on a Superdex SD200 column with 20mM HEPES pH 8, 300mM NaCl, 10% glycerol, and 1mM DTT.

To purify ARIH2, pGEX4T1 GST-ARIH2 plasmid was transformed into BL21 Star (DE3) cells (Thermo #C601003), grown to an OD ~0.6 at 37°C, and induced with 0.1mM IPTG at 16°C overnight in media containing 0.1mM $ZnCl_2$. Cells were pelleted at 4000rpm for 15 minutes at 4°C and lysed using sonication in 20mM HEPES pH 8, 50mM NaCl, 0.1mM $ZnCl_2$, and 1mM DTT. The lysate was centrifuged 14500rpm for 40 minutes at 4°C, loaded onto a GST column (Cytiva #17513101), and eluted on an FPLC using a gradient from 0 to 40mM reduced glutathione in 20mM HEPES pH 8, 500mM NaCl, 0.1mM $ZnCl_2$, and 1mM DTT. Samples containing GST-ARIH2 were pooled, cleaved with thrombin overnight and desalted. After backpassing the desalted samples onto the GST column to get rid of cleaved tag, the flowthrough was collected and purified using size exclusion chromatography on a Superdex SD200 column with 25mM HEPES pH 8, 200mM NaCl, 0.1mM $ZnCl_2$, and 1mM DTT.

APOBEC3G Degradation Assays

293T cells were grown in a 6-well plate to about 60% confluency prior to transfection. The transfection mixture was prepared by adding 1μg of pcDNA Vif-2xstrep and 1μg of pcDNA A3G-3xFLAG plasmid to 100μL serum-free Opti-MEM (Gibco, #31985088) and 6μL of TransIT-LT1 transfection reagent (Mirus, #2300). 1μg of pcDNA empty vector plasmid was added in place of either the Vif plasmid or A3G plasmid in control wells not expressing one of the proteins. The mixture was then briefly and gently vortexed and incubated for 15 minutes at room temperature prior to being added dropwise into the wells.

5μM of Mg132 (Sigma Aldrich, #M7449) or an equivalent volume of DMSO was added to the cells 16 hours prior to harvesting. Cells were lysed with 350μL of buffer containing 50mM Tris 7.5, 150mM NaCl, 0.5% NP40, 1mM EDTA, and a cOmplete protease inhibitor tablet and sonicated for 3 seconds at 30% amplitude on a microtip sonicator. Samples were then analyzed using Western blotting.

FLAG Immunoprecipitation

293T cells were grown in a 6-well plate to about 60% confluency prior to transfection. The transfection mixture was prepared by adding 1μg of pcDNA Vif-2xstrep, 1μg of pcDNA A3G-3xFLAG plasmid, and 1μg pCS2 myc-ubiquitin (gift from Emerman Lab, for pulldowns including myc-ubiquitin only) to 100μL serum-free Opti-MEM (Gibco, #31985088) and 3μL of TransIT-LT1 transfection reagent (Mirus, #2300) for each μg of plasmid.

Cells were harvested 48 hours post-transfection using a Triton X-100 buffer containing 50 mM Tris-HCl pH 7.5, 150 mM NaCl, 1.1% Triton X-100, 1mM EDTA, and a cOmplete protease inhibitor tablet. For samples containing myc-ubiquitin only, the lysate was boiled at 95°C for 5 minutes. All samples were sonicated for 3 seconds at 30% amplitude on a microtip sonicator, and spun down in a centrifuge at max speed.

The supernatant was then incubated with magnetic strep beads (Fisher, #501933310) for 4 hours and 2μL of RNase A/T1 mix for RNase-treated samples (Thermo Fisher, # EN0551). Bound protein was eluted with 500ng/μL 3xFLAG peptide (Sigma Aldrich, #F4799) diluted in 1xTBS for 1 hour rotating at 4°C. Samples were then analyzed using Western blotting.

In vitro Ubiquitination

In vitro ubiquitination was performed as previously described[16]. Rcm, Y86H, and HIV-1 Vifs were mixed with neddylated Cul5/Rbx2 at a 1:1 molar ratio 30 minutes prior to combining

the substrates, E3, and charging reactions. Reactions were quenched with protein loading buffer containing SDS and betamercaptoethanol.

Western Blotting

Samples from A3G degradation assays, strep coIPs, FLAG IPs, and in vitro ubiquitination were treated with 4x protein loading dye (200mM Tris-HCl 6.8, 8% SDS, 40% glycerol, 20% β-mercaptoethanol, 50mM EDTA, and bromophenol blue) and run on 4-15% gels (Bio-Rad, #4561086). The samples were then wet transferred onto PVDF membranes (MilliporeSigma, #IPFL00010). The membranes were blocked with 1% BSA for 1 hour and incubated with the following concentrations of antibodies diluted in 1% BSA for 1 hour: 1:5000 mouse anti-strep HRP (EMD Millipore, #71591-3), 1:5000 mouse anti-GAPDH (Proteintech, #60004-1-Ig), 1:2500 rabbit anti-FLAG (Sigma Aldrich # F7425-.2MG), and 1:2500 mouse anti-myc (Sigma Aldrich, #M4439).

The blots were washed three times with TBST and then incubated with 1:5000 fluorescent anti-mouse (Bio-Rad, #12004158) and anti-rabbit (Bio-Rad, #12005869) secondary antibodies for 1 hour. The blots were washed three times with TBST again, treated with ECL reagent (Invitrogen, #WP20005), and visualized on a BioRad chemidoc system.

References

1. Li, Y. L. *et al.* The structural basis for HIV-1 Vif antagonism of human APOBEC3G. *Nature* **615**, 728–733 (2023).
2. Global HIV & AIDS statistics — Fact sheet. (2023).
3. Hahn, B. H., Shaw, G. M., De Cock, K. M. & Sharp, P. M. AIDS as a zoonosis: Scientific and public health implications. *Science (1979)* **287**, 607–614 (2000).
4. Beer, B. E. *et al.* Characterization of Novel Simian Immunodeficiency Viruses from Red-Capped Mangabeys from Nigeria (SIVrcmNG409 and -NG411). *J Virol* **75**, 12014–12027 (2001).
5. Sharp, P. M. & Hahn, B. H. Origins of HIV and the AIDS pandemic. *Cold Spring Harb Perspect Med* **1**, 1–22 (2011).
6. Jarmuz, A. *et al.* An anthropoid-specific locus of orphan C to U RNA-editing enzymes on chromosome 22. *Genomics* **79**, 285–296 (2002).
7. Mangeat, B., Turelli, P., Liao, S. & Trono, D. A Single Amino Acid Determinant Governs the Species-specific Sensitivity of APOBEC3G to Vif Action. *Journal of Biological Chemistry* **279**, 14481–14483 (2004).
8. Harris, R. S. *et al.* DNA Deamination Mediates Innate Immunity to Retroviral Infection. **113**, 803–809 (2003).
9. Salter, J. D., Bennett, R. P. & Smith, H. C. The APOBEC Protein Family: United by Structure, Divergent in Function. *Trends Biochem Sci* **41**, 578–594 (2017).
10. Johnson, W. E. Origins and evolutionary consequences of ancient endogenous retroviruses. *Nat Rev Microbiol* **17**, 355–370 (2019).

11. Sheehy, A. M., Gaddis, N. C., Choi, J. D. & Malim, M. H. Isolation of a human gene that inhibits HIV-1 infection and is suppressed by the viral Vif protein. *Nature* **418**, 646–650 (2002).

12. Stopak, K., De Noronha, C., Yonemoto, W. & Greene, W. C. HIV-1 Vif blocks the antiviral activity of APOBEC3G by impairing both its translation and intracellular stability. *Mol Cell* **12**, 591–601 (2003).

13. Sheehy, A. M., Gaddis, N. C. & Malim, M. H. The antiretroviral enzyme APOBEC3G is degraded by the proteasome in response to HIV-1 Vif. *Nat Med* **9**, 1404–1407 (2003).

14. Jäger, S. *et al.* Vif hijacks CBF-β to degrade APOBEC3G and promote HIV-1 infection. *Nature* **481**, 371–375 (2012).

15. Zhang, W., Du, J., Evans, S. L., Yu, Y. & Yu, X. F. T-cell differentiation factor CBF-β regulates HIV-1 Vif-mediated evasion of host restriction. *Nature* **481**, 376–379 (2012).

16. Hüttenhain, R. *et al.* ARIH2 Is a Vif-Dependent Regulator of CUL5-Mediated APOBEC3G Degradation in HIV Infection. *Cell Host Microbe* **26**, 86-99.e7 (2019).

17. Sawyer, S. L., Emerman, M. & Malik, H. S. Ancient adaptive evolution of the primate antiviral DNA-editing enzyme APOBEC3G. *PLoS Biol* **2**, (2004).

18. Compton, A. A., Hirsch, V. M. & Emerman, M. The host restriction factor APOBEC3G and retroviral Vif protein coevolve due to ongoing genetic conflict. *Cell Host Microbe* **11**, 91–98 (2012).

19. Compton, A. A. & Emerman, M. Convergence and Divergence in the Evolution of the APOBEC3G-Vif Interaction Reveal Ancient Origins of Simian Immunodeficiency Viruses. *PLoS Pathog* **9**, (2013).

20. Bogerd, H. P., Doehle, B. P., Wiegand, H. L. & Cullen, B. R. A single amino acid difference in the host APOBEC3G protein controls the primate species specificity of HIV type 1 virion infectivity factor. *Proc Natl Acad Sci U S A* **101**, 3770–3774 (2004).

21. Schröfelbauer, B., Chen, D. & Landau, N. R. A single amino acid of APOBEC3G controls its species-specific interaction with virion infectivity factor (Vif). *Proc Natl Acad Sci U S A* **101**, 3927–3932 (2004).

22. Huthoff, H. & Malim, M. H. Identification of Amino Acid Residues in APOBEC3G Required for Regulation by Human Immunodeficiency Virus Type 1 Vif and Virion Encapsidation. *J Virol* **81**, 3807–3815 (2007).

23. Letko, M., Booiman, T., Kootstra, N., Simon, V. & Ooms, M. Identification of the HIV-1 Vif and Human APOBEC3G Protein Interface. *Cell Rep* **13**, 1789–1799 (2015).

24. Ito, F. *et al. Structural basis for HIV-1 antagonism of host APOBEC3G via Cullin E3 ligase*. https://www.science.org (2023).

25. Kouno, T. *et al.* Structural insights into RNA bridging between HIV-1 Vif and antiviral factor APOBEC3G. *Nat Commun* **14**, (2023).

26. Etienne, L., Hahn, B. H., Sharp, P. M., Matsen, F. A. & Emerman, M. Gene loss and adaptation to hominids underlie the ancient origin of HIV-1. *Cell Host Microbe* **14**, 85–92 (2013).

27. Binning, J. M., Chesarino, N. M., Emerman, M. & Gross, J. D. Structural Basis for a Species-Specific Determinant of an SIV Vif Protein toward Hominid APOBEC3G Antagonism. *Cell Host Microbe* **26**, 739-747.e4 (2019).

28. Binning, J. M. *et al.* Fab-based inhibitors reveal ubiquitin independent functions for HIV Vif neutralization of APOBEC3 restriction factors. *PLoS Pathog* **14**, (2018).

29. Yu, X. *et al.* Induction of APOBEC3G ubiquitination and degradation by an HIV-1 Vif-Cul5-SCF complex. *Science* **302**, 1056–60 (2003).

30. Chen, G., He, Z., Wang, T., Xu, R. & Yu, X.-F. A Patch of Positively Charged Amino Acids Surrounding the Human Immunodeficiency Virus Type 1 Vif SLVx4Yx9Y Motif Influences Its Interaction with APOBEC3G. *J Virol* **83**, 8674–8682 (2009).

31. Turner, T. *et al.* Differential Contributions of Ubiquitin-Modified APOBEC3G Lysine Residues to HIV-1 Vif-Induced Degradation. *J Mol Biol* **428**, 3529–3539 (2016).

32. Albin, J. S. *et al.* Dispersed sites of HIV Vif-dependent polyubiquitination in the DNA deaminase APOBEC3F. *J Mol Biol* **425**, 1172–1182 (2013).

33. Dang, Y., Wang, X., Zhou, T., York, I. A. & Zheng, Y.-H. Identification of a Novel WxSLVK Motif in the N Terminus of Human Immunodeficiency Virus and Simian Immunodeficiency Virus Vif That Is Critical for APOBEC3G and APOBEC3F Neutralization. *J Virol* **83**, 8544–8552 (2009).

34. Kim, D. Y. *et al.* CBFβ Stabilizes HIV Vif to Counteract APOBEC3 at the Expense of RUNX1 Target Gene Expression. *Mol Cell* **49**, 632–644 (2013).

Publishing Agreement

It is the policy of the University to encourage open access and broad distribution of all theses, dissertations, and manuscripts. The Graduate Division will facilitate the distribution of UCSF theses, dissertations, and manuscripts to the UCSF Library for open access and distribution. UCSF will make such theses, dissertations, and manuscripts accessible to the public and will take reasonable steps to preserve these works in perpetuity.

I hereby grant the non-exclusive, perpetual right to The Regents of the University of California to reproduce, publicly display, distribute, preserve, and publish copies of my thesis, dissertation, or manuscript in any form or media, now existing or later derived, including access online for teaching, research, and public service purposes.

DocuSigned by:
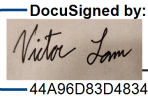
44A96D83D48346F...

Author Signature

12/11/2023

Date